Alma Mater Studiorum · Università di Bologna

Scuola di Scienze
Dipartimento di Fisica e Astronomia
Corso di Laurea in Fisica

SYNTHESIS AND CHARACTERIZATION OF $TiFe_{1-x}Ni_x$ INTERMETALLIC HYDRIDES FOR HYDROGEN STORAGE

Relatore:
Prof. Luca Pasquini

Presentata da:
Viola Ferretti

Anno Accademico 2023/2024

Abstract

Nowadays, human activities are heavily dependent on fossil fuels, which has resulted in both an environmental and energy crisis over the years. Hydrogen stands out as the most promising solution to transform energy production into a greener process. The hydrogen cycle consists of three key phases: production, storage, and conversion. Since green hydrogen production relies on renewable energy sources, which are inherently intermittent, efficient hydrogen storage is crucial to avoid energy losses and ensure a reliable energy supply when needed. In this context, hydrides present a particularly interesting solution. This research focuses on metallic hydrides based on Ni-substituted TiFe alloys. TiFe is known for its high volumetric density, good sorption kinetics, and reversibility, and it operates under mild temperature and pressure conditions. Furthermore, its performance can be enhanced through stoichiometric tailoring. Nickel is selected for partial substitution of Fe as it improves hydride activation, kinetics, cyclability, and stability, enabling hydrogen production under ambient conditions. Samples with the composition $TiFe_{1-x}Ni_x$ were synthesized with varying nickel content (x = 0.05, 0.10, 0.15, 0.20, 0.30) by arc melting and characterized in terms of composition, morphology, and structure via Scanning Electron Microscopy (through Energy Dispersive X-ray Spectroscopy and Secondary Electron Analysis) and X-ray Powder Diffraction. Thermodynamics of hydrogen sorption were investigated using a High-Pressure Differential Scanning Calorimeter and a Sievert apparatus, which allowed the construction of Pressure-Composition Isotherms. The study of $TiFe_{1-x}Ni_x$ samples across this compositional range provides a comprehensive review of the hydrogen sorption properties of these intermetallic hydrides and how they vary with Ni concentration. The main conclusion of this work is that partial Ni substitution only slightly modifies the crystal structure, expanding the unit cell volume and enabling hydride formation at lower equilibrium pressures, which is promising in the view of practical applications. Further analysis of hydride activation and kinetics will help complete the knowledge about the underlying physics of metallic hydrides. Moreover, extending the study to different compositions and stoichiometries may offer new insights into new potential solutions for hydrogen storage.

Contents

List of Figures

List of Tables

Chapter 1

Introduction

1.1 The world of today

Perhaps the most crucial challenge encountered by humans is that of the climate change. The main driver of this process is the greenhouse effect: some gases emitted in the Earth's atmosphere trap the heat coming from the sun and stop its re-emission in space, leading to global warming. These topics have become increasingly important in the last decades, but their causes can be found in the 18th century. In fact, while the responsible gases are naturally produced, human activities developed with industrialization add large quantities to their concentration in the atmosphere. Among them, carbon dioxide (CO_2) is the main contributor to the process of global warming. Pre-industrial societies were mainly based on agrarian economy, where the majority of the income derived from agriculture and farming. Because of photosynthesis, the carbon dioxide that was liberated by human activities and animals was reabsorbed by the plants, avoiding alterations of the environmental equilibrium. The first non-living machine that could transmit continuous power,

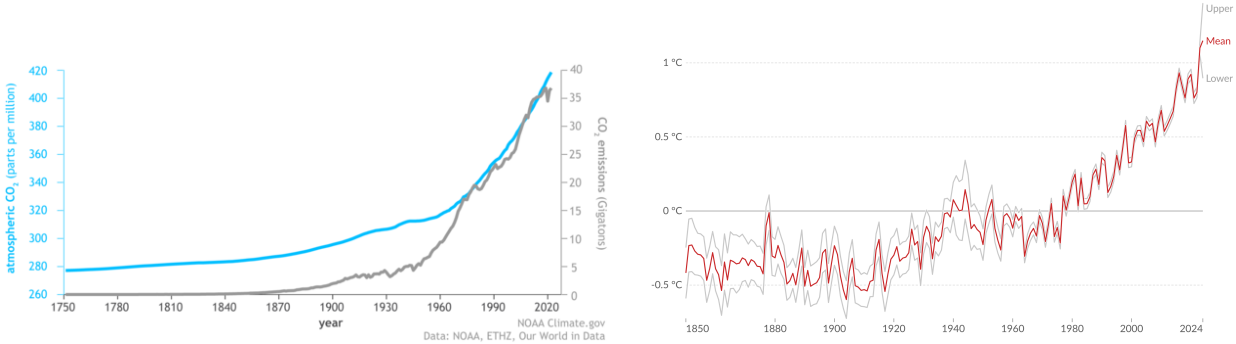

Figure 1.1: (a) CO_2 atmospheric concentration and emission increase,[2] and (b) parallel global temperature rise.[3]

created by humans to work for humans, was the steam engine, invented in 1712 by Thomas Newcomen. Its efficiency was later increased by James Watt, leading to the first industrialization, around 1760.[1] From this moment on, the history of humankind completely changed, leading to faster technological progress, increased accessibility of goods and development of new professions. But this innovation came with an important cost: the

resources to aliment steam engines were found in fossil fuels, resulting from compression and heating of ancient vegetation over geological time scales. The consumption of fossil fuels together with deforestation leads to the liberation of 7×10^{12} kg yr^{-1} of carbon in the form of CO_2. The two major natural sinks of carbon dioxide are plants and oceans, which absorb an additional 2×10^{12} kg yr^{-1} carbon, leading to an annual increase of 0.4% of the CO_2 concentration in the atmosphere (Fig. 1.1 (a)).
Another major contributor of greenhouse gases is the transportation sector, which developed in the 20th century and is mainly based on fossil fuels. In fact, it accounts for nearly one quarter of global energy-related CO_2 emissions, and it also causes the production of other air pollutants like NOX and PM10. For instance, road vehicles account for the largest part, due to the combustion of petroleum-based products, like gasoline, in internal combustion engines.[4]
Scientists began studying the process of CO_2 emissions early after the first industrial revolution. In the 1860s, physicist John Tyndall recognized Earth's natural greenhouse effect and suggested its influence on climate. In 1896, Svante Arrhenius first predicted that changes in atmospheric carbon dioxide levels could substantially alter the surface temperature through the greenhouse effect. More recently, Gilbert Plass formulated the "Carbon Dioxide Theory of Climate Change" in 1956.[5] As it can be seen in Fig. 1.1 (b), the previsions were correct: the average temperature of the Earth's surface is now about 1.1°C warmer than it was in the late 1800s (before the industrial revolution) and warmer than at any time in the last 100,000 years. The last decade (2011-2020) was the warmest on record, and each of the last four decades has been warmer than any previous decade since 1850.[4] While such researches should have raised awareness about the consequences of industrialization, the world energy consumption increased from 10^{12} kWh yr^{-1} in 1860 to 10^{14} kWh yr^{-1} today (Fig. 1.2).

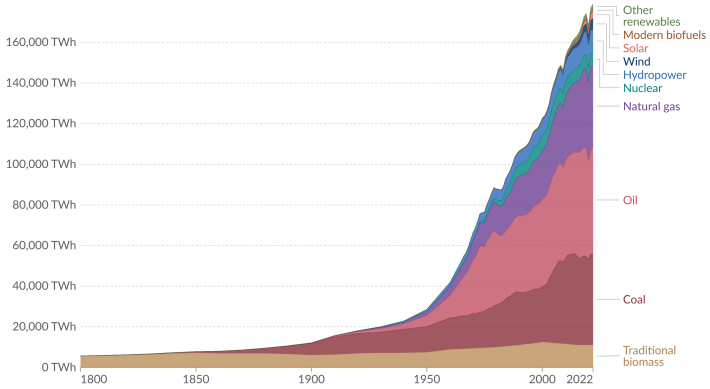

Figure 1.2: World energy consumption since 1800.[7]

Basically, humans are emptying fossil fuels reservoirs. Thus, together with the climate crisis, comes the energetic crisis. Moreover, the demand for fossil fuels has a strong impact on social, political and economic interactions between the various countries[1].[6] In this scenario, the only possibility is to convert the world economy and human lifestyle, now based on fossil fuels, to a sustainable one. The central idea is that energy should be entirely produced by "clean" means such as wind turbines, photovoltaics, geothermal power stations, etc. The inherently intermittent nature of renewable energy sources renders buffering and storage of energy indispensable. At present energy buffering is mainly provided by fossil

fuel-generated electricity. It is therefore necessary to look for other energy carriers, and hydrogen is one of the most attractive candidates thanks to its unparalleled gravimetric energy density (33 kWh/kg) and because it can be integrated in a clean and closed material cycle from production to usage, while offering interesting storage and distribution possibilities,[8] as explained in the next section.

1.2 The world of tomorrow: Hydrogen

Hydrogen is an appealing solution to the climatic and energetic problems the world is facing today. Composed of one proton and one electron, it is the simplest, lightest and most abundant atom in the universe.

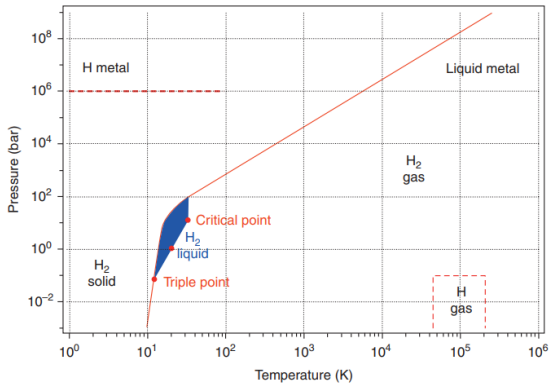

Figure 1.3: The hydrogen phase diagram.[12]

At low temperatures, H is a solid with a density of 70.6 kg m^{-3} at -262°C, and it is a liquid in a small zone between the triple and critical points (the blue region in Fig. 1.3) with a density of 70.8 kg m^{-3} at -253°C. At higher temperatures it is a gas, with a density of 0.089886 kg m^{-3} at 0°C and a pressure of 1 bar.[9]
As a fuel, green hydrogen only produces water as a combustion product. Its cycle, from production to usage, is depicted in Fig. 1.4. It is a closed and carbon-neutral cycle, characterized by the absence of CO_2 generation and by the fact that no living matter is necessary for its production. The first step of the cycle is the conversion of energy from a sustainable energy source, like sunlight, into electricity. The generated power is used to dissociate water into oxygen, which is released in the atmosphere, and hydrogen, which is stored, transported and distributed. Finally, hydrogen is combusted together with the oxygen in fuel cells, combustion engines or turbines. This process releases energy as work and heat, producing water or steam as waste.
Other than to its null environmental impact, the focus on hydrogen (H) is due to its efficiency as energy carrier.[10] As a reference, one of the most important parameter to consider is the gravimetric energy density, defined as the available energy per unit mass of substance, thus expressed in Watt-hours per kilograms. H has three times the gravimetric energy density of gasoline: 33 kWh/kg against 12 kWh/kg.[11] In simple terms, this means 1 kg of hydrogen can generate three times the energy produced by 1 kg of gasoline, thus needing a smaller amount of material to produce the same energy. The problem is that hydrogen is a gas in standard conditions (Fig. 1.3): considering the same example as a

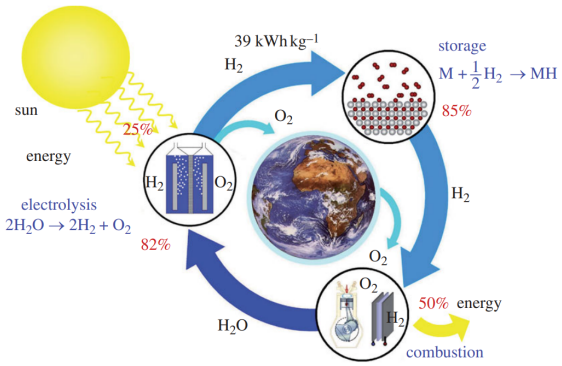

Figure 1.4: Green hydrogen cycle.[1]

reference, 1 kg of H at 25°C and 1 bar requires a volume of 11 m^3, thus occupying much more space than 1 kg of gasoline. This property is described by the volumetric energy density, i.e. the available energy per unit volume of substance. It is clear that H has a very low volumetric energy density; in fact, due to its low critical point (T_C = 33 K, see Fig. 1.3) it is very difficult to obtain satisfactory volumetric energy density, even applying high pressures.[11]
Additionally, as all fuels, some degree of danger characterizes the use of H, because it has a wide range of flammable concentrations in air and low ignition energy. As a consequence, additional controls and monitoring are needed to ensure secure use of H as a fuel.[13]
Therefore, it is necessary to develop compact and secure hydrogen storage media in order to manage efficiently and safely hydrogen production and use. There is an ongoing effort to create a safe and efficient hydrogen-based energy cycle, as it is demonstrated by the current projects and long-term plans in action.[4,6,13,14]

1.2.1 Hydrogen production

H can be produced via different techniques, some based on fossil fuels and others based on renewable sources, i.e. from solar light or indirectly via electricity from wind power or hydro power. In the second category, clean H production is mainly based on water electrolysis:

$$2H_2O(l) \rightarrow 2H_2(g) + O_2(g) \tag{1.1}$$

A typical water electrolyzer comprises three main components: an electrolyte, a cathode, and an anode. The water splitting reaction is an uphill process, thus an externally generated voltage that exceeding the equilibrium voltage of water splitting is required to decompose water molecules into hydrogen gas in the hydrogen evolution reaction (HER) at the cathode, and oxygen gas in the oxygen evolution reaction (OER) at the anode. The standard equilibrium voltage of the water electrolysis cell is U_0 = 1.229 V (at T = 298 K, P = 1 atm and pH = 0). The energy efficiency of the water splitting reaction is defined as the ratio of the thermodynamic equilibrium cell voltage to the real cell voltage, U_{cell}, which accounts for the overpotentials that stem from charge transfer reactions on anode and cathode sides, ohmic losses due to ion migration in the electrolyte phase, and from other parasitic losses.[15] Today, H electrolysis is around 70% energy efficient. To produce H from water and sunlight, solar cells and electrolizers can be combined. A promising

method is to directly produce H through photoelectrochemical water splitting:

$$2H_2O(l) \; + \; h\nu \; \rightarrow \; 2H_2(g) \; + \; O_2(g) \tag{1.2}$$

Photoelectrochemical cells employ one or more semiconductor electrodes, in such a way that, when illuminated by a light source with an energy greater than the semiconductor energy gap, charge carriers are excited from valence to conduction band. So, the photo-induced potential can be employed to promote chemical reactions at the interface. This is represented in Fig. 1.5 for a cell consisting of an n-type semiconductor as anode and a metal as cathode: water oxidation takes place at the semiconductor-electrolyte interface and hydrogen production occurs at the metal electrode.[16]

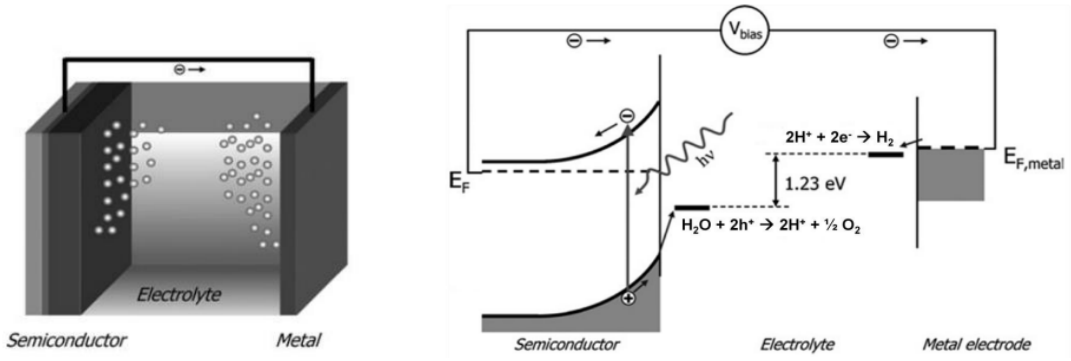

Figure 1.5: Photoelectrochemical cell (a) structure and (b) process.[16]

1.2.2 Hydrogen storage

After its production via electrolysis, hydrogen is a gas. Storage systems are characterized by two main parameters: gravimetric and volumetric density. The former is the ratio of the mass of H to the mass of the storage system; the latter is the mass of H divided by the volume of the storage system. The aim of hydrogen storage is to reach the highest possible volumetric density, by reducing the gas volume. Different techniques to store H are known and they comprehend:

- high-pressure gas cylinders;
- cryogenic tanks for liquid hydrogen;
- physisorption;
- storage via chemical reactions;
- hydrides.

The former are the most common storage systems and they can support up to 80 MPa, causing H to reach a volumetric energy density of 33 kg H_2 m^{-3}. On the other hand, the gravimetric density decreases with increasing pressure, representing a drawback in the applications of this method, which is usually only applied in laboratories. In addition,

Table 1.1: *Basic H storage systems and their main features.*[12]

Storage system	Volumetric density (kg H_2 m^{-3})	Gravimetric density (wt%)	P_{abs} (bar)	T_{abs} (K)
High-pressure gas cylinders	≤ 33	13	800	298
Cryogenic liquid H_2 containers	71	100	1	21
Physisorption	20	4	70	65
Metal hydrides	≤ 150	2	1	298
Complex hydrides	150	18	1	298
Chemical reactions with H_2O	≤ 100	14	1	298

safety of gas cylinders is a concern, requiring some structural modifications to make them resistant to mechanical and corrosion damage.
The second possibility is represented by systems that reach temperatures lower than the critical point T_C (1.3), allowing the storage of liquid H. The liquefaction is realized through the Joule-Thompson cycle (Linde cycle): the gas is compressed, cooled and then partially liquefied in an isenthalpic expansion. Because H warms up during the last step, a cooling mechanism based on N_2 is also employed. In these tanks, H is conserved at 21.2 K at ambient pressure, without any coverage that could increase the pressure, and consequently the temperature. The large amount of energy required to realize liquid H, and the delicate required conditions to store it, restrict its possible applications to those where H is used in a short time period.
Thirdly, physisorption of gas molecules by a solid offers an interesting alternative for H storage. This process is generated by the van der Waals interactions of gas molecules with a solid substrate, and is reversible. The variation of van der Waals interaction with the distance r between the gas molecule and the surface, is regulated by an attractive term which depends on r^{-6}, and a repulsive term which varies with r^{-12}. This interaction is weak and can only be observed at temperatures below 273 K. The binding of the gas molecules to the solid substrate through van der Waals forces generates the first monolayer of adsorbate, which is either liquid of solid. The second layer is the result of the binding of the gas and the adsorbed material, thus the binding energy is equal to the latent heat of sublimation of the adsorbate. The amount of adsorbed hydrogen is proportional to the specific surface area of the adsorbent, i.e. the total surface area per unit mass. An example of storage systems based on physisorption is represented by carbon nanotubes, which thanks to the large specific surface area and the curvature of the structure, allow H atoms to recombine and arrange themselves in a concentric pattern inside the nanotube. In the end, the maximum measured absorption capacity of the nanostructured material is 2 mass%.[19]
Considering the fourth possibility, hydrogen can be generated by reacting metals and chemical compounds with water. When Na is put in water, NaOH is formed, with a gravimetric H density of 3 mass%; replacing Na with Li, a gravimetric hydrogen density of 6.3 mass% is reached. The major challenge of this storage method is reversibility and control of the thermal reduction process.[9]
Finally, hydrides are an attractive H storage method. They are solid systems resulting from the reaction metallic compounds with H, which generally occurs at elevated temperatures and at constant pressure. Such reaction consists in an absorption process during

which H atoms enter the lattice of the host material and occupy the available interstitial sites, transforming the absorbent material in an hydride. The simplest way to represent this is the following:

$$M(s) + \frac{x}{2}H_2(g) \rightleftharpoons MH_x(s) \tag{1.3}$$

The process is fully reversible, allowing to extract H when needed, through an endothermic process. This makes hydrides a safe and compact H storage system. In general, hydrides volumetric density can reach above 100 kg H_2 m^{-3},[10] at the cost of a limited gravimetric density, due to the high weight of the metallic host. Indeed, metal hydrides can stack up to 2 mass%. On the other hand, complex hydrides can absorb up to 18 mass%, but suffer from inadequate thermodynamic and kinetic properties, as well as limited reversibility. The conditions for hydrogen absorption and desorption can be tailored by partial substitution of the constituent elements in the host lattice.[19] The challenge in hydride study is to realize systems that are able to incapsulate and release H at ambient temperature and atmospheric pressure, to make the operation simple and to avoid the need of additional work in this step of the H cycle.

1.2.3 Hydrogen conversion

When the stocked hydrogen is needed for practical applications, it must be transferred to a conversion device which transforms it into usable energy, like a fuel cell (FC). FCs consist of an anode, where oxidation occurs, a cathode, where reduction occurs, and an electrolyte, where ions carry the current between the electrodes. The chemical energy present in hydrogen is converted into electrical energy by controlled electrochemical reactions at each of the electrodes in the cell, completing the overall reaction

$$2H_2(g) + {}_2(g) \rightarrow 2H_2O(l) \tag{1.4}$$

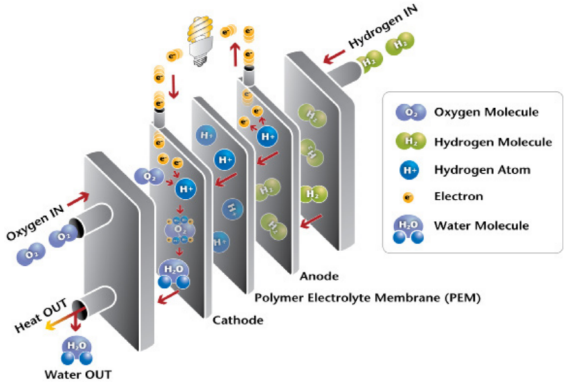

Figure 1.6: Proton Exchange Membrane fuel cell.[13]

Fuel cells can be based on different structures and processes; among them, Polymer Electrolyte Membrane (PEM) fuel cell is the most promising one (1.6). In a PEMFC, the fuel gas flows through channels to the anode, where H_2 molecules are separated into protons and electrons. While the PEM only allows protons to pass and go towards the cathode, electrons follow an external circuit to the cathode, producing electricity, i.e. work that can

be used to power an external machine. When the electrons reach the cathode after doing work, they find the protons and oxygen coming from the air flowing through channels to the cathode, and react to form water. The latter is an exothermic reaction, generating heat that can be used outside the FC.
In order to speed up the reactions at electrodes, catalysts are added to them. Fuel cells electrodes are complex structures, because they have three functions: they ensure a stable interface between the reactant gas and the electrolyte, they catalize the electrode reactions and they conduct electrons from or to reaction sites. A significant problem is the control of the the so-called three-phase boundary, where the electrolyte, electrode, and the reactant H_2 gas all come together; indeed, a stable three-phase boundary is crucial to the good performance and long operation of the system. In addition, fuel cell systems require sophisticated control systems to provide accurate metering of the fuel and air and to exhaust the reaction products. Important operational factors include stoichiometry of the reactants, pressure balance across the separator membrane, and freedom from impurities that can shorten life by poisoning the electrodes. Fuel cells can operate with very high electrical efficiencies approaching 60-70%.[17]

In this wide framework, the focus of this thesis is on metal hydrides-based H storage, whose structure and physical behavior will be discussed in detail in the next chapter.

Chapter 2

Metal Hydrides

2.1 Hydride-forming metallic compounds

From the chemical point of view, H shows a vast versatility thanks to the various bonding types it can create with other elements, such as metallic, ionic, or covalent bonding. Focusing on the former interaction, it is good to start with a description of the host metallic materials.

2.1.1 Transition metals

Most metals have simple crystal structures: body-centered cubic (*bcc*), face-centered cubic (*fcc*) or hexagonal close-packed (*hcp*). Each structure is characterized by a different level of packing. *fcc* and *hcp* are tightly packed, meaning that there is little free space left between crystal metal (M) atoms: in volumetric terms, only 26% of the space remains empty; on the other hand, *bcc* is a less closely packed structure, leaving 32% of the space empty. The quantity of free space in a crystal is a crucial information when talking about

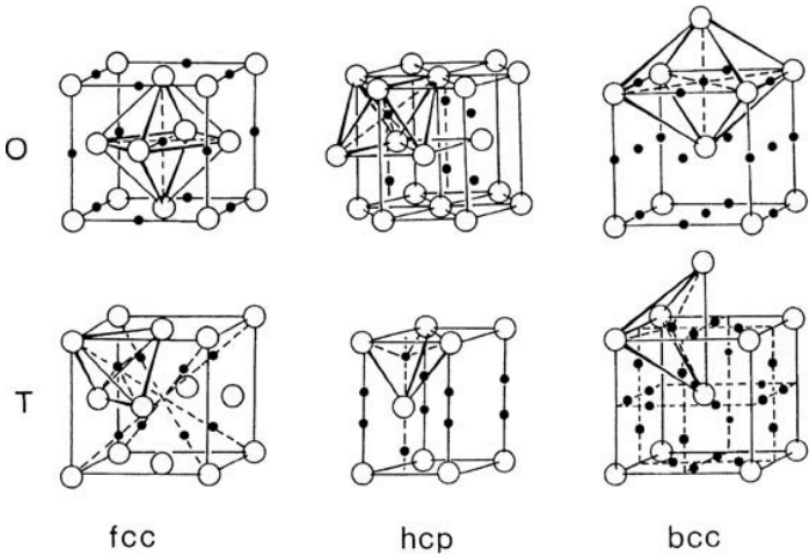

Figure 2.1: *bcc*, *fcc* and *hcp* crystal structures (columns) and the relative octahedral (O) and tetrahedral (T) interstitial sites (rows).[18]

gas storage. In fact, it determines the size of the interstices where the gas atoms can be hosted when they interact with the metal. The interstitial sites in these crystal structures can be of two types, depending on the disposition of atoms surrounding them:

- octahedral sites (delimited by six M atoms in the corners of a regular octahedron)
- tetrahedral sites (delimited by four M atoms in the corners of a regular tetrahedron)

If R is the radius of the large spheres, representing the M atoms, then the radii of the inscribed spheres in the octahedral and tetrahedral interstices are $R_T = 0.225R$ and $R_O = 0.414R$ in the fcc or hcp, and $R_T = 0.291R$ and $R_O = 0.115R$ in the bcc.[19] Metals can host H atoms in these spaces and form hydrides of type MH_n, with $n = 1, 2, 3$, that can exist as multiphase systems. Because the lattice structure is that of a typical metal with atoms of hydrogen on the interstitial sites, they are called interstitial hydrides.
Among metals, the focus is on transition metals, due to their unique properties. This class of materials is found between the alkali earths to the noble metals , as can be seen in Fig 2.2. Properties of transition metals are to a considerable degree dominated by

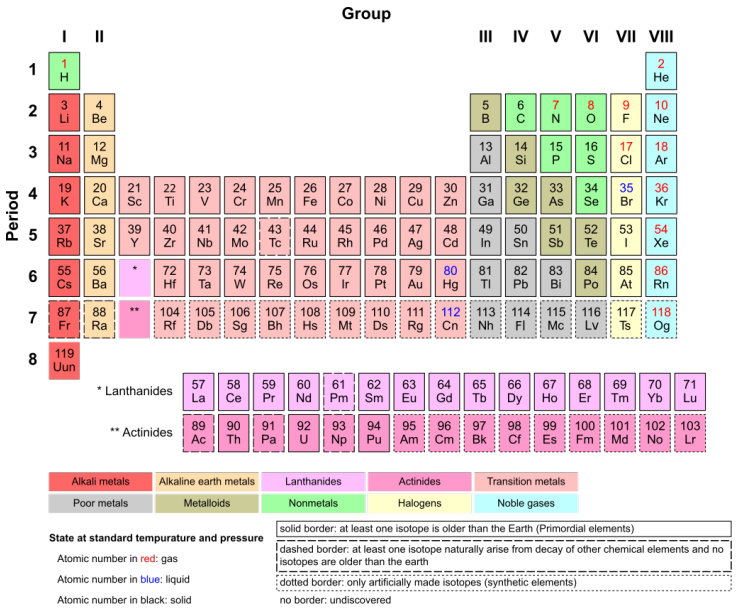

Figure 2.2: Periodic table of elements, where transition metals are highlighted in pink.

electrons in the d-band, which is gradually filled through the rows, going from the empty d-shell in the alkali earths to the completely filled one in the noble metals. Their band structure is constituted by a broad low-density energy band of s,p-type electrons and a narrow high-density d band that extends through the Fermi energy; in this scenario, the tight-binding approximation is the best starting point to study electronic properties of these materials.[20] In principle, all transition metals can be expected to form metallic hydrides. However, some of them have not been observed because they would only be stable at unrealistically high pressures, thus past research on hydrides has been largely confined to V-H, Nb-H and Pd-H binary systems.[21]

2.1.2 Compositional tailoring

MH_n binary hydrides have the limiting compositions MH, MH_2, and MH_3. Thus, it is often convenient to synthesize intermetallic compounds of transition metals to improve the properties of the materials of interest. Such compounds have been defined in 1967 by Schulze[22] as solid phases containing two or more intermetallic elements, with optionally one or more non-metallic elements, whose crystal structure differs from that of the other constituents. They are indicated by the general formula $AB_{\mathtt{x}}$, where $\mathtt{x} = B/A$ is the stoichiometric ratio. A is an element that forms very stable metallic hydrides (e.g. rare earths and early transition metals), meaning that it has a high hydrogen affinity, represented by the fact that the enthalpy variation in the $A - H$ reaction is large and negative; on the other side, the B element only forms hydrides at very high pressure (e.g. late transition metals), characterized by a positive or only slightly negative enthalpy of reaction, as reported in Fig. 2.3. Representative examples of hydrides are $LaNi_5$, $CeNi_3$, $TiMn_2$ and $TiFe$ for $\mathtt{x} = 5,\ 3,\ 2$ and 1, respectively. Moreover, partial substitution of A and/or B atoms can be useful to tune the properties of the alloy, as will be explained.

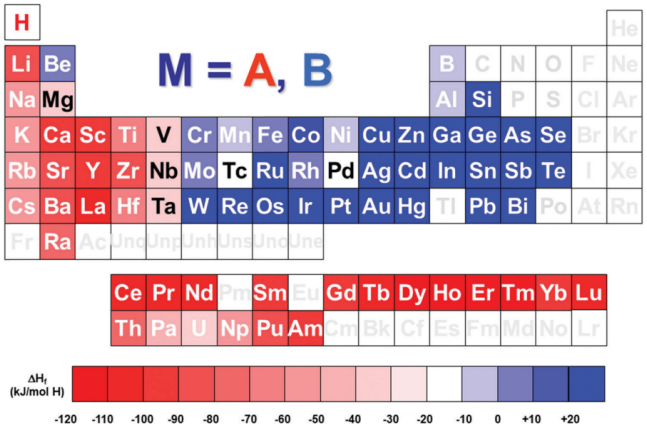

Figure 2.3: Periodic table of the elements showing the formation enthalpy of binary M–H metal hydrides, and the relative classification of A (in red) or B-type (in blue) M elements.[23]

2.2 Hydride formation

2.2.1 Interaction of H with metals

If the metal is exposed to H_2 atmosphere, the gas can interact with the metal surface through a reaction called absorption process, which can be described in terms of a one-dimensional potential energy curve (Fig. 2.4). Far from the metallic surface, hydrogen is in its gaseous form, i.e. the H_2 molecule. By approaching the surface, the process begins and follows the steps listed below (and illustrated in Fig. 2.5):

(1) physisorption

(2) H_2 molecule dissociation

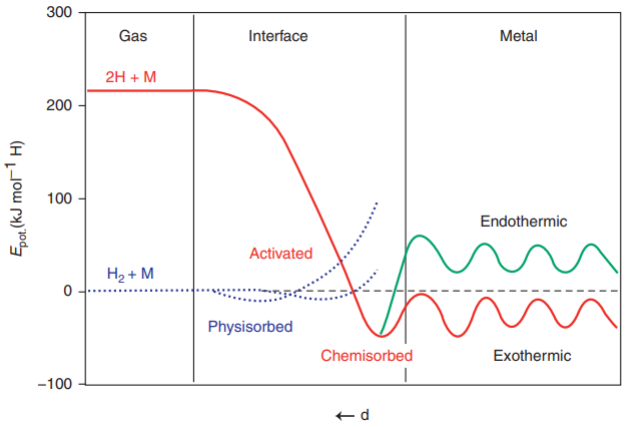

Figure 2.4: Lennard-Jones potential of hydrogen approaching a metallic surface. Far from the metal surface, the potential of a hydrogen molecule and that of two hydrogen atoms are separated by the dissociation energy. The first attractive interaction of the hydrogen molecule is the van der Waals force leading to the physisorbed state. Closer to the surface, the hydrogen has to overcome an activation barrier for dissociation and formation of the hydrogen metal bond. Hydrogen atoms sharing their electron with the metal atoms at the surface are then in the chemisorbed state. In the next step, the chemisorbed hydrogen atom can jump in the subsurface layer and finally diffuse on the interstitial sites through the host metal lattice.[12]

(3) H-metal bond formation

(4) subsurface H diffusion

(5) solid solution (α phase)

(6) hydride phase (β phase)

In (1), the first attractive interaction between the H_2 molecule and the metal surface arises and corresponds to the van der Waals interaction, which leads to a physisorbed state with energy $E_{phys} = -5\ kJ \cdot mol^{-1} \cdot H$ at approximately one H_2 molecule radius (0.2 nm) from the metal surface. Closer to the surface, step (2) begins. The difference between the H_2 molecule potential and the energy of two separated H atoms is the energy necessary to let the following reaction happen:

$$\frac{1}{2}H_2 \rightarrow H \tag{2.1}$$

It is called the dissociation energy and it is equal to 218 $kJ \cdot mol^{-1} \cdot H$. Moreover, there is an energy barrier that the H_2 molecule has to overcome in order to allow the interaction between the H atom and the metal. When the activation barrier is overcome, the H-metal bond forms (step (3)), thus the H atoms are in a chemisorbed state at energy $E_{chem} = -50\ kJ \cdot mol^{-1} \cdot H$, where they share their electron with the metal atoms. Eventually, in (4), the chemisorbed H atom can jump in the subsurface layer and finally diffuse on the interstitial sites through the host metal lattice. H atoms diffuse relatively fast in the metal lattice, gradually slowing down when the hydride starts to

form. For instance, at room temperature the H diffusion coefficient in metallic Mg is $D_H^{Mg} = 7 \cdot 10^{-}11\ m^2 s^{-1}$, but it decreases to $D_H^{MgH_2} = 10^{-}18\ m^2 s^{-1}$ in the hydride.[11] As the H atoms start entering the metal, while the H concentration is low (H/M<0.1), H atoms are exothermically dissolved in the host material, forming the α-phase. Assuming that this process occurs at thermal equilibrium between a solid solution and H_2 gas, one has:

$$\begin{cases} \mu^\alpha &= \frac{1}{2}\mu^g \\ \Delta h &= h^\alpha - \frac{1}{2}h^g \\ \Delta s &= s^\alpha - \frac{1}{2}s^g \end{cases} \tag{2.2}$$

In particular, Δh_s and Δs_s are the (partial molar) enthalpy and entropy of solution, respectively, corresponding to the enthalpy and entropy change when one H atom is dissolved from the gas (g) phase into a metal. The heat of solution thus defined can be determined by calorimetric measurements, as actually done for a number of systems.
Assuming that there are N_0 M atoms, N available interstitial sites and n H atoms, one can define the fraction of interstitial sites as $r = N/N_0$ and the atomic concentration of H atoms as $x = n/N_0$. The relation between H concentration and pressure is then described by the Sievert's equation:

$$\frac{x}{r-x} = \sqrt{\frac{p}{p_0}} \exp\left(-\frac{\Delta g_s}{RT}\right) \tag{2.3}$$

where p_0 is the standard pressure (1 bar) and Δg_s is the partial molar Gibbs free energy, given by:

$$\Delta g_s = \Delta h_s - T\Delta s_s \tag{2.4}$$

Therefore, $x \sim \sqrt{p}$ at low H concentration. In this regime, as H atoms are accommodated in the interstitial sites of the metal lattice, its volume expands by 2–3 $\dot{A}^3$ per hydrogen atom.
At greater hydrogen concentrations in the host metal (H/M>0.1), interactions between H atoms become stronger and lead to new changes in the metal. First, lattice expansion becomes important. Indeed, the volume per M atom increases linearly with H concentration:

$$v(x) = v_0 + x v_H \tag{2.5}$$

where v is the final volume per M atom, v_0 is the initial one, v_H is the volume increase per H atom (which is about 2-3 $\dot{A}^3$, as previously seen). In addition, v_H follows the relation

$$v_H = \left(\frac{\partial h^\alpha}{\partial p}\right)_T + T\left(\frac{\partial v_H}{\partial T}\right)_p \tag{2.6}$$

Noting that the pressure dependence of h^α essentially determines that of Δh_s, and that the second term, being much smaller than the first term, can be neglected for most purposes, we have

$$v_H = \left(\frac{\partial \Delta h_s}{\partial p}\right)_T \tag{2.7}$$

The effects of this behavior were first explained by Alefeld based on a mean-field theory: the lattice dilation produced by interstitial H atoms, can in turn interact with the stress

field of each H atom, and lower the heat of solution in proportion to the H concentration. Thus, the heat of solution is, in general, a function of H concentration and one can write for the total enthalpy change ΔH_s:

$$\frac{\partial \Delta H_s}{\partial x} = \left(\frac{\partial \Delta H_s}{\partial V}\right)_x \frac{\partial V}{\partial x} + \left(\frac{\partial \Delta H_s}{\partial x}\right)_V \tag{2.8}$$

The first term represents describes the unit cell enlargement due to the interstitial H atoms, and corresponds the elastic contribution. It can be written as

$$\left(\frac{\partial \Delta H_s}{\partial V}\right)_x \frac{\partial V}{\partial x} = \gamma K_0 \frac{v_H^2}{v_0} \tag{2.9}$$

where K_0 is a constant and

$$\gamma = \frac{2\,(1-2\sigma)}{3\,(1-\sigma)} \tag{2.10}$$

σ being the Poisson's ratio. This average elastic interaction, which does not depend on the local configuration of H atoms, can be called a mean-field contribution. The volume expansion usually corresponds to 10–20% of the metal lattice, causing the build-up of large stress at the phase boundary. This often leads to a decrepitation of brittle host metals such as intermetallic compounds; as a consequence, the final hydride is a powder with a typical particle size of 10–100 μm.

The second term is volume-independent and it represents the electronic contribution, as it derives from the extra electrons brought into the lattice by H atoms; it depends both on the total number of extra electrons, that acts uniformly over the crystal, and on the local electronic states, which become effective at shorter distances. This situation can be described by adopting a band-filling picture where the only effect of the extra electrons is to fill up the energy levels of the host metal up to the Fermi level, considering an additional effect due to the short-range repulsive interaction when the the H concentration.This repulsive force is confirmed by some empirical evidences. Firstly, H atoms do not come closer than 2.1 $\dot{A}$. Secondly, reduction of the partial configurational entropy has been noted in solid-solution phases in comparison to what is expected for random distribution over all interstitial sites,

$$s^c = -k \ln \frac{x}{r-x} \tag{2.11}$$

Considering the formula describing the configurational entropy, it is safe to conclude that s^c is decreased because r is decreased by the mutual blocking of H atoms, which grows with increasing x. Thirdly, nucleation and growth of the hydride phase (β-phase), and the formation of ordered structures in practically all M–H systems, can also be regarded as evidence for the short-range repulsion. Indeed, if H–H interactions were attractive, precipitation of H-rich phases should take place at low temperatures instead of formation of ordered arrangements.[18] The β-phase starts to nucleate and grow as soon as the metal α-phase has reached a saturation solubility and is the result of the direct interaction of H atoms with M ones. Thus, a miscibility gap forms due to the impossibility of the two phases to completely mix and the equilibrium condition is verified if the Gibbs free energy of hydride formation is zero:

$$\Delta G^{\alpha\to\beta} = \Delta H^{\alpha\to\beta} - T\Delta S^{\alpha\to\beta} = G^{0,\beta} - G^{0,\alpha} - RT \ln\left(\frac{p_{H_2}}{p_0}\right) = 0 \tag{2.12}$$

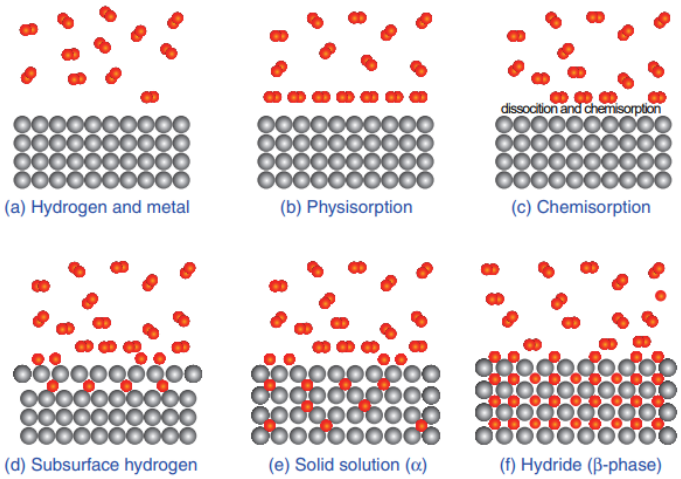

Figure 2.5: Schematic representation of the six distinct hydrogen absorption steps. First, the metal lattice is exposed to hydrogen gas in the non-equilibrium state, then: (1) at low temperature, hydrogen molecules adsorb at the surface of the metal; (2-3) dissociation of hydrogen molecules and chemisorption of hydrogen atoms; (4) subsurface hydrogen; (5) solid solution phase; and (6) hydride phase.[12]

This leads to van't Hoff equation, which is a fundamental law describing the relation between the temperature and pressure equilibrium conditions (T_{eq}, p_{eq}) for the coexistence of the two phases phases, and thermodynamic parameters characterizing hydride formation:

$$\ln\left(\frac{p_{H_2}}{p_0}\right) = \frac{\Delta H_0^{\alpha\to\beta}}{RT} - \frac{\Delta S_0^{\alpha\to\beta}}{R} \tag{2.13}$$

where $\Delta H_0^{\alpha\to\beta}$ and $\Delta S_0^{\alpha\to\beta}$ are the standard enthalpy and entropy of reaction. Therefore, when $p_{H_2} > p_{eq}$, the hydride state is stable and H is absorbed, while when $p_{H_2} < p_{eq}$, the metallic state is stable and H2 release occurs. From now on, apex will be dropped for Gibbs free energy, enthalpy and entropy of hydride formation.

In conclusion, the equality of chemical potentials means that the $\alpha \to \beta$ transformation takes place at a constant gas pressure, resulting in a plateau on the pressure–composition isotherm within the $(\alpha + \beta)$ two-phase composition range. In reality, hydride systems often show an hysteresis effect: the plateau pressure for hydride formation often exceeds that for hydride decomposition, as depicted in Fig.2.7. Schwarz et al.[24] explained this as the result of strain generated by the misfit present in the coherent mixture of two phases, which in turn generates a macroscopic energy barrier between the transforming phases. Indeed, in the presence of coherent interfaces, the Gibbs free energy does not only depend on the chemical potential (considered up to now), but also on the coherency strains, which correspond to the aforementioned energy barrier:

$$G_{\alpha+\beta} = g_{chem} + g_{coh} \tag{2.14}$$

Unlike the usual microscopic thermodynamic barriers, this energy barrier cannot be overcome by a thermal fluctuation, but only by a spontaneous increase of the free energy of the system, which is forbidden by the second law of thermodynamics. Therefore, during

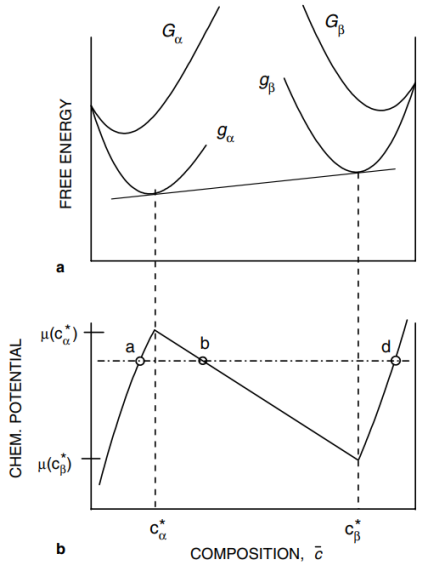

Figure 2.6: (a) Free-energy curves as a function of interstitial atom concentration for a solid that decomposes into two phases, α and β, separated by coherent interfaces. Curves g_a and g_b represent the chemical contribution to the single-phase free energies. Curves G_a and G_b represent the total single-phase free energies, which include the coherent strain energy contributions. (b) Chemical potential as a function of composition.[24]

the H-sorption process, the barrier effectively locks the system in a metastable state ($\alpha + \beta$), preventing it from reaching the stable state, until the increase in the driving force caused by an increase (decrease) in the chemical potential of the interstitials is able to eliminate the macroscopic barrier. Then, the transformation is unlocked and the spontaneous absorption (desorption) can proceed. This obstacle to the transformation due to the macroscopic barrier results in the splitting of the phase-transition pressure (temperature) into two pressures (temperatures): one during increase of pressure (cooling) and another during decrease of pressure (heating).[24]

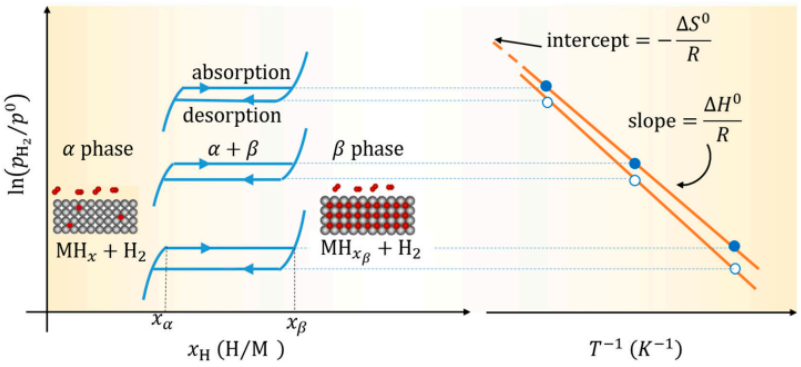

Figure 2.7: Pressure-Composition Isotherms (on the left) showing plateau pressures in correspondence of two-phase region, and hysteresis between absorption and desorption; the correspondent van't Hoff equation on the right side.[11]

2.2.2 Activation

In the first steps of H-M interaction, H_2 molecules dissociate and are chemisorbed is they overcome the energy barrier corresponding to the activation energy. This energy mainly depends on the host material surface and on its capacity to interact with H. Indeed, if the surface were ideal and clean, the absorption process would be fast and barrierless, but in real conditions it is hindered by the presence of passivating oxide layers formed on the metal surface due to air exposure. To facilitate the hydride activation, different solutions can be applied. One of the most popular approaches is to perform thermal treatments, bringing the material to high temperatures and pressures. Moreover, mechanical treatments can be done, like high-pressure torsion, ball-milling and rolling. Otherwise, the reactivity of the metal surface with H can be improved by adding catalyst particles which easily react with it, like Ni or Pd; another solution is alloying: substituting elements that enhance H penetration inside the metal, such as Mn, Zr or Cr.[11 25 26]

2.2.3 Kinetics: JMAK model

As previously described, H-sorption is composed of several different steps. Since a reaction can only proceed as fast as its slowest step, its kinetics is mainly determined by the principal rate-limiting step. Nonetheless, the interplay between more of them can also drive the transformation. To determine the rate-limiting mechanism and try to get more insight on the atomistic interactions, the transformed fraction as a function of time $\alpha(t) = \frac{V^\alpha}{V^\alpha + V^\beta}$ is calculated and the best model that fits it is identified. In the case of hydrides, the process is limited by nucleation and growth of the β phase. Nucleation occurs preferentially along grain boundaries, so that different regions of the material have different nucleation probabilities. When regions start growing from separate nuclei, they impinge on each other and develop a common interface over which growth stops, while it continues elsewhere. This process is decribed by the JMAK (Johnson-Mehl-Avrami-Kolmogorov) model:

$$\alpha(t) = 1 - \exp\left(-(kt)^n\right) \tag{2.15}$$

where k is the rate constant and $n = a + bc$ is the so-called Avrami exponent or order of the transformation, which depends on: $0 < a < 1$ such that $a = 0$ if nucleation ends shortly after the beginning of the process or $a = 1$ if the nucleation is constant in time; $b = 0.5$ for diffusion-limited case or $b = 1$ for source-limited ones, and on $c = 1, 2, 3$ describing the dimensionality (1 for 1-D linear growth or 3 for 3-D spherical growth).

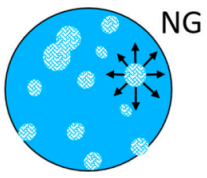

Figure 2.8: Schematic representation of the nucleation and growth model.[11]

From this, a function that is linear with time can be found:

$$\mathcal{F}(\alpha) = \left(-\ln(1-\alpha)^{\frac{1}{n}}\right) = kt \tag{2.16}$$

which allows to a direct determination of kinetic parameters.[11 27]

2.2.4 Thermodynamics: Lattice-gas model

A good explanation of H-M interaction and hydride formation is given by the lattice-gas model. It was first formulated by Lee and Yang[12] and it was later applied to describe metal-hydrogen systems, like Pd-H and Nb-H.[18] Even if these calculations have been only partially successful so far, the theory gives an intuitive description of the processes occurring. The M-H system is described as a rigid periodic lattice of metal atoms and mobile interstitial hydrogen atoms. In this framework, the H atoms ensemble cannot be described as a free gas, due to the presence of the lattice and to their mutual interaction.Therefore, it can be described as a monoatomic gas whose interaction potential is represented by

$$U = \sum_{i,j} U(\left|\vec{R}_i - \vec{R}_j\right|) \tag{2.17}$$

where $\vec{R}_i$ is the position of the i-th atom and the following boundary conditions are valid:

(1) atoms have an impenetrable core of radius a: $U(r) = \infty$ for r<a

(2) the interaction has a finite range: $U(r) = 0$ for r>b

(3) the interaction is never strongly attractive : $U(r) > -\infty$

In practice, this means that two hydrogen atoms cannot occupy the same interstitial site (3) and that there is some sort of interaction between two H dissolved in a metal (1,2). These properties define the lattice gas. As a result, the energy of H atoms dissolved in the metal is given by both the H atomic potential (ϵ_0) and the H-H interaction potential (ϵ):

$$E = N_H\epsilon_0 + N_{HH}\epsilon \tag{2.18}$$

where N_{HH} is the number of nearest neighbor H-pairs, N_H is the number of H atoms in the metal, which is $N_H < N$ if N is the number available sites. With this assumption, if the zero energy level is taken at the energy of a free H atom outside the metal, the energy landscape seen by one H atom in a metal is represented in 2.9.

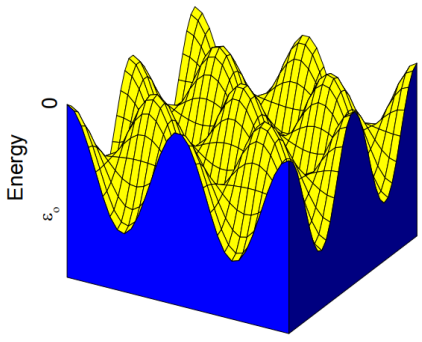

Figure 2.9: Potential seen by one H atom in a metal. The minima correspond to interstitial sites.[19]

The starting point to study the thermodynamics of the system is the Helmholtz free energy

$$F = -kT \ln \left[\sum \exp \left(\frac{E}{kT} \right) \right] \tag{2.19}$$

where the sum is performed considering all the configurations of N_H atoms distributed over the N available sites. To determine it, one needs to describe the N_{HH} parameter. By looking at the equation 2.18, it is clear that the problem is formally analogous to the Ising model. The appropriate approximation to allow its analytical solution is to assume that there is no short range order around H atoms, which is true in the case of weak interaction between them. This is the so-called Bragg-William approximation and it leads to:

$$N_{HH} = \frac{N_H n}{2} \frac{N_H}{N} \tag{2.20}$$

with n is the number of nearest neighbors interstitial sites, and $\frac{N_H}{N} = c_H$ is the probability of finding a nearest neighbor around a given H; the factor $1/2$ avoids counting the H-H pairs twice. Thus, the Helmholtz free energy is given by substituting 2.18 and 2.20 and by applying Stirling's formula in the limit of large N:

$$F = kTN \left[c_H \ln c_H + (1 - c_H) \ln (1 - c_H) \right] + N \left[\epsilon_0 c_H + \epsilon \frac{n}{2} c_H^2 \right] \tag{2.21}$$

It is now possible to find the chemical potential of hydrogen in the metal, also represented in picture 2.10:

$$\mu_H(c_H, T) = \left(\frac{\partial F}{\partial N_H} \right)_{T,V} = kT \ln \frac{c_H}{1 - c_H} + \epsilon_0 + \epsilon n c_H \tag{2.22}$$

At the thermodynamic equilibrium, the chemical potentials of the phases (left-side term for the gas, right-side term for H in a metal) are equal:

$$\frac{1}{2} \left(\epsilon_b + kTln \left(\frac{p}{p_0(T)} \right) \right) = kT \ln \left(\frac{c_H}{1 - c_H} \right) + \epsilon_0 + \epsilon n c_H \tag{2.23}$$

This equation describes the solubility isotherms in the one phase region, and in the limit of small hydrogen gas pressure ($p \rightarrow 0$, $c_H \rightarrow 0$) it corresponds to Sievert's law (eq. 2.3), as the H concentration in the metal is proportional to the square root of the H_2 pressure:

$$\frac{1}{2} kT \ln \frac{p}{p_0(T)} \sim kT \ln c_H \tag{2.24}$$

The equilibrium condition in eq. 2.23 may be unphysical at T<T_C, so one must also consider that:

$$\left(\frac{\partial \mu_H}{\partial c_H} \right)_{p,V} \geq 0 \tag{2.25}$$

which is reflected on the dependence of the Helmholtz free energy F on c_H, reported in in picture 2.10.
It is possible to show that the free energy can be minimized by assuming the existence of a mixed phase such that:

$$c_\alpha x_\alpha + c_\beta x_\beta = c_H \tag{2.26}$$

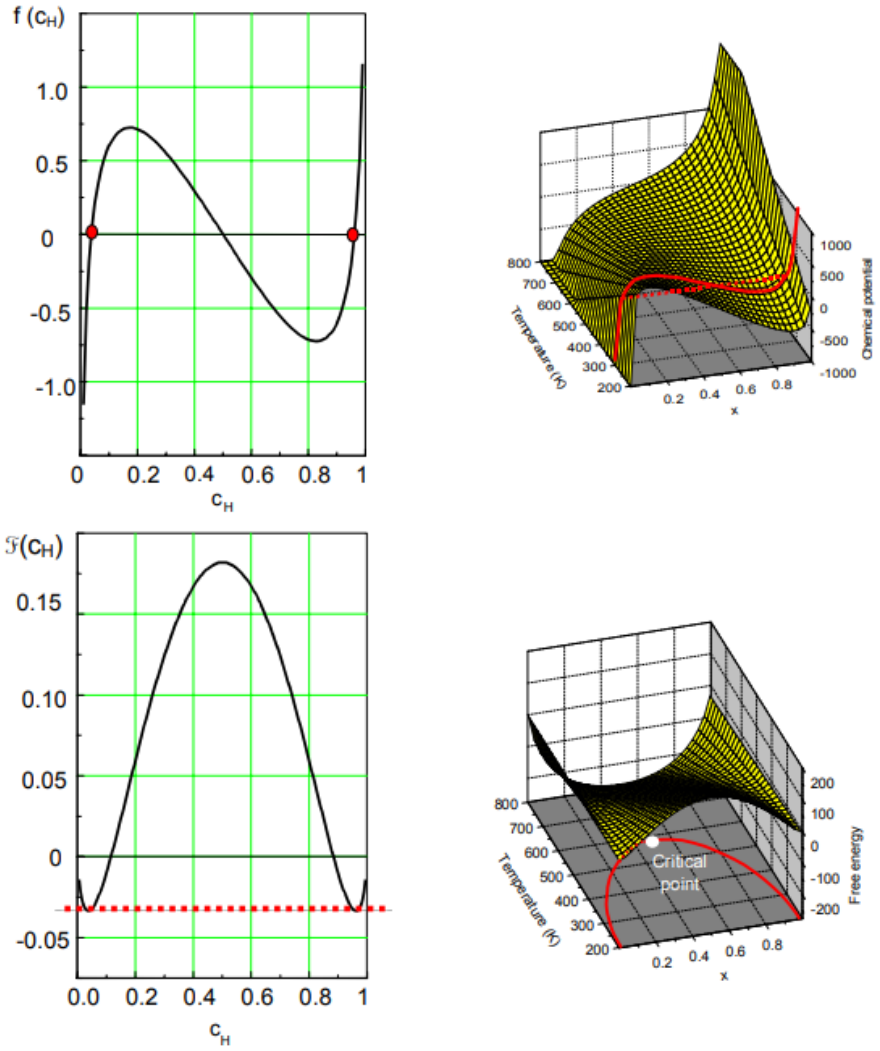

Figure 2.10: Equilibrium conditions for chemical potential and Helmholtz free energy in a hydride system (determined for $\frac{\epsilon n}{kT} = -7$).[19]

where $x_{\alpha(\beta)}$ is the fraction of the sample in the $\alpha(\beta)$ phase ($x_\alpha + x_\beta = 1$), and $c_{\alpha(\beta)} = \frac{N_H^{\alpha(\beta)}}{N^{\alpha(\beta)}}$. The two coexisting phases have concentrations c_i given by:

$$kT \ln \frac{c_i}{1 - c_i} + \epsilon n \left(c_i - \frac{1}{2} \right) = 0 \tag{2.27}$$

with $i = \alpha,\ \beta$ and corresponding dissociation pressure:

$$kT \ln \frac{p_{dis}}{p_0(T)} = 2\epsilon_0 + \epsilon n - \epsilon_b \tag{2.28}$$

Therefore, the natural logarithm of the dissociation pressure depends on the inverse of the temperature, which corresponds to van't Hoff equation (eq. 2.13).
Eventually, on can obtain the coexistence curve, which describes the conditions of temperature T and H fraction c_H such that the two phases coexist. This curve is is symmetric

relative to $c_H = 1/2$ with a maximum at $T = T_c$, which represents the critical temperature under which the phases can coexist. In the case of hydride formation, the critical temperature is mainly determined by the order of H-H interaction energy:

$$T_c = -\frac{\epsilon n}{4k} \tag{2.29}$$

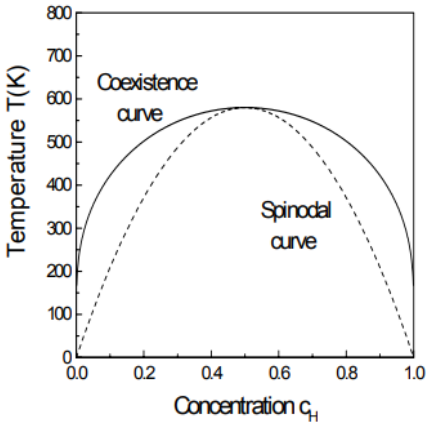

Figure 2.11: Coexistence curve and spinodal curve (determined for $\epsilon n = 0.2\ eV$).[19]

Generally speaking, this means that if at the beginning the system is found in the α-phase, external factors (exposure to H atmosphere in the present case) provoke the formation of a secondary phase β, which coexists with the first one at $T < T_c$; with increasing T, the β-phase nucleates and grows until the system has completely transitioned to the β-phase.

2.2.5 Miedema model

So far we have considered binary systems made of one type of metallic host lattice atoms and hydrogen. However, considering intermetallic compounds, the effect of alloying can often be rather important. Van Mal et al. (1974) and Miedema et al. (1976,1977) developed a model to describe the equilibrium thermodynamics of such systems. As explained in the previous section, in an intermetallic compound AB_n, only A forms a stable binary hydride. In a first approximation, one can consider $n \gg 1$, as it eases up the calculations. H atoms diffuse inside the compound, they will more easily interact with A atoms surrounding them, while $A - B$ bonds are easily broken to allow the formation of $A - H$ and $B - H$ ones, as depicted in Fig. 2.12.
As a result, the heat of formation of the hydride of an intermetallic compound depends on the heats of formation of the intermetallic compound itself and of the binary hydrides of the metals constituting the compound:

$$\Delta H\left[AB_nH_{2m}\right] = \Delta H\left[AH_m\right] + \Delta H\left[B_nH_m\right] - \Delta H\left[AB_n\right] \tag{2.30}$$

This approach works well to describe systems like $LaNi_5$. However, many interesting intermetallic compounds are of type AB, or AB_2, where the condition $n \gg 1$ is not satisfied. Thus a more general treatment is needed to describe them.

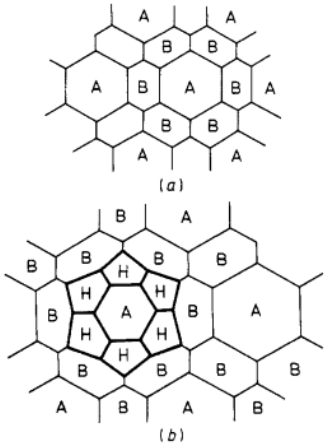

Figure 2.12: Schematic representation of the positions of hydrogen atoms in a ternary hydride formed from a compound AB_n.[21]

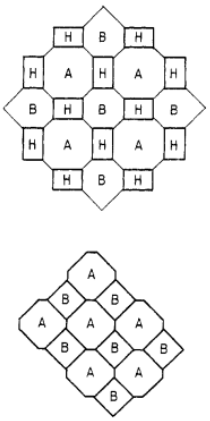

Figure 2.13: Schematic representation of the positions of hydrogen atoms in a ternary hydride formed from a compound AB.[21]

Considering an AB system (Fig. 2.13), it is clear that the situation is much different with respect to the previous one. Indeed, as H atoms prefer sites at which it is preferentially surrounded by A atoms, it is unlikely that all $A-B$ bonds will be broken during H absorption, and the number of hydrogen atoms per atom A absorbed by AB compounds is smaller than that for AB_n compounds with large n. These effects can be included in the model, leading to the generalized formula:

$$\Delta H\left[AB_nH_{x+y}\right] \;=\; \Delta H\left[AH_x\right] + \Delta H\left[B_nH_y\right] - (1-F)\,\Delta H\left[AB_n\right] \tag{2.31}$$

where $(1-F)$ is the number of broken $A-B$ bonds.[21]

2.2.6 Well-known hydrides

To gain a deeper understanding of the main features of hydrides, selected examples are described in the following.

Pd

Historically, Pd hydride has been the first to be studied, and thus has been extensively investigated through the years. Despite the wide research done on Pd-based hydride, its H storage capacity is inherently limited by the high mass of Pd, which reaches 0.6 wt%, and its cost is prohibitive for most applications.[11] Its crystal structure is face-centered cubic, with $Fm\bar{3}m$ space group, and a lattice constant of 3.890 $\dot{A}$. It can be easily activated, and when H atoms are absorbed, they occupy part of the available octahedral sites, leading to a lattice expansion equal to $\Delta V^{\alpha-\beta} = 1.57$ cm^3/g-atom of H. At H concentration $wt\% = \frac{[H]}{[Pd]}$ lower than 0.02, pure α phase exists, while for $wt\% \geq 0.6$ only pure β phase is present; for intermediate H concentrations, the solution is a mixture of the two phases. The enthalpy and entropy of formation of the Pd-H system are $\Delta H = -37$ kJ/mol$_{H_2}$ and $\Delta S = -92$ J/K·mol$_{H_2}$, respectively.[28][29]

$LaNi_5$

$LaNi_5$ is a hydride-forming alloy of type AB_5, characterized by a $CaCu_5$ crystal structure with a hexagonal lattice, and P6/mmm space group.[30] It forms tetrahedral interstitial sites to be occupied by absorbed H atoms. Its weight percentage can reach 1.5 wt%, the largest observed in the $CaCu_5$ family. It is characterized by versatile thermodynamic properties enabled by substitutional effects, high volumetric capacity, easy activation, a unique flat plateau with moderate hysteresis, rapid kinetics, resistance to poisoning and good cycle stability. As drawbacks, it has moderate gravimetric capacity, decrepitate to very fine powder and contain expensively and unevenly distributed elements in the earth. The enthalpy and entropy of formation of the $LaNi_5$ hydride are $\Delta H = -31$ kJ/mol$_{H_2}$ and $\Delta S = -110$ J/K·mol$_{H_2}$, respectively.[31][32]

2.3 The $TiFe_{1-x}Ni_x$ system

2.3.1 TiFe

TiFe crystal structure is of CsCl-type, space group $Pm\bar{3}m$, with a lattice parameter of 2.976 $\dot{A}$. It is usually produced by melting the elements at a high temperature, as it will be done in this study by Arc Melting. TiFe-based hydrides have been studied staring in the 1070s because of the conditions at which H-sorption occurs: at temperatures below 100°C and pressures lower than 100 bar. The study of their properties aims at achieving high storage capacities, mainly for stationary storage, since the mobile applications would be limited by the intrinsic large weight of the intermetallic compound. Moreover, lowering the equilibrium pressure of the alloy is a key challenge to allow hydride formation at milder conditions, which would be useful for the assembly of a standalone stationary energy storage system composed of an electrolyzer and a fuel cell. To reach this goal, stoichiometric tailoring can be applied, as done in this research by partial Ni-substitution,

as explained later.

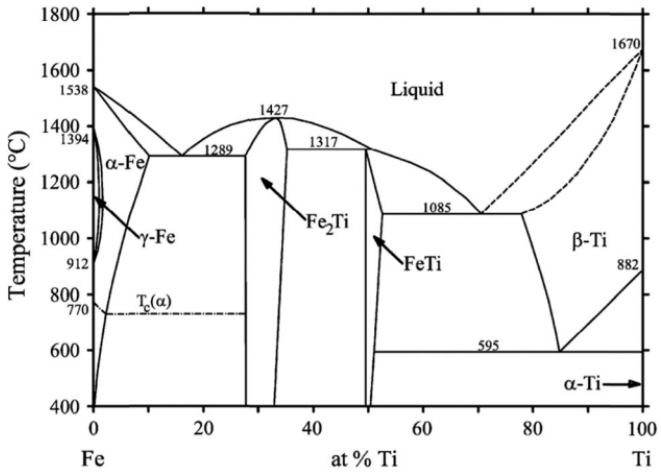

Figure 2.14: Fe–Ti phase diagram.[23]

TiFe hydrogen storage properties strictly depend on the composition and on the presence of secondary phases. Indeed, in the typical AB structure of the intermetallic compound, Ti is the A element, which forms stable hydrides, and Fe has the role of the B component, that only forms hydrides at very high pressure. Thus, depending on where we are in the phase diagram (Fig.2.14), different composition of the alloy are reflected on different hydride properties. TiFe alloy is an homogeneous solution in the narrow range going from 49.7 to 52.5 at% Ti. Adjacent phases are $TiFe_2$ (below 49.7 at% Ti) $TiFe_2$, and β-Ti (above 52.5 at% Ti). The Fe-rich one does not absorb hydrogen, while the latter is highly reactive. In fact, in Ti-rich alloys, like $TiFe_{0.9}$, the formation of β-Ti precipitates enables the H-sorption at ambient conditions without the need for long activation treatments. However, in general TiFe alloy is not easy to activate and requires a laborious treatment to allow the first hydrogenation. This is caused by the fact that TiFe is sensitive to air exposure, and passivating oxide and hydroxide layers are formed on the surface, hindering interaction with H. A. Santhosh et al.[26] modeled oxidized TiFe (100) surfaces with first-principle methods to understand which is the most convenient configuration for oxygen to be adsorbed; the preferred ones are in Fig.2.15.

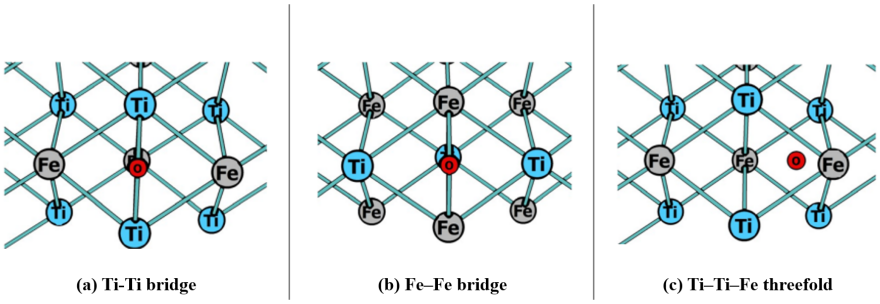

Figure 2.15: TiFe (100) oxidized surfaces.[26]

There are currently two distinct proposed activation models:

- Activation of air-exposed TiFe via the formation of TiO_2 and Fe clusters, since the latter provide a catalytic surface for H_2 dissociation;
- Segregated Ti–Fe–O oxide phases and clean TiFe surfaces formed freshly during desorption cycles provide catalytic means for H_2 intake, while no elemental Fe is formed in significant amounts.

In particular, the second description is confirmed by the fact that some Ti-rich oxide phases, like Ti_4Fe_2O, have a positive influence, since they react with H, facilitating its absorption. Additionally, the introduction of a foreign element to partially substitute Fe atoms seems to help. Indeed, a new element with a different oxygen affinity appears to induce selective oxidation and phase separation of Ti and Fe in the oxide layer, leading to a redistribution of major elements and inhibiting the formation of the thick, continuous passivating oxide layers found on pure TiFe, thus accelerating the activation process.[25] Furthermore, aside from thermal and mechanical treatments, also repeated absorption-desorption cycles have proved to be beneficial for activation, since they lead to alternate volume expansion and contraction and induce the crack of the passivating layer.[23]
Kinetics studies have confirmed the general aforementioned scheme for H-M interaction: hydrogen is chemisorbed on TiFe surface, from which it slowly diffuses through the hydride layer, while the nucleation and growth of the hydride occurs. Interestingly, H atoms present a very low diffusion coefficient, of the order of 10^{-12} cm^2s^{-1}, compared to the one measured on other hydrides (10^{-6}-10^{-8} cm^2s^{-1}); this can be attributed to the ordered structure restricting possible diffusion paths.
Four different hydride phases are found: α-solid solution, two monohydride phases β_1 and β_2 and a dihydride phase γ. The α phase maintains the same crystal structure as the alloy, with an enlargement of the unit cell volume. On the other hand, with the monohydride phases formation, the crystal structure becomes orthorombic. The difference between β_1 and β_2 phases resides in the occupancy of octahedral sites: the former corresponds to TiFeH, while the latter to $TiFeH_{1.4}$. The formation of the β-phases is related to the presence of strains induced by the absorption of hydrogen, as free-strain samples obtained by annealing generally show a single α-γ hydrogenation step. The transition to γ phase at higher H concentration was subject of debate, as the crystal structure was not clearly identified, but the latest experimental studies and theoretical calculations confirm that the orthorombic structure is maintained. The dihydride phase is formed at very high pressures, thus limiting the usage and the reversible capacity of this material. The absorbed H content depends on the synthesis method, going from a maximum of 0.3 wt% for amorphous TiFe, to 1.3 wt% for ball milled TiFe or 1.7 wt% for samples prepared via radio-frequency melting. Moreover, ball milled samples show a single plateau, while melted ones show two, suggesting the formation of both β and γ phases. Concerning the thermodynamics of the TiFe hydride, they also slightly vary depending on the different synthesis procedure applied. The first data available are related to the desorption process (in the absorption slightly lower values are expected): $\left|\Delta H_{des}^{\beta\to\alpha}\right| = 28.1$ kJ $mol_{H_2}^{-1}$, $\left|\Delta S_{des}^{\beta\to\alpha}\right| = 106$ J K^{-1} $mol_{H_2}^{-1}$, $\left|\Delta H_{des}^{\gamma\to\beta}\right| = 33.7$ kJ $mol_{H_2}^{-1}$, $\left|\Delta S_{des}^{\gamma\to\beta}\right| = 132$ J K^{-1} $mol_{H_2}^{-1}$. The entropy change for the first plateau is very low, and this could linked to the high strains that stabilize the β phase. Concerning cyclability, upon subsequent absorption-desorption

cycles, the hysteresis gap is reduced, but the γ phase is formed at higher pressures, until it disappears, leading to a decrease of the H capacity.[33][23]

2.3.2 Ni

Acting on the TiFe alloy composition with elemental substitutions, synthesizing a Ti-Fe-M' (where M' is a substituting transition metal) intermetallic compound can significantly change the hydride properties, improving activation process and cyclability, hydrogenation properties, lowering and stabilizing the plateau pressures, and reducing the gap between mono- and di- hydride plateau pressures. However, in many cases the substitution can cause severe drawbacks, for example improving thermodynamics while leading to H capacity reduction (M' = Zr, Cr), or lowering the monohydride plateau pressure while increasing the gap with respect to the second one (M' = Cu). All these effects will depend both the microstructure and on the formation of secondary phase precipitates, as seen for the basic TiFe alloy. It has been demonstrated that enlarging the TiFe cell parameter by elemental substitution is useful for the hydrogenation properties of TiFe, since H atoms can enter more easily in the host lattice, resulting in the lowering plateau pressure and milder activation conditions. Moreover, an important aspect in the choice of alloying elements is their availability and cost. This research is focused on the use of Ni to partially substitute Fe atoms. Nickel is a late transition metal which is considered a Critical Raw Material, thus it is not ideal for industrial upscaled materials. However, it presents many interesting features that can be beneficial for the TiFe-Ni compound, thus its study can help disclose the physics characterizing metallic hydrides, leading to a complete picture of new possible solutions for hydrogen storage. Indeed, Ni is known to improve hydride activation, kinetics, cyclability, and stability, making it possible to couple it to hydrogen production at ambient conditions.[25][23] This positive influence of Ni-substitution is a explained by a structural change occurring in the TiFe lattice, since Ti-Ni bond is weaker than Ti-Fe bond, leading to a larger lattice parameter ($a_{Ti-Ni} = 3.015$ $\dot{A}$,[34] $a_{Ti-Ni} = 2.976$ $\dot{A}$[23]), and a unit cell enlargement, which promotes H atoms absorption in the host alloy at milder conditions, while maintaining the same crystal structure of TiFe. This effect is described by Vegard's law:

$$a_{AB_{1-x}C_x} = (1-x)\, a_{AB} + x a_{AC} \tag{2.32}$$

This is an empirical law stating that the lattice parameter a of a solid solution of two constituents $AB_{1-x}B_x$ is approximately a weighted mean of the two constituent binary compounds lattice parameters, a_{AB} and a_{AC}, at the same temperature. In the present case, components A,B and C correspond to Ti, Fe, Ni, respectively, with constituent binary compounds TiFe and TiNi. For these reasons, samples of the form $TiFe_{1-x}Ni_x$ in a range of compositions (x = 0.05, 0.10, 0.15, 0.20, 0.30) are synthesized and characterized from the compositional, morphological and structural point of view; then thermodynamics and kinetics of hydrogen-sorption are studied. The importance of this research resides in the fact that it constitutes a comprehensive review of the hydrogen-sorption properties of $TiFe_{1-x}Ni_x$-based hydrides in a wide Ni concentration range, which is not available up to date.

Chapter 3

Materials and Methods

To fully characterize $TiFe_{1-x}Ni_x$-based hydride, the intermetallic compounds are first synthesized through Arc Melting and then characterized from the compositional, morphological and structural point of view with Scanning Electron Microscopy and X-ray Diffraction. H-sorption processes are analyzed with Differential Scanning Calorimetry and Sievert's measurements.

3.1 Samples synthesis

Elemental metals Ti and Fe in the form of grains, and Ni in the form of rods, were weighted to satisfy the composition requirements for each compound and compressed together to form a unique block, to be fused in the Arc Melter.

Arc melting

An Edmund B*ü*hler GmbH Compact MAM-1 Arc Melter was used to melt the Ti-Fe-Ni block. It has a water-cooled copper crucible plate to contain 5 to 20 g of material, and a tungsten electrode with a maximum temperature of 3500 °C, generating a maximum current of 450 A and an average current of 300 A. The chamber was pre-treated with Ar cycles, reaching the final pressure of 10^{-6} mbar. Three melting cycles are performed, then the sample is turned upside-down and the procedure is repeated; this is done meticulously to assure the homogeneity of the whole sample. Moreover, at each cycle a Ti getter is melted in such a way that, thanks to its high oxygen affinity, it absorbs the residual gas in the chamber, avoiding the formation of oxides in the samples.

Metallurgical treatment

Arc-melted samples are spheres with 3-4 mm diameter. They are split in two halves with MicroMet cutting machine and the flat surface is lapped with LSA ReMet polisher. The latter process is realized in multiple steps with gradually finer-grained aluminum foils, the last ones with the addition of Alumina. Lastly, they are encapsulated in polymeric resin to allow the compositional and morphological analysis of the circular section with Scanning Electron Microscopy. This procedure is done for all samples, except for $TiFe_{0.90}Ni_{0.10}$.

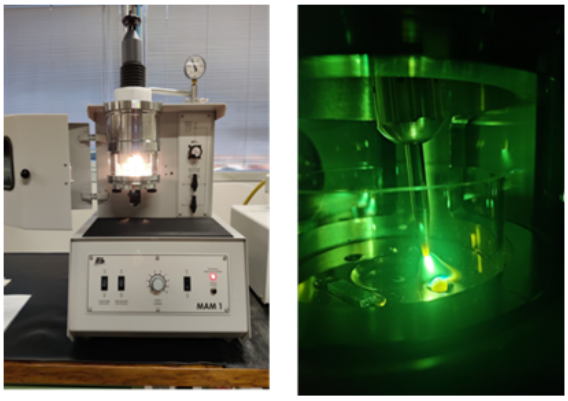

Figure 3.1: Arc Melter on the left and zoom on melting process on the right.

Figure 3.2: From left to right: Arc Melter, Automatic Mounting Press, Cutting Machine, Polisher.

Ball Milling

The milling procedure was carried out by introducing manually pulverized samples in a Spex CertiPrep 8000 Mixer/Mill, under air atmosphere, at standard pressure. Both pot and balls were made of hardened steel, in a ratio of balls-to-powder mass equal to 2:1. The milling time was maintained between 4 and 7 minutes for all samples. Ball milled samples are used in Powder X-ray Diffraction and in DSC measurements with the Differential Scanning Calorimeter and the Sievert's apparatus.
The list of synthesized samples is in Tab.3.1. Mass loss due to the procedure, including weighting and melting, was less than 1% of the initial value. For ball milled ones, the duration of the procedure is indicated, while non-ball milled ones have only gone through the metallurgical treatment.

Table 3.1: *Recap of synthesized samples.*
Sample mass is reported and, for ball milled ones, the duration of the treatment is indicated.

Composition	Sample	BM	Mass [g]
$TiFe_{0.95}Ni_{0.05}$	Ni05-a	✗	1.059(1)
	Ni05-b	5'	1060(1)
$TiFe_{0.90}Ni_{0.10}$	Ni10-a	✗	1.768(1)
	Ni10-b	7'	
$TiFe_{0.85}Ni_{0.15}$	Ni15-a	✗	1.170(1)
	Ni15-b	7'	8.827(1)
$TiFe_{0.80}Ni_{0.20}$	Ni20-a	✗	1.165(1)
	Ni20-b	7'	0.883(1)
	Ni20-d	✗	1.169(4)
$TiFe_{0.70}Ni_{0.30}$	Ni30-a	✗	1.069(1)
	Ni30-b	4'	1.068(1)

3.2 Morphological, compositional and structural characterization

3.2.1 Scanning Electron Microscopy

The morphological and compositional analysis of arc melted samples has been performed with a Leica Cambridge Stereoscan 360 SEM, equipped with a tungsten electron-emitting filament. Electrons interact in different ways with the sample, depending on their energy and depth, giving various type of information. Three experiments are possible with this instrument: Secondary Electron (SE) Analysis, Energy Dispersive X-ray Spectroscopy (EDX) and Backscattered Electron (BE) Analysis (not used in this context). The former technique is based on the fact that primary electrons can ionize specimen atoms that emit low energy secondary electrons (typically 3–5 eV), which can only escape from a region within a few nanometers of the material surface; their flux is measured by an Everhart Thornely detector. This signal gives topographic information on surface texture, roughness and morphology in general. Data concerning the composition were collected through EDX: an inner shell electron is displaced by collision with a primary electron and an outer shell electron will fall into the hole left in the inner shell to return to ground state by the emission of an X-ray photon. Emitted radiation is measured by an Oxford Instrument 7060 EDX detector, and analyzed the INCA Oxford Instrument software. Two types of microanalysis are possible through EDX:

- local analysis
  This type of measurement is done by focusing on an area on the surface and by selecting on it the regions to separately characterize; this method is fast since each spectrum is detected in 2-3 minutes.

- compositional map
  This analysis consists in characterizing the composition of the whole selected area,

by exposing it to the primary electron beam for about 1 hour; maps allow to have a complete and precise analysis of the selected area.

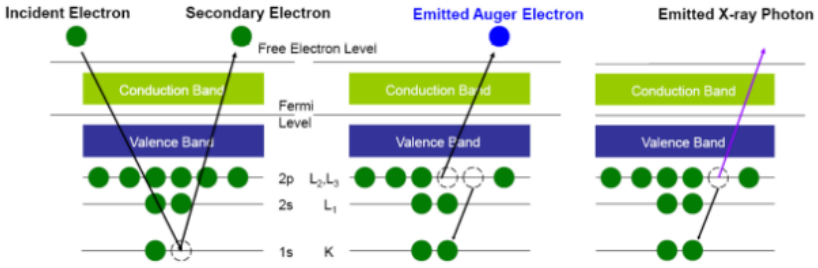

Figure 3.3: Secondary signals from interaction of the sample with primary electrons: secondary electrons, Auger electrons (not studied here), X-rays.

3.2.2 Powder X-ray Diffraction

The structural characterisation has been carried out on ball milled samples with an X'Pert Pro PANalytical X-ray diffractometer, Bragg-Brentano geometry, Cu K-α source with Ni and Cu filters, 1/2° slits.
The experiment is based on diffraction of X-rays by atoms in the crystal structure, which is described by Bragg's Law:

$$n\lambda = 2d\sin\theta \tag{3.1}$$

where n is an integer multiple of λ, that is the wavelength of the X-rays beam, d is the lattice parameter (distance between two crystal planes), θ is the angle formed between the direction of the incoming beam and the one normal to the crystal plane. The process is depicted in Fig. 3.4

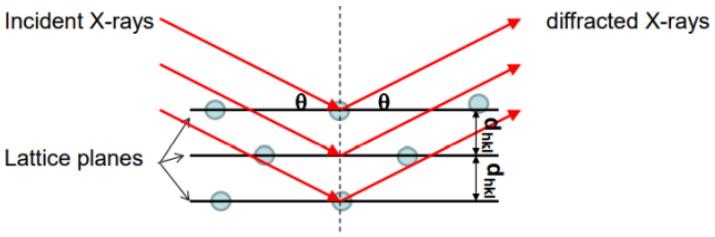

Figure 3.4: X-ray diffraction from a crystal.

The X-rays source is an X-ray tube where electrons emitted from an anode collide with a metal source, generally made of Cu, which emits spectral lines corresponding to the excitation of inner-shell electrons of the metal $k\alpha$ at λ =1.5406 $\dot{A}$ (energy E = 8.04keV). Since the sample is in powder form, every possible crystalline orientation is equally represented in it, making it isotropic. Powder X-ray Diffraction operates under the assumption that the sample is randomly arranged. Therefore, a statistically significant number of each plane of the crystal structure will be in the proper orientation to diffract the X-rays, and each plane will be represented in the signal. Bragg-Brentano geometry (Fig. 3.5) offers high-resolution and high beam-intensity analysis at the cost of very precise alignment

requirements and carefully prepared samples. The incident angle θ between X-ray source and the sample is always $1/2$ of the detector angle. There are two possible working modes:

- $\theta : 2\theta$ scan: with X-ray tube fixed, the sample rotates at θ/min and the detector at double velocity;
- $\theta : \theta$ scan: the sample is fixed and the tube rotates at the same rate as the detector at θ/min;

In the experiment, the second one is used, with 2θ varying in the range $[28 - 114]°$. Sample surface is kept on the tangent plane of the focusing circle defined by three spots at sample, X-ray source and receiving slit. The incident- and diffracted-beam slits move on a circle that is centered on the sample.

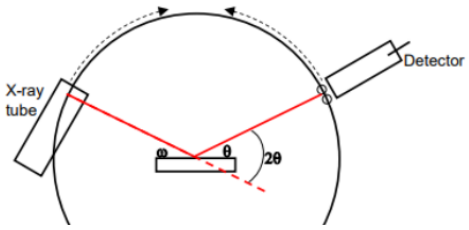

Figure 3.5: Bragg-Brentano geometry for Powder X-ray Diffraction.

In this way, the detector measures the diffracted radiation and plots the signal intensity with respect to 2θ. Results were first visualized with the High Score Plus software[35] and then analyzed through MAUD software,[36] through Rietveld's refinement method. This technique to analyze diffractograms was first introduced in 1967[37] and uses the least squares method to refine a theoretical line profile until it matches the measured profile; from this fit, it is then able to get information on the concentration of each element/phase, the crystallite size and the lattice parameters from the intensity, the width and position of the peaks, respectively. To account for preferential orientation, March-Dollase algorithm was used. Eventually, the 3D crystallographic rendering was realized with VESTA.[38]

3.3 H-sorption analysis

3.3.1 High-Pressure Differential Scanning Calorimetry

High-Pressure Differential Scanning Calorimeter (HP-DSC) measures the heat flow associated with material transitions as a function of temperature and time, providing both quantitative and qualitative data on endothermic and exothermic processes. The instrument used in this study is a TA Instruments Q10 DSC and data are visualized with TA Instruments Universal Analysis Software.

The apparatus

The main component of the instrument is the DSC cell, whose structure is depicted in Fig. 3.6. The cell has a volume of 3.4 mL, enclosed in a steel cylinder that can be

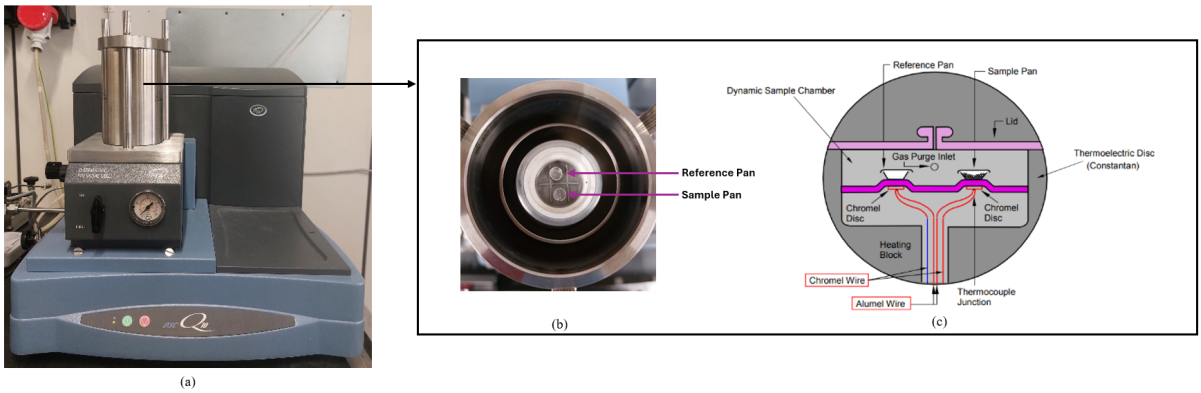

Figure 3.6: (a) TA instruments DSC Q10, (b) DSC cell from above, and (c) schematic representation of the internal structure of the DSC cell.

pressurized up to 70 bar (it will be used under 50 bar in the present experiments). It has two gas flow control valves, a three-way valve, a pressure gauge, a pressure release valve, and gas pressure fittings on the side. The cell contains a pressure transducer which continuously measures actual sample pressure. Gas inputs are connected to high-purity H_2 and Ar. The latter is used to purge the DSC cell before experiments, to eliminate internal impurities that can alter the experiment. The sample, of mass between 0.5 and 100 mg, is encapsulated in an Aluminum pan, since the high melting point of this material (660°C) allows to work at high temperatures. The sample pan and an empty reference pan, also made of Al, sit on two separate platforms raising from a constantan thermoelectric disk surrounded by a furnace. The furnace will set a temperature T_{fs} and T_{fr} in the position corresponding to the sample and the reference pans, respectively. At the same time, resistances R_s and R_f are created between the heating block and the platforms supporting sample and reference pans, respectively. Finally, on the platforms, reference and sample are at temperatures T_s and T_r. Two area thermocouples with chromel disk contact monitor the sample and reference temperature, with an accuracy of $\pm$ 0.1°C.
The heat flow associated with the sample is:

$$q_s = \frac{T_{fs} - T_s}{R_s} \tag{3.2}$$

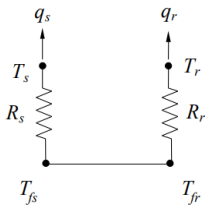

Figure 3.7: Heat flow measurement procedure.

and that associated with the reference is:

$$q_r = \frac{T_{fr} - T_r}{R_r} \tag{3.3}$$

and finally $q = q_s - q_r$.
Assuming that thermal resistances associated to sample and reference are identical ($R_s = R_f = R$), and the temperature of the furnace is constant in correspondence of sample and reference ($T_{fs} = T_{fr} = T_f$), the differential heat flow, corresponding to the heat of reaction, is obtained using the thermal equivalent of Ohm's Law:

$$q = \frac{\Delta T}{R} \tag{3.4}$$

If $T_s = T_r$, no phase transformation occurred, otherwise some process is taking place in the sample. If during a heating (cooling) ramp $T_s < T_r$ ($T_s > T_r$) it means that, even if the furnace is trying to increase (decrease) the temperature, T_s is blocked at a constant temperature, which means a phase transformation is occurring.

HP-DSC measurements and data analysis

After the pulverized sample of a mass of about 20 mg has been encapsulated ans positioned in the DSC cell with the reference pan, measurements can start. The following parameters have to be set:

- H_2 pressure;
- temperature range to analyze;
- rate of heating/cooling.

The latter parameter is measured in °C/min and determines both the speed of the procedure and the quality of the signal: a fast rate (like 10 °C/min) will allow a fast measurement, but a very broad peak, since the speed of ramp is greater than that of the reaction kinetics; on the other hand a slow rate (2 °C/min) would allow a slow measurement, maintaining near-equilibrium conditions, leading to a more precise result, at the price of a large time cost. Thus a compromise can be found by setting 5 °C/min, which is often used in hydride DSC studies in literature[39] and seems to allow good measurements. The resulting data consist of the heat flow, measured in W with a sensitivity of 0.1 μW, as a function of temperature (°C), which first increases in the heating ramp, and then decreases during cooling.

The detection of a positive heat flow signal corresponds to an exothermic process, which in the case of hydrides corresponds to hydrogen absorption by the sample, causing energy release due to formation of new bonds of the sample atoms with hydrogen; inversely, a negative peak corresponds to an endothermic process indicating the hydrogen desorption from the sample, during which energy is needed by the sample to break H-M bonds. From the qualitative point of view, different conclusions can be reached. For instance, the presence of more than one peak indicate the occurrence of more than one transition, and a sharp or a broad peak can indicate a fast or a slow reaction, respectively. From data analysis one can get the following quantitative information:

- enthalpy of reaction
- onset temperature of absorption/desorption process
- equilibrium pressure of absorption/desorption process

Even though DSC is a non-equilibrium measurement, and thus the directly exchanged heat does not resemble the heat of formation/decomposition, it is possible to extract the heat of formation/decomposition of hydrides. Assuming quasi-equilibrium conditions, the Gibbs free energy of the transformation is null:

$$\Delta G \;=\; \Delta H - T_{eq}\Delta S \;=\; 0 \;\;\Longrightarrow\;\; \Delta H \;=\; T_{eq}\Delta S \tag{3.5}$$

where T_{eq} is the temperature at which the process occurs, which coincides with the onset temperature of the non-zero heat flow signal, if we only consider thermodynamics. Since in general $\delta Q \;=\; T\Delta S$, eq.3.5 also implies that the enthalpy of reaction can be found by integrating the heat flow signal with respect to time. However, this type of result is difficult to obtain when the sample is a hydride-forming compound, and often leads to lower values than the expected heat of reaction.[39][40] A more reliable approach is the van't Hoff analysis: more measurements at different pressures are performed for the same sample, and the equilibrium pressure and temperature found for each dataset are fitted with eq.2.13. Rongeat et al.[39] determined T_{eq} by using the derivative of the curve or, in some cases, by taking the intersection between the background line and the slope of the peak. Anyway, this method is not always trivial to apply, since in many hydrides the onset could be determined more by the kinetics than by the thermodynamics of the system. Moreover, the process may present multiple peaks, which are not easy to isolate and identify. Thirdly, in the case of noisy measurements it is difficult complete such analysis. Concerning the equilibrium pressure, ideally the pressure set in the DSC should be constant, but since the temperature is varied, it changes in agreement with the ideal gas law:

$$p \;=\; \frac{nR}{V}T \tag{3.6}$$

where $R = 83.14$ bar cm^3 mol^{-1} K^{-1} is the ideal gas constant. In addition, pressure leaks in the DSC pipelines could alter the detected pressure value. Therefore, a new approach to extract meaningful equilibrium pressure and temperature has been developed in this study. Basically, all the non-zero signal $\phi^{abs/des}(t)$ $[W]$ (independently on the number of peaks present) is considered to be related to the H-sorption process, and is integrated

with respect to time leading to $\Delta H_{int}^{abs/des}$ $[J]$:

$$\Delta H_{int}^{abs/des} = \int_{peak\ start}^{peak\ end} \phi^{abs/des}(t)dt \tag{3.7}$$

Then, the half-reaction temperature and pressure parameters are extrapolated in such a way that $\Delta H_{h.r.}^{abs/des} = \Delta H_{int}^{abs/des}/2$. The half-reaction point is taken as a reference since it represents the intermediate conditions at which the transformation occurs, thus giving a correct estimation of the equilibrium parameters. Finally, the temperature found for the absorption reaction ($T_{h.r.}^{abs}$) and that related to the desorption ($T_{h.r.}^{des}$) are averaged, to obtain a unique parameter for the dataset, and the same is done for the pressure:

$$\begin{cases} T_{h.r.} = \frac{T_{h.r.}^{abs}+T_{h.r.}^{des}}{2} \\ \\ p_{h.r.} = \frac{p_{h.r.}^{abs}+p_{h.r.}^{des}}{2} \end{cases} \tag{3.8}$$

Eventually, eq.2.13 is used to fit the data and determine both enthalpy and entropy of reaction:

$$\ln\left(\frac{p_{h.r.}}{p_0}\right) = \frac{\Delta H}{RT_{h.r.}} - \frac{\Delta S}{R} \tag{3.9}$$

Instrument calibration

To obtain accurate experimental results the DSC cell must be calibrated when it is first installed and periodically after that. In the Q10 DSC, the calibrations to perform are the following:[41]

(1) **cell constant calibration**
In this this calibration procedure, a standard metal is heated through its melting transition in the same gas atmosphere that will be used in the experiments. The calculated heat of fusion is compared to the theoretical value, and the cell constant is the ratio between these two values.

(2) **temperature calibration**
Temperature calibration is obtained by the previous procedure: the extrapolated onset of the recorded melting point of the standard metal is compared to the known melting point, and the difference is calculated for temperature calibration.

(3) **baseline calibration**
The baseline slope and offset calibration involves heating an empty cell through the entire temperature range of interest for subsequent experiments, holding isothermal at the temperature limits; the calibration program is used to calculate the slope and offset values needed to flatten the baseline and zero the heat flow signal

Calibrations (1) and (2) are performed using In as a standard metal, under H_2 atmosphere, and leads to a cell constant value of 1.8, which is automatically applied in the subsequent measurements. Even after calibration (3), the presence of a non-zero baseline was observed in some experimental runs. This can be due to the presence of artifacts and spurious signals that the automatic software procedure is not able to account for. This can also

happen when the signal is close to the limits of the investigated temperature range. In addition, most automatic correction procedures are not based on a physical consistent model. Therefore, an additional correction was added in the data analysis to remove it, following the method described by A. Cisse et al.[42] and depicted in Fig.3.8, based on the calculation of a cubic spline fit with boundary conditions given by the pre- and post- peak signal slope. A more accurate description can be found in Appendix A1.

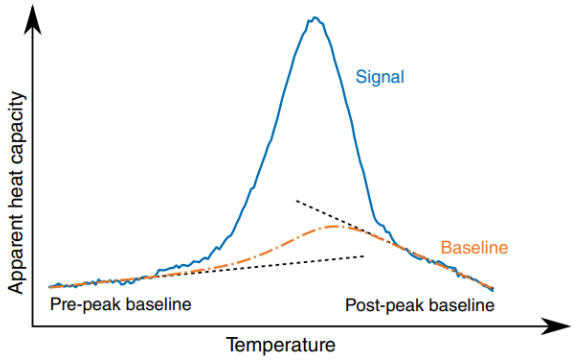

Figure 3.8: Baseline removal method.[42]

3.3.2 Sievert's measurements

Sievert's measurements are fundamental to determine another important feature of hydrides: their weight capacity. Since in solid state hydrogen storage research masses of the order of mg are generally studied in a wide range of temperature and pressure, high precision and accuracy are required to perform capacity measurement. In this framework, volumetric Sievert's measurements are the best method to be applied: fixed pressure and temperature are set in a known reference volume, separated form the sample by a valve; when the valve is opened, hydrogen will flow following the pressure gradient and its uptake/release is detected from changes in the pressure.[43] The Sievert's apparatus is deployed in the present work, exploiting the volumetric measurement technique. The setup is controlled by the Hydrogen Sorption Analyser (HSA) software based on the LabVIEW.[44]

The apparatus

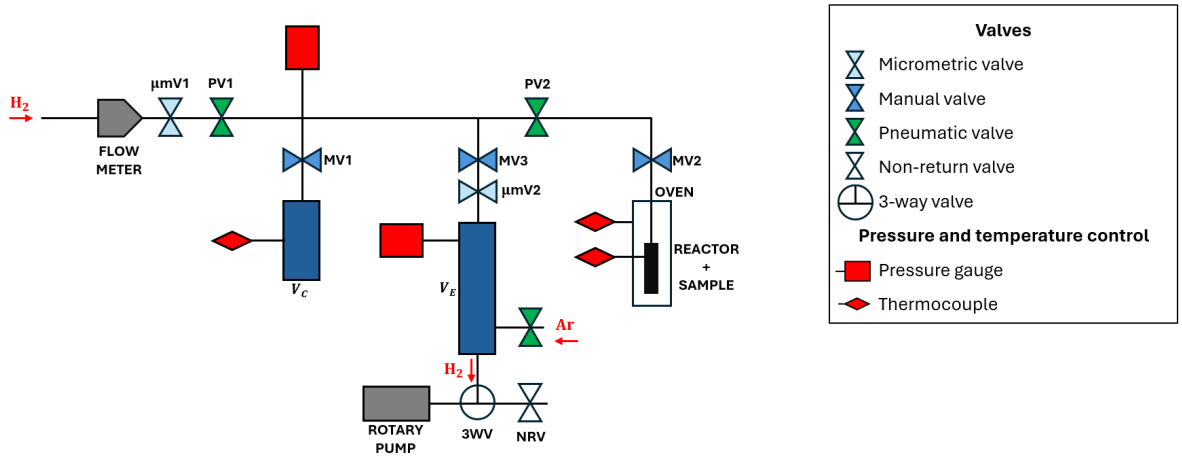

Figure 3.9: Schematic representation of the Sievert's apparatus.

The Sievert's apparatus, depicted in Fig.3.9, is now explained following the hydrogen path inside of it. First, a flow-meter (El-Flow by Bronkhorst) and a micrometric valve (μmV1) regulate the H_2 flow. The μmV1 is kept to its minimum to have a good control of the gas inlet. Then, the pneumatic valve PV1, controlled by the software, allows the gas flow to enter the rest of the system. Its internal structure is composed of solenoid valves where a piston can move on the vertical direction controlled by 6 bar of air, closing or opening the passage for H_2. If PV1 is open, the gas expands until it reaches the manual valve MV1, the pneumatic valve PV2 and the manual one MV3. MV1 connects the system, to the calibrated volume V_C, which has known volume and controlled temperature. It is used as a reference to measure the whole volume of the apparatus, as will be explained, and can be included in experiments by leaving MV1 open.
PV2 is controlled by the software and connects the system to the oven, which contains reactor with the sample holder inside. A manual valve MV2 is present to isolate the reactor from the rest of the volume. In addition, a capillary pipe is used for this connection, to

avoid temperature gradients between the oven and the apparatus and unused passive volumes. The oven has a resistor with a maximum range of 500°C surrounding the inner core and a thermal insulator as a coating. The reactor is made of stainless steel and can operate at high-temperature and pressure operations. To avoid gas leaks, both a silver thread improving element lubricity a thin silver ring (gasket) which acts as a vacuum seal between the body and the female cap are added. The gasket is provided with a filter, avoiding powder spreads inside the apparatus. The sample holder is a stainless steel cylinder hosting the powder and allowing hydrogen to flow in and out.
MV3 is the valve regulating the expulsion of the gas from the apparatus; it is connected through the micrometric valve μmV2 to the expansion volume V_E, linked to a rotary vacuum pump. μmV2 is kept to its minimum during the experiment, when H_2 must be kept inside the system, and is gradually opened to allow its exit. In the first step of the exhausting procedure, which aims to reduce hydrogen pressure inside the system to values that can be accepted by the rotatory pump, a three-way valve interrupts the connection between V_E and the rotary pump, while directly connecting the former to a non-return valve. In this configuration, H_2 enters the expansion volume and is mixed with argon (whose flow is regulated by another pneumatic valve), to be ejected. Then, the rotatory pump is connected again to V_E and vacuum is performed once again in the volume.
Pressure and temperature of the system are measured by pressure gauges (MKS Baratron capacitive manometers) and thermocouples (type K), respectively. The first of the two pressure sensors (MKS 750D) is connected to the Sievert pipelines and can measure up to 70 bar; the second one (MKS 722A) is linked to the expansion volume, to control the gas exit. The three thermocouples operate in a range of -200°C to 1200°C and are connected to the reactor walls, the oven and the external surface of V_C.

Experimental procedure and data analysis

The Sievert's apparatus allows to perform equilibrium measurements which measure the H_2 pressure as a function of the absorbed (desorbed) gas quantity at a fixed temperature, called Pressure-Composition Isotherms (PCI). To simplify the description, we define V_{cx} the volume delimited by PV1, PV2 and PV3, and V_{cxt} the same volume with addition of the pipeline until MV2. During an absorption measurement, the following steps are done:

(1) pressure in V_{cx} is set at $p^1_{cx}(0)$, starting from 0 bar

(2) wait for the pressure stabilization in V_{cx} at p^1_{cx}

(3) PV2 is opened, thus H_2 reaches the sample holder, occupying the volume V_{cxt} and the reactor

(4) wait for the pressure stabilization in the whole volume at p^1

(5) PV2 closed

(6) steps from (1) to (5) are repeated, increasing the pressure each time, reaching the maximum pressure of 50 bar

Thus, at the k^{th} repetition cycle, the section going from the PV2 (closed) to the reactor is at the pressure p^{k-1}, while the pressure in V_{cx} is set to p^k_{cx}. Applying the ideal gas law

(eq. 3.6), the number of H_2 moles before (n_i^k) and after (n_f^k) the PV2 opening can be calculated as follows:[45]

$$\begin{cases} n_i^k &= \frac{p_{cx}^k V_{cx}}{RT_{cx}} + \frac{p_{cxt}^{k-1}(V_{cxt}-V_{cx}+V_{\Delta T})}{RT_{cxt}} + \frac{p_{cxt}^{k-1}(V_{sh}-V_s-V_{\Delta T})}{RT_{sh}} \\ n_f^k &= \frac{p^k(V_{cxt}+V_{\Delta T})}{RT_{cxt}} + \frac{p^k(V_{sh}-V_s-V_{\Delta T})}{RT_{sh}} \end{cases} \tag{3.10}$$

where V_{sh} and T_{sh} are the volume and temperature of the sample holder, and V_s is the volume occupied by the sample, which depends on its mass and density: $V_s = \frac{\rho_s}{m_s}$. Pressure and temperature of each part are constantly monitored by the relative pressure gauges and thermocouples and saved by the software. The $V_{\Delta T}$ volume accounts for temperature gradients in the capillary tube between MV2 and the oven: because the temperature of the oven is in higher than that in the rest of the apparatus (T_{cxt}), the fraction of the line near to MV2 is considered to be at T_{cxt}, while the remaining part, near to the oven, is at T_s. From eq.3.10 one can find the number of H_2 moles absorbed in the k^{th} cycle:

$$\Delta n^k = \left| n_i^k - n_f^k \right| \tag{3.11}$$

By plotting the pressure at each cycle as a function of Δn^k, the PCI is obtained. The main information to be extracted from it is the hydrogen capacity of the sample. As a matter of fact, from eq. 3.11, the total quantity of absorbed hydrogen can be found:

$$\Delta n = \sum_k \Delta n^k \tag{3.12}$$

In the end, the hydrogen concentration c_H is given by the wt%:

$$c_H = \frac{m_{H_2}}{m_s} \times 100 = \frac{\Delta n \cdot m_{H_2}^{mol}}{m_s} \times 100 \tag{3.13}$$

where $m_{H_2}^{mol} = 2.016$ g mol^{-1} is the hydrogen molar mass. The same procedure is followed for the desorption measurements, where the pressure p_{cx}^k is decreased at each time in the range from 50 to 0 bar.
Different factors can influence and jeopardize measurements:

- **pressure leaks and temperature oscillations**
  Both can alter the results of this experiment, leading to a wrong evaluation of c_H. However, a good isolation of the measuring apparatus should reduce spurious signals, and the presence of precise sensors allow to monitor them and to understand if the variations correspond to an actual hydrogen uptake (desorption). The thermocouples connected to the reactor walls and the oven have a sensitivity of ±1°C, while the one at the external surface reach ±0.1°C, and the MKS 750D pressure gauge has an accuracy of 1% on the reading. The latter is crucial to determine the uncertainty on the hydrogen capacity of the sample.

- **gas impurity**
  Impurities can lead to unwanted events, since they can interact with the sample, hindering its reaction with hydrogen, or they might absorb the gas themselves. To avoid this, the hydrogen input line is directly connected to high-purity (99.99% H_2)

gas, and purification procedure with an inert gas like argon must be executed after each absorption-desorption measurement; also, the system exposure to air should be avoided.

- **non ideality of the gas**
  The deviation of a real gas from an ideal gas is represented by the compressibility factor Z, defined as defined as the ratio of the molar volume of a gas to the molar volume of an ideal gas at the same temperature and pressure. The corrected gas law is then:
  $$pZV = nRT \tag{3.14}$$
  The deviation from ideal behavior becomes more significant at lower temperatures or larger pressures. When approaching pressures around 50 bar, van der Waals's equation should be used:
  $$\left(p + \frac{an^2}{V^2}\right)(V - nb) = nRT \tag{3.15}$$
  where $a = 0.2476$ L^2 bar mol^{-2} is the molecular interaction parameter and $b = 0.02661$ L mol^{-1} is the co-volume of the hydrogen molecules. Anyway, these corrections are appreciable only for pressures higher than the ones used in the experiments.

- **internal volumes**
  The apparatus volume must be accurately chosen for pressure variations detection, also based on the amount of sample: for example, since a smaller hydride quantity will absorb/desorbed less H_2, a reduced volume is needed to detect it more precisely. At the same time, the apparatus volume must be sufficiently large so that the pressure change resulting from hydrogen absorption or desorption does not halt the process before complete hydrogenation or dehydrogenation of the sample. Precise determination of the volumes is also required to achieve measurement accuracy. In doing this, also valves internal volumes must be considered, since opening/closing a valve causes a slight variation of the real volume of the system.

Uncertainty on the final measured capacity value ($\mathcal{Y}$), can be determined by propagation of errors on p, V, T, and m_s ($\mathcal{X}_i$), through the formula:

$$\delta\mathcal{Y} = \mathcal{Y}\sqrt{\sum_i \left[\left(\frac{\delta\mathcal{X}_i}{\mathcal{X}_i}\right)\right]^2} \tag{3.16}$$

Volume determination

Starting from a known calibrated volume V_c (which also contains the pipeline until MV1 closed), the rest of the Sievert's apparatus volume is measured in the following way (assuming all valves are initially closed and the system is in vacuum):

- V_{cx} is filled with MV1 open, while all other valves are closed, up to a pressure p_{V_c}
- MV1 is closed to isolate V_c and vacuum is done in the remaining $V_{cx} - V_c$ volume

- MV1 is opened: the H_2 gas occupying V_c expands in V_{cx} following Boyle's law:

$$p_{V_c} V_c \;=\; p_{V_{cx}} V_{cx} \tag{3.17}$$

  From this, since $p_{V_{cx}}$ is measured by the pressure gauge, V_{cx} can be found.

- the same procedure is done by opening PV2 to measure V_{cxt}, and then by opening MV2 to measure V_{TOT}.

Note that, apart from V_c, all volumes are measured with opened valves in the corresponding portion of space: V_{cx} comprehends the internal volume of the opened MV1, V_{cxt} contains also that of PV2, and V_{TOT} also depends on that of MV2. As a consequence, each time a valve is closed, the isolated volume, obtained by subtraction, accounts for the loss of valves dead volumes.

Background calibration

Background calibration is done by applying the absorption-desorption measurement procedure without sample. In this condition, since no sample-H interaction occurs, one would expect a null Δn from eq. 3.12. In reality, this is not true due to the aforementioned error sources. Thus, it is useful to extract the background signal, to be subtracted to the signal resulting from actual measurements. This is done by collecting PCIs at 30, 60, 100 and 150°C, allowing to determine a p-V-T map for the background signal.

Chapter 4

Results and Discussion

4.1 Compositional and morphological characterization

Compositional homogeneity was verified in all the samples through EDX local microanalyses performed on different regions of the sample surface, and on the same scale to have the same accuracy. The results are averaged over all spectra and the error is given by the standard deviation, and are summed up in Tab.4.1. No oxide phases related to the air exposure of the alloy were identified, possibly due to the low abundance of them, coupled with the low sensitivity of this technique in identifying light atoms (Z<11). Indeed, as the atomic number is reduced, it becomes increasingly difficult to ionize an atom, and even if this occurs, it is less likely to generate an X-ray energetic enough to escape the surface, which results in a weaker signal from the light elements. Oxygen was only identified in the presence of Al, like in sample Ni30-a (Fig.4.1), indicating that its presence is due to the polishing treatment with Alumina, whose chemical formula is Al_2O_3. This hypothesis is also confirmed by the absence of O-Al phases in sample Ni10-a, which was the only one not treated with Alumina. Some regions with higher-Ti concentration (up to 60 at%) where spotted in samples Ni15-a and Ni30-a. These can be due to imprecision in the sample weighting procedure or to the formation of Ti-rich phases due to insufficient Arc Melting time. Apart from these rare exceptions, the overall analysis demonstrates the samples homogeneity. This is also confirmed by the qualitative uniformity of the elemental maps reported in Fig.4.3 and by the measured elemental atomic fractions, in agreement with Tab.4.1. Concerning the morphological analysis based on SE samples Ni05-a, Ni20-a, and Ni30-a show smooth and clean surfaces (Fig. 4.4 (a), (d), (e)), differently from Ni10-a and Ni15-a (Fig. 4.4 (b), (c)). However, SE contrast does not correspond to variations of composition (Fig.4.2), therefore it must be of purely morphological origin, likely associated with surface roughness. Thus, the metallurgical treatment must be at the source of such superficial features. In particular, sample Ni10-b did not undergo the procedure, as its numerous morphological defects demonstrate. Samples Ni15-b and Ni20-b were lapped and polished manually, and the results are gradually improved. Only Ni05-b and Ni30-b were treated with the automatized procedure, and in fact their surfaces are smoother than the others.

Table 4.1: *Samples compositions measured by EDX.*
Expected and measured samples compositions, and atomic percentages of the elements are reported (uncertainty on the experimental values is in parentheses).

Sample	Expected composition	Measured Composition	Ti [at%]	Fe[at%]	Ni [at%]
Ni05-a	$TiFe_{0.95}Ni_{0.05}$	$TiFe_{0.92}Ni_{0.05}$	50.8(3)	46.6(3)	2.7(1)
Ni10-a	$TiFe_{0.90}Ni_{0.10}$	$TiFe_{0.87}Ni_{0.10}$	50.9(1)	44.1(1)	4.9(1)
Ni15-a	$TiFe_{0.85}Ni_{0.15}$	$TiFe_{0.78}Ni_{0.13}$	52.1(3)	41.0(2)	6.9(3)
Ni20-a	$TiFe_{0.80}Ni_{0.20}$	$TiFe_{0.76}Ni_{0.19}$	51.5(2)	38.9(2)	9.6(1)
Ni30-a	$TiFe_{0.70}Ni_{0.30}$	$TiFe_{0.66}Ni_{0.29}$	51.2(3)	34.0(3)	14.8(2)

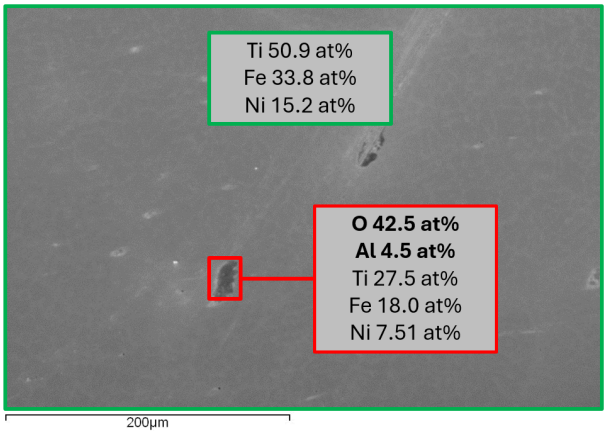

Figure 4.1: Example of O-Al oxide phase found in Ni30-a. Red square is related to the region where the O-Al phase was found. Green square contains data related to the average of analyses in the remaining area (4 in total).

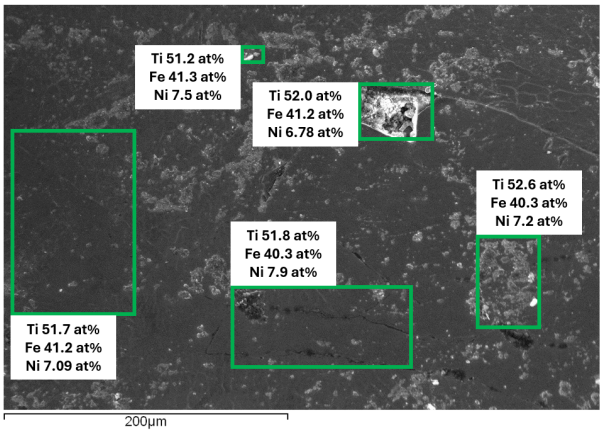

Figure 4.2: EDX analysis of Ni15-a sample, which shows absence of correlation between SE contrast and composition.

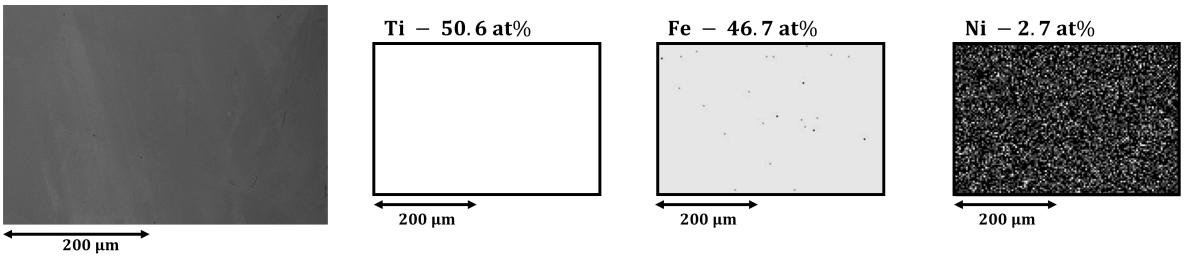

(a) **Ni05-a**

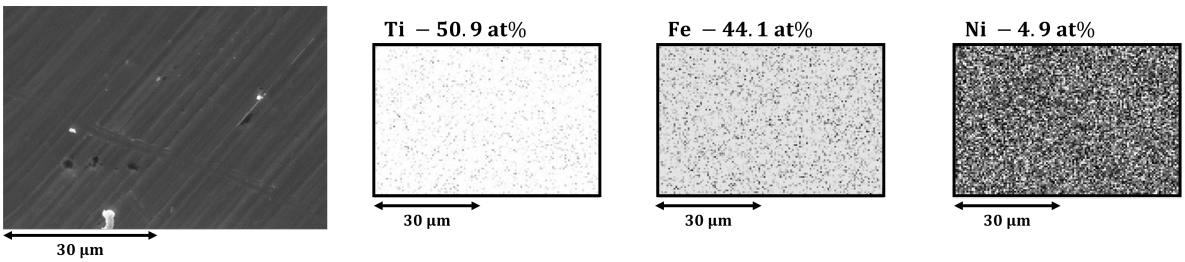

(b) **Ni10-a**

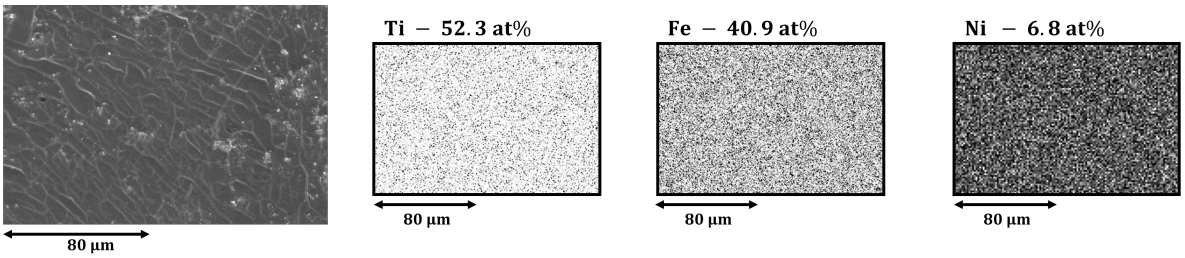

(c) **Ni15-a**

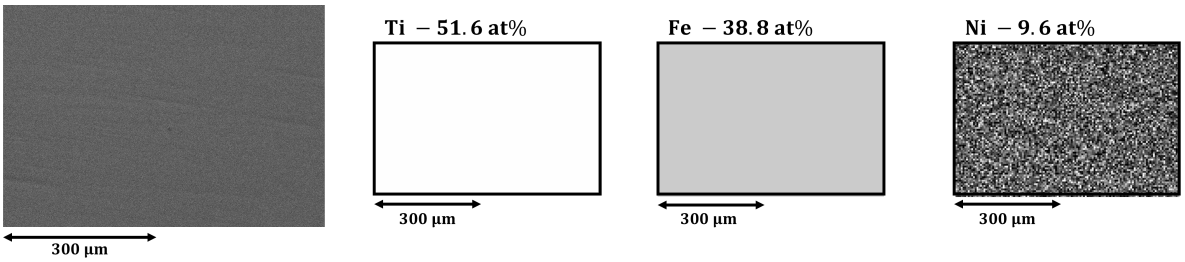

(d) **Ni20-a**

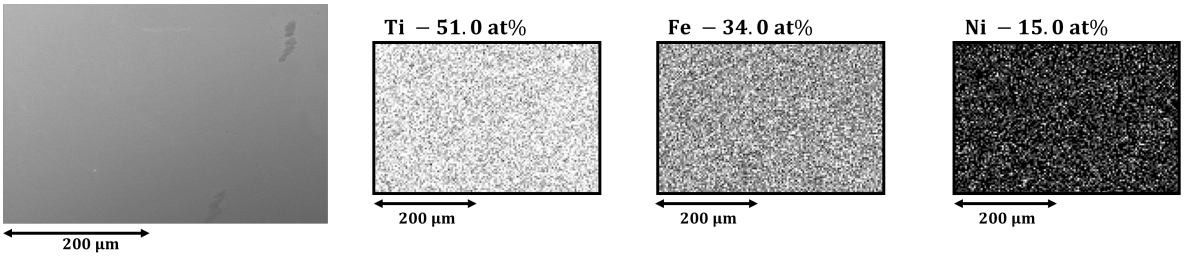

(e) **Ni30-a**

Figure 4.3: Morphological images (on the left) and relative EDX compositional maps of samples with different Ni content.

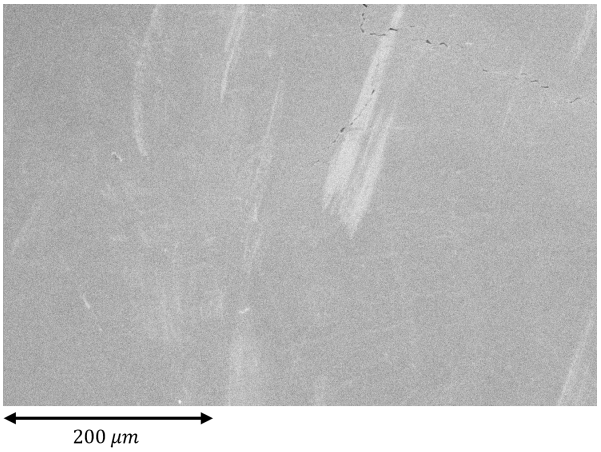

(a) **Ni05-b**

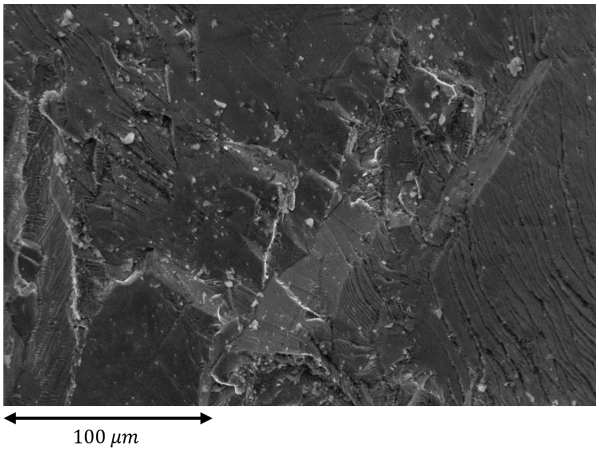

(b) **Ni10-b**

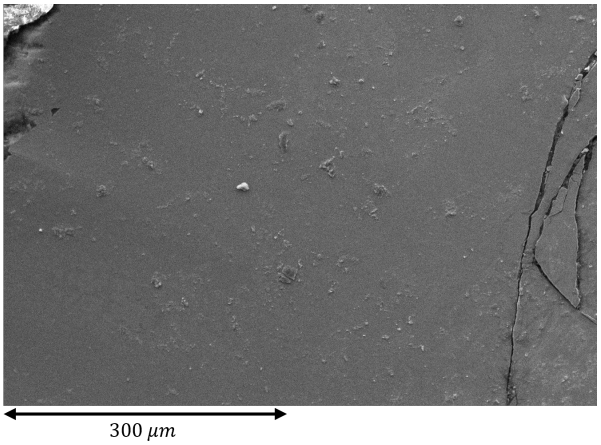

(c) **Ni15-b**

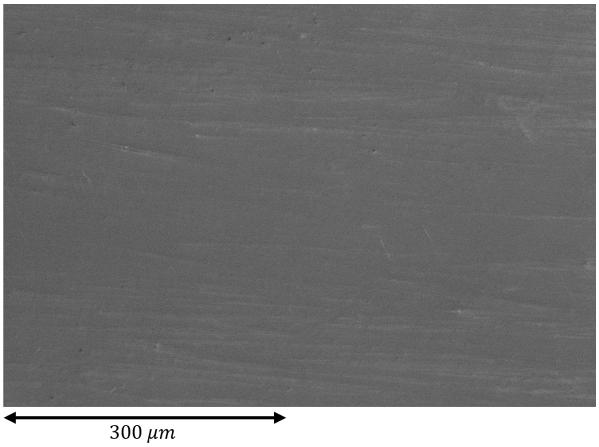

(d) **Ni20-b**

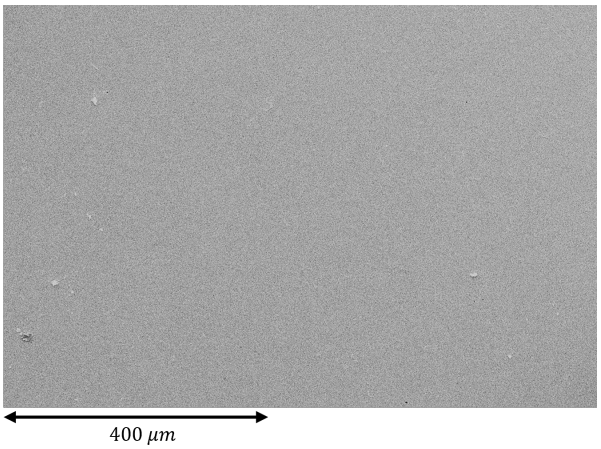

(e) **Ni30-b**

Figure 4.4: SE images of samples with different Ni content.

4.2 Structural characterization

XRD spectra of the BM samples are reported in Fig.4.6 and the results of Rietveld's refinement are in Tab.4.2. Since the peaks at 30°, 42.9°, 62.4°, 78.7°, 94.1°, 109.9° correspond to those of TiFe,[46] all samples have CsCl-type crystal structure, space group $Pm\bar{3}m$, represented in Fig.4.5. The superlattice peak at 30°, corresponding to the (100) plane, indicates an ordered structure resulting from the Arc Melting technique.

Table 4.2: *Results of Rietveld's refinement of XRD data.*
Samples, wt% of the identified phases, lattice parameter and crystallite size are indicated, with the associated error.

Sample	TiFe [wt%]	Ti_4Fe_2O [wt%]	Lattice parameter [$\dot{A}$]	Crystallite size [nm]
Ni05-b	99±0.1	1±0.1	2.981(3)	37.3±3.7
Ni10-b	98±0.2	2±0.2	2.982(3)	35.9±3.6
Ni15-b	95±0.5	5±0.5	2.985(3)	29.6±3.0
Ni20-b	95±0.5	5±0.5	2.987(3)	31.8±3.2
Ni30-b	99±0.1	1±0.1	2.993(3)	41.9±4.2

The peak at 41.6° is associated to the oxide phase Ti_4Fe_2O,[47] which is always found in concentrations between 1 and 5 wt%. Its formation can be facilitated by the sporadic presence of Ti-rich regions (also found via SEM analysis), due to high reactivity of Ti with oxygen and it could occur either during the alloying process or already be present in the raw material. Anyway, Ti_4Fe_2O has proved to be helpful in the activation process.[33] Thanks to the BM treatment, preferential orientation is not observed, at the price of the broadening of the peaks. The difference can be seen by comparing Fig.4.6 (d) and (e). On one side, this allows an easier analysis, since the application of Mach-Dollase algorithm is not required, while it needs to be used for 62.4° and 78.7° peaks of non-BM samples; on the other hand, the broader peaks cause a greater overlap between the 42.9° TiFe peak and the 41.6° oxide peak, resulting in a lower detected oxide phase concentration.

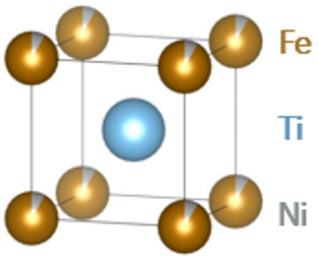

Figure 4.5: General crystal structure of $TiFe_{1-x}Ni_x$ compounds.

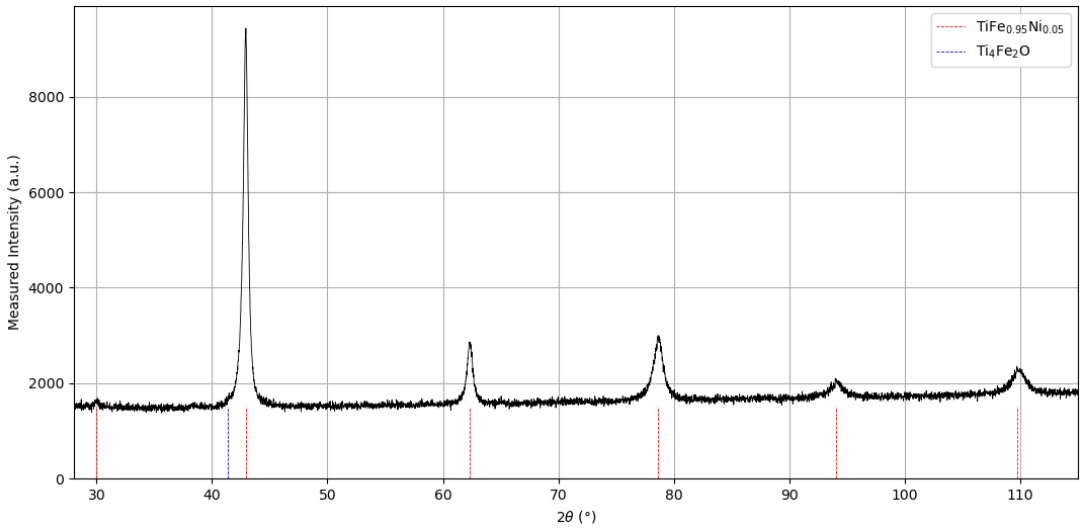

(a) **Ni05-b**

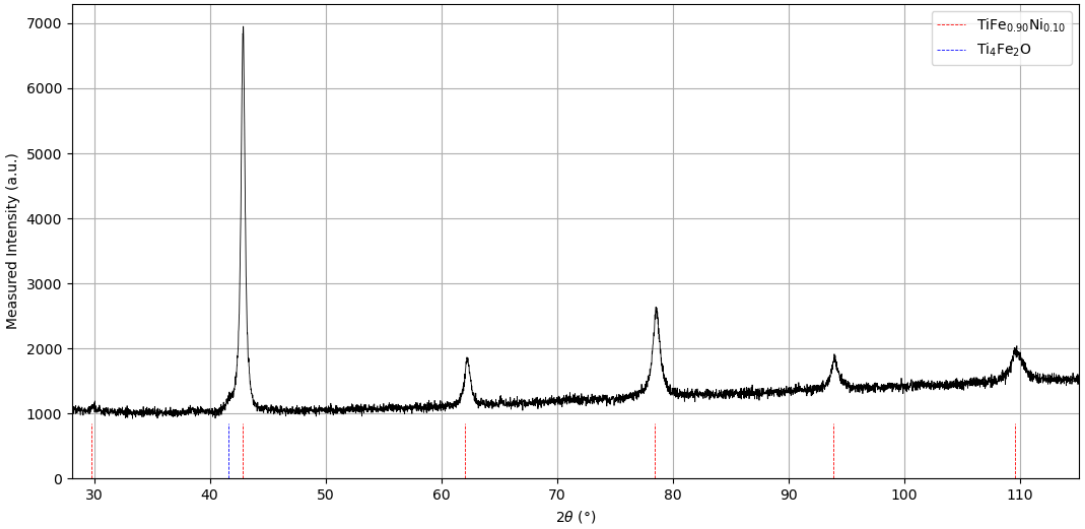

(b) **Ni10-b**

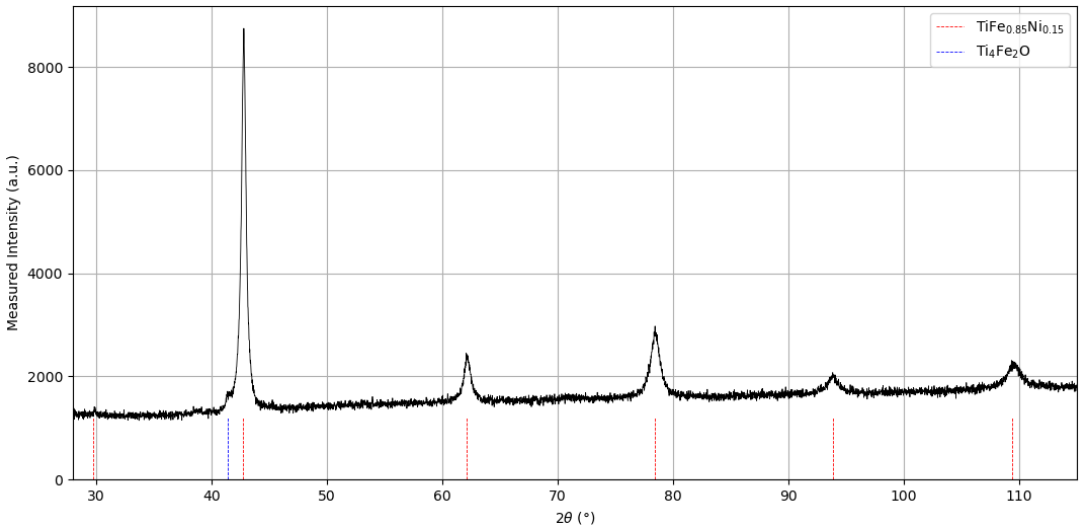

(c) **Ni15-b**

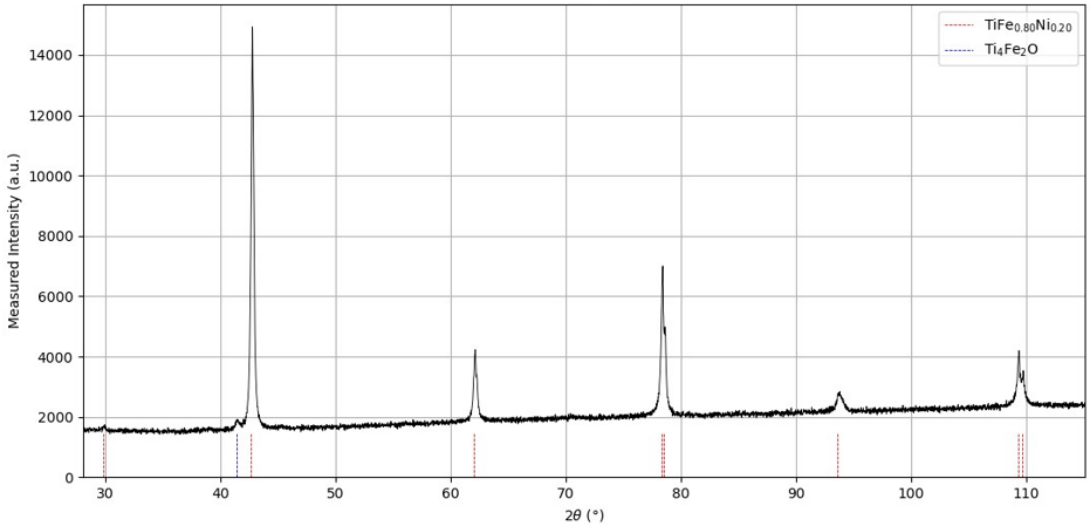

(d) **non-BM Ni20-b**

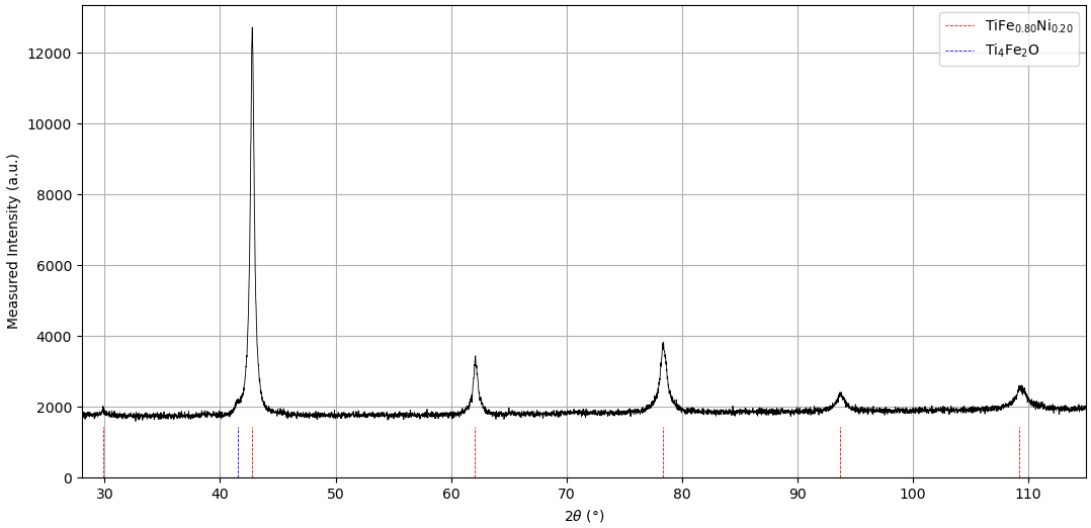

(e) **Ni20-b**

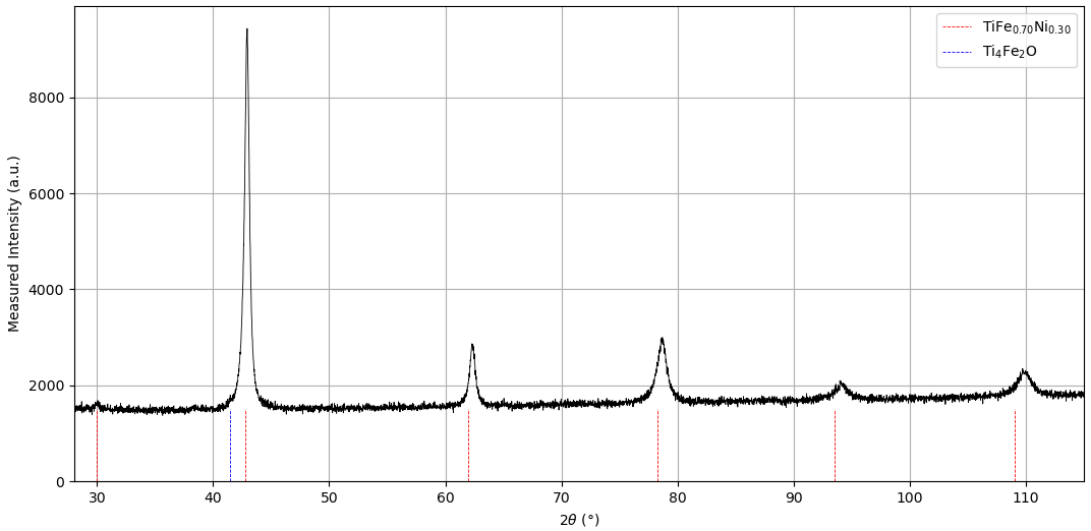

(f) **Ni30-b**

Figure 4.6: XRD patterns of samples (a) Ni05-b, (b) Ni10-b, (c) Ni15-b, (d) non-BM Ni20-b, (e) Ni20-a, (f) Ni30-a. Red dotted lines correspond to $TiFe_{1-x}Ni_x$ peaks, while blue ones are relative to Ti_4Fe_2O.

4.2.1 Vegard's law

The lattice parameter of Ni05-b is slightly larger than the TiFe one (2.976 $\dot{A}$), and it linearly increases with increasing Ni concentration (Tab.4.2). This is evident in the diffraction profiles of Fig.4.6 from the shift of characteristics TiFe peaks towards lower 2θ values, which correspond to larger lattice parameters, in agreement with Bragg's law (eq.3.1). These results demonstrate that partial substitution of Fe with Ni does not affect the structure, but only slightly increases the unit cell volume. Recalling that Vegard's law (eq.2.32) describes this effect, the correlation between Ni concentration x and the lattice parameter can be fitted with it, by considering that the reference binary compounds are TiFe and TiNi. Results of this analysis are in Tab.4.3 and show good agreement with the expected values. Considering samples in a wider x range would perhaps give a better outcome.

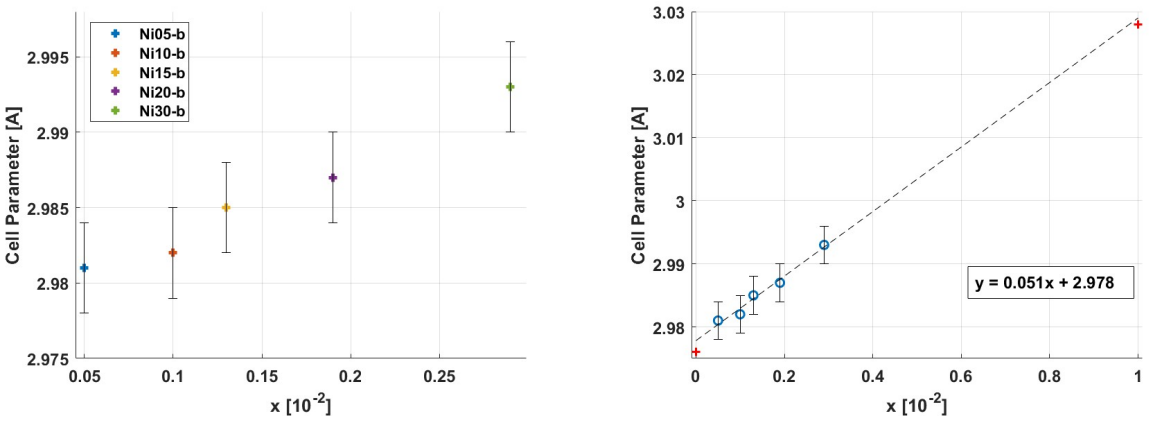

(a) (b)

Figure 4.7: Lattice parameter as a function of Ni atomic concentration: (a) shows data from samples analysis, (b) shows the fit (black dotted line) of data (blue circles) and lattice parameters of TiFe and TiNi from literature[2334] as a reference (red crosses).

Table 4.3: *Results of Vegard's law fit of the data.*
a^{exp} and a^{ref} are the experimental values from the fit and the reference values, respectively. Errors are given by the standard deviation.

Binary compound	a^{exp} [$\dot{A}$]	a^{ref} [$\dot{A}$]
TiFe	2.978(4)	2.976
TiNi	3.029(1)	3.015

4.3 Differential Scanning Calorimetry

4.3.1 Pd and $LaNi_5$ characterization

Before starting the calorimetric study of $TiFe_{1-x}Ni_x$, two well-known hydrides are characterized to verify the correct behavior of the instrument.
Pd is an easily activated and extensively studied hydride-forming metal, thus it can be used as a reference. Measures done with Pd sample (20.2 mg) can be seen in Fig.4.8 (a). The enthalpy of reaction is first evaluated from the peak area of heat flow as a function of temperature, but its value is approximately equal to half the expected one. This result is often not reliable, as anticipated in Section 3.3.1 and discussed later, due to pressure leaks and temperature rate instability. Then, a van't Hoff analysis is performed by taking equilibrium pressures and temperatures as a reference (Fig.4.8 (b)), obtaining results in agreement with expected ones (Tab.4.4).
$LaNi_5$ is not directly activated like Pd, so an activation procedure is needed. It consisted of alternated temperature ramps and isothermals at high pressure (40 bar), as reported in Fig.4.8 (c):

- isothermal (iso) @ 40°C, 3h + ramp to 60°C
- iso @ 60°C, 3h + ramp to 90°C
- iso @ 90°C, 3h + ramp to 180°C
- repeated heating-cooling ramps to verify complete activation

The sample was already activated after the first steps, confirming the well-known behavior of $LaNi_5$;[48] anyway, the procedure ensures that the activation is complete. Due to pressure leaks, the pressure decreases during the procedure, causing the temperatures reached with the second cooling ramp and the third heating one to be too low for H-sorption to occur, as proved by the absence of the corresponding peaks in Fig.4.8 (c). This was also verified with some additional measurements after the activation routine, which confirmed that the peak areas had stabilized around a constant value. Then, measurements were performed on the sample (11.8 mg) and are reported in Fig.4.8 (d); from the van't Hoff analysis (Fig.4.8 (e)) values near those reported in literature are obtained. The presence of the double desorption peak can be ascribed to the presence of the intermediate hydride phase β-$LaNi_5H_{3-4}$ between the α and the β ($LaNi_5H_6$) phases.[49] Final results relative to these two samples are in Tab.4.4 and, since they agree with literature, this type of analysis is also applied in the study of $TiFe_{1-x}N_x$ samples.

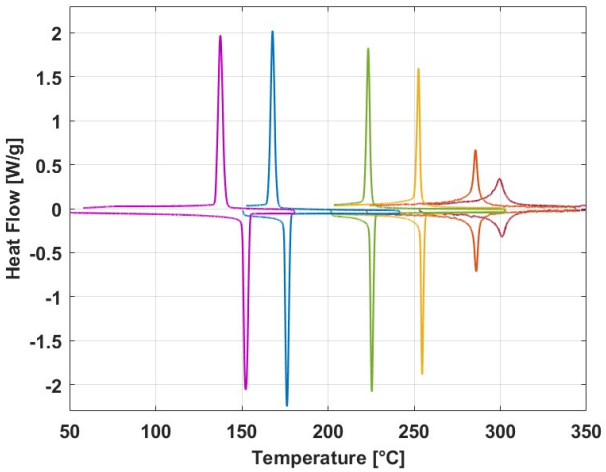

(a) Pd DSC ramps

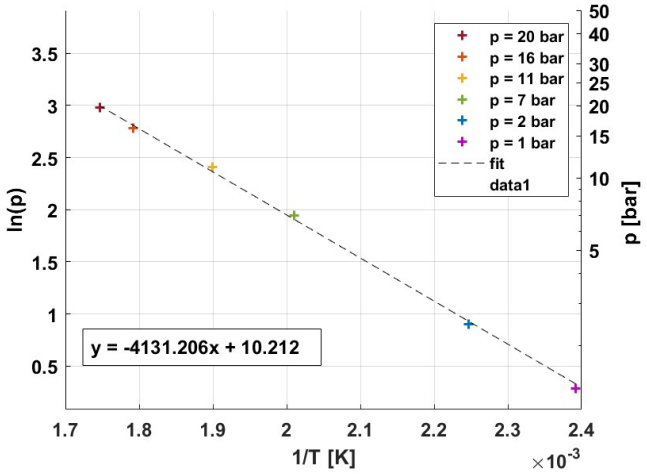

(b) Pd van't Hoff analysis

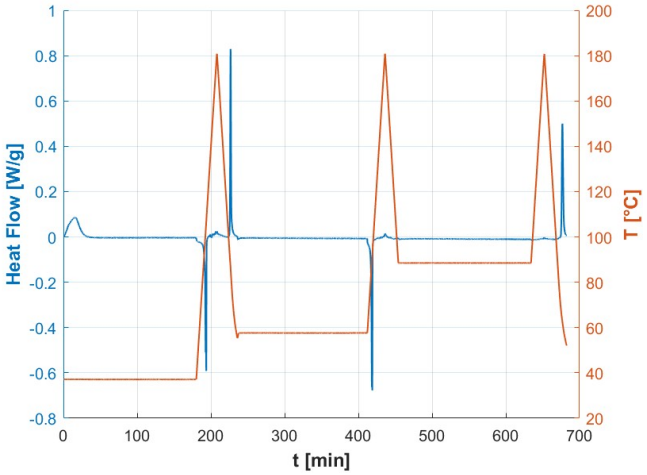

(c) $LaNi_5$ activation

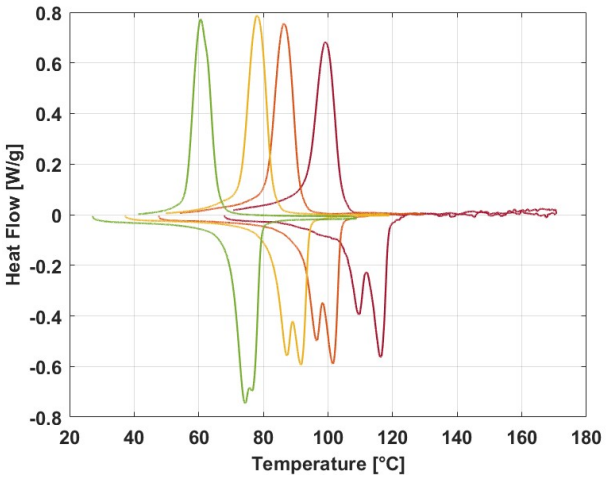

(d) $LaNi_5$ DSC ramps

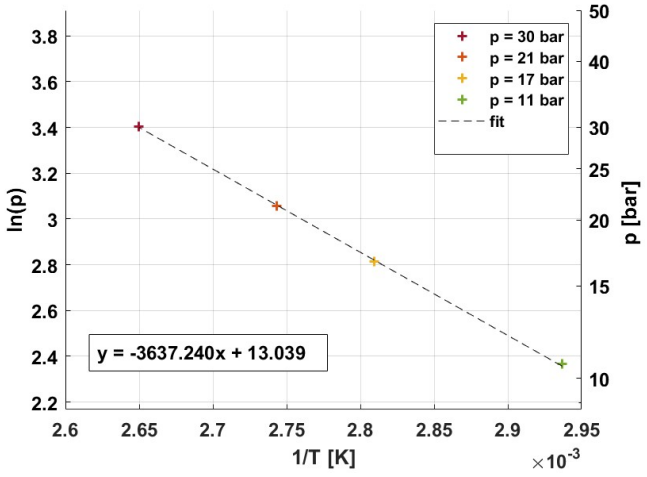

(e) $LaNi_5$ van't Hoff analysis

Figure 4.8: DSC data of (a) Pd measurements and (b) relative van't Hoff analysis, and those of $LaNi_5$ relative to (c) activation, (d) measurements and (e) van't Hoff analysis. Equilibrium p values of each DSC ramp of (a) and (d) are written on the van't Hoff plots (b) and (e)).

Table 4.4: *Results of van't Hoff analysis applied on Pd and $LaNi_5$ data.*
$\Delta H(S)^{exp}$ and $\Delta H(S)^{ref}$ are the experimental values from the fit and the reference values,[293132] respectively. The linear fits are weighted on the error on the pressure, given by its maximum semi-dispersion; errors on extracted values are given by the standard deviation.

Sample	$\lvert\Delta H^{exp}\rvert$ $[kJ\ mol^{-1}]$	$\lvert\Delta H^{ref}\rvert$ $[kJ\ mol^{-1}]$	$\lvert\Delta S^{exp}\rvert$ $[J\ mol^{-1}\ K^{-1}]$	$\lvert\Delta S^{ref}\rvert$ $[J\ mol^{-1}\ K^{-1}]$
Pd	37.0±0.7	$_{\alpha\to\beta}$ 37.4±0.3 $_{\beta\to\alpha}$ 39.0±0.5	84.9±1.3	$_{\alpha\to\beta}$ 92.5±0.8 $_{\beta\to\alpha}$ 92.5±1.3
$LaNi_5$	28.4±0.6	$_{\alpha\to\beta}$ 31.4 $_{\beta\to\alpha}$ 30.1	104.8±1.6	$_{\alpha\to\beta}$ 109.6 $_{\beta\to\alpha}$ 107.9

4.3.2 $TiFe_{1-x}Ni_x$ characterization

$TiFe_{1-x}Ni_x$ samples of mass of about 20 mg are weighted and inserted in the DSC (precise values are in Tab.4.5). Moreover, a previously synthesized $TiFe_{0.90}$ was analyzed to compare it with Ni-substituted samples. All samples need to be activated first, and

Table 4.5: *Samples analyzed with DSC.*
The error on the measures is given by the balance sensitivity, equal to 0.1 mg. Sample masses are re-measured after the experiment, and in the case of Ni20-b a mass loss is detected.

Sample	m [mg]
$TiFe_{0.90}$	20.5
Ni05-b	22.6
Ni10-b	20.2
Ni15-b	18.9
Ni20-b	21 ($\rightarrow$ 12)
Ni30-b	21.7

this is done by alternating repeated cooling-heating ramps at high pressure and high-T isotherms. The goal of this first step is to find the milder activation conditions possible, so for the first samples analyzed ($TiFe_{0.90}$ and Ni10-b), isotherms are performed at 40 bar at increasingly higher T starting from 50°C to 450°C, to verify the minimum necessary temperature:

- $TiFe_{0.90}$
  - iso @ 40°C, 4h + 20 heating-cooling ramps in the range [40-200]°C
  - iso @ 200°C, 10h + 30 heating-cooling ramps in the range [40-350]°C
  - **iso @ 450°C, 6h** + 3 heating-cooling ramps $\rightarrow$ partial activation
  - repeated heating-cooling ramps to verify complete activation

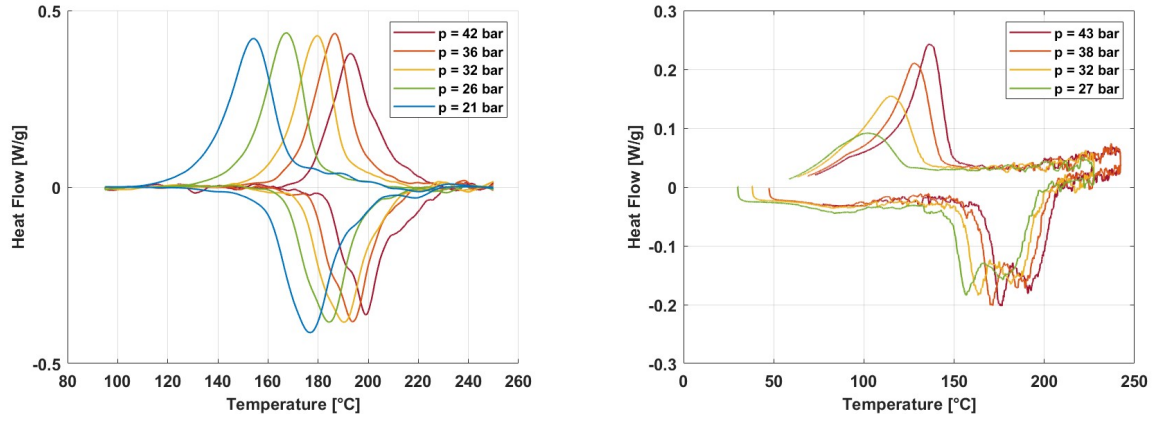

(a) (b)

Figure 4.9: DSC data (a) of Ni20-b after baseline removal and (b) of non-BM $TiFe_{0.90}Ni_{0.10}$.

- Ni10-b
  - iso @ 50°C, 2h + heating-cooling ramp [50-170-90]°C
  - iso @ 90°C, 2h + heating-cooling ramp [90-170-120]°C
  - iso @ 120°C, 2h + heating-cooling ramp [120-170-RT]°C
  - 4 heating-cooling ramps [90-200-90]°C
  - iso @ 130°C overnight, + heating-cooling ramp [90-200-90]°C
  - iso @ 200°C, 5h + heating-cooling ramp [200-80-300]°C
  - iso @ 300°C, 5h + 3 heating-cooling ramps in the range [300-80]°C
  - **iso @ 450°C, 5h** + heating-cooling ramps → partial activation
  - repeated heating-cooling ramps to verify complete activation

The crucial step to initiate partial activation in both procedures is the isothermal at 450°C, so the other samples are treated by performing about 10 cooling-heating ramps at high pressure and an isotherm directly at 450°C. Complete activation is achieved after a final series of repeated cooling-heating ramps, verifying that the heat flow signal area is constant. A more in-depth study on the activation procedure is necessary to better understand how to differently treat samples depending on their composition, in the most efficient and fast way.
Actual measurements are realized starting from high pressure (40 bar) and gradually lowering it towards lower values by steps of about 5 bar, as reported in Fig.4.10. The heat flow signal is normalized to the sample mass. Since all measurements show a non-zero baseline, an additional correction is added before analyzing them, following the method explained in section 3.3.1 and Appendix A1. As an example, Ni20-b data after baseline subtraction is plotted in Fig.4.9 (a), since its baseline is the most altered. This can be due to the presence of dispersed powder in the DSC cell that can jeopardize the heat flow detection, as a mass loss was detected in this case after the experiment.
The first noticeable tendency is that the peaks are shifted at lower temperatures as the

pressure is decreased, in agreement with van't Hoff equation (eq.2.13). In addition, with increasing Ni concentration (i.e. from (a) to (e)), peaks are at higher temperatures for a fixed pressure, showing that Ni-rich hydrides are more stable. Double peaks are observed in the desorption process of Ni10-b, Ni20-b and Ni30-b. They may be due to the separate di- and mono- hydride decomposition, or to a sluggish kinetics of the transition. Precise conclusions cannot be reached only based on DSC measurements, but Sievert's measurements can help identifying the causes of this behavior.
It is interesting to see the effect of ball-milling on the H-sorption reaction. Sample Ni10-b was first analyzed before BM, and the related data is represented in Fig.4.9 (b). The partial disappearance of double peaks from non-BM to BM Ni10-b show that the reaction occurs in a more direct step, as observed in literature.[23] This can be due to the better uniformity reached with BM in terms of powder particle size, since the resulting finer powder does not contain large grains that typically react more slowly.

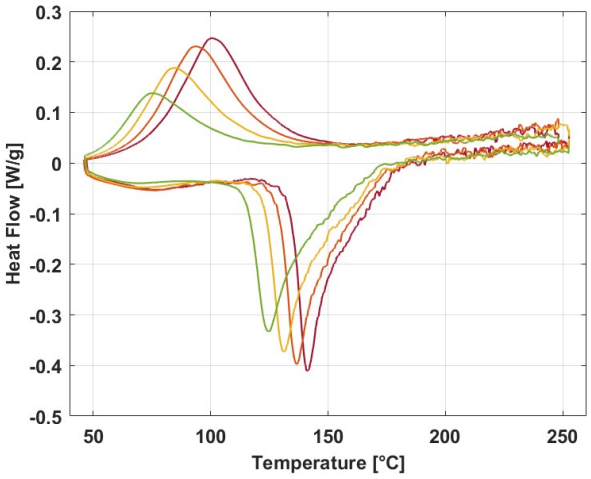

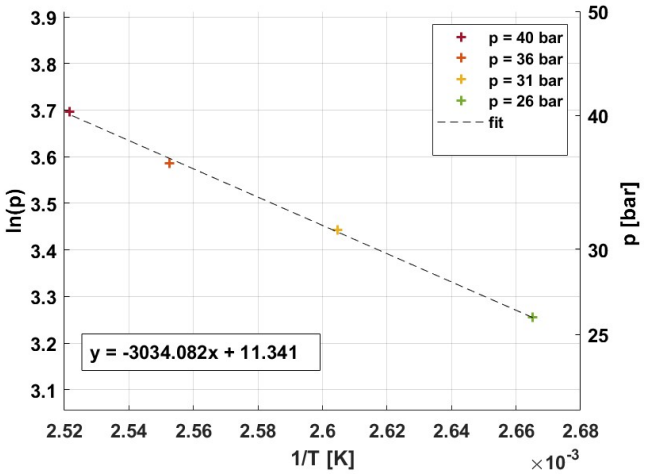

(a) **Ni05-b**

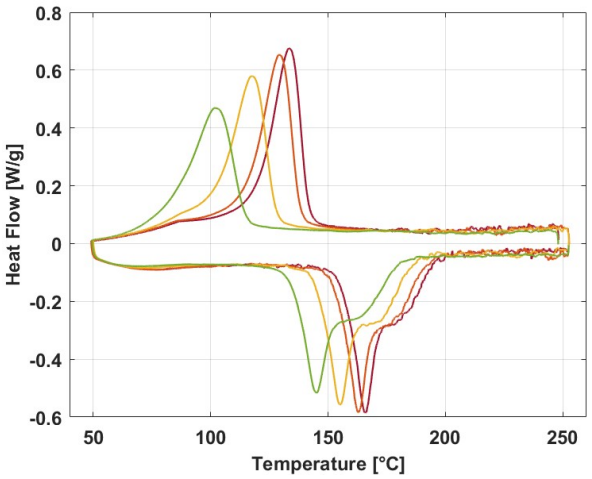

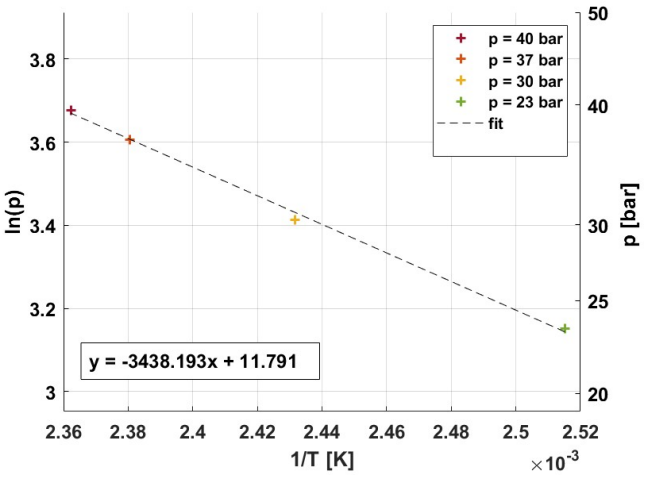

(c) **Ni10-b**

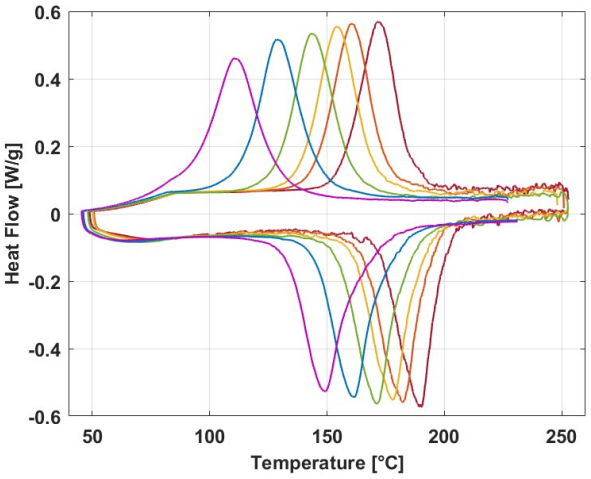

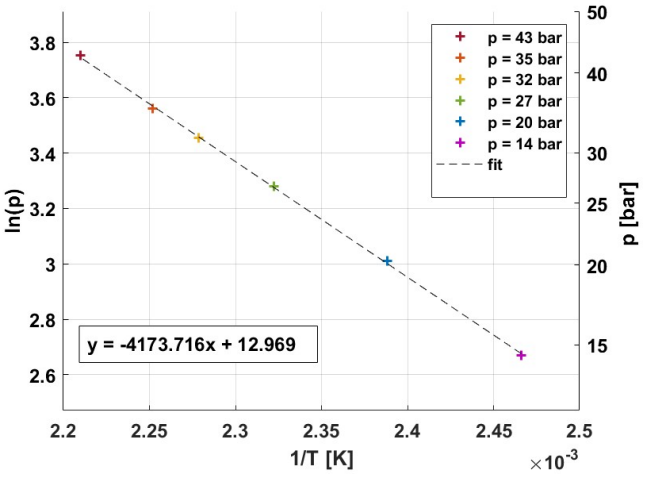

(e) **Ni15-b**

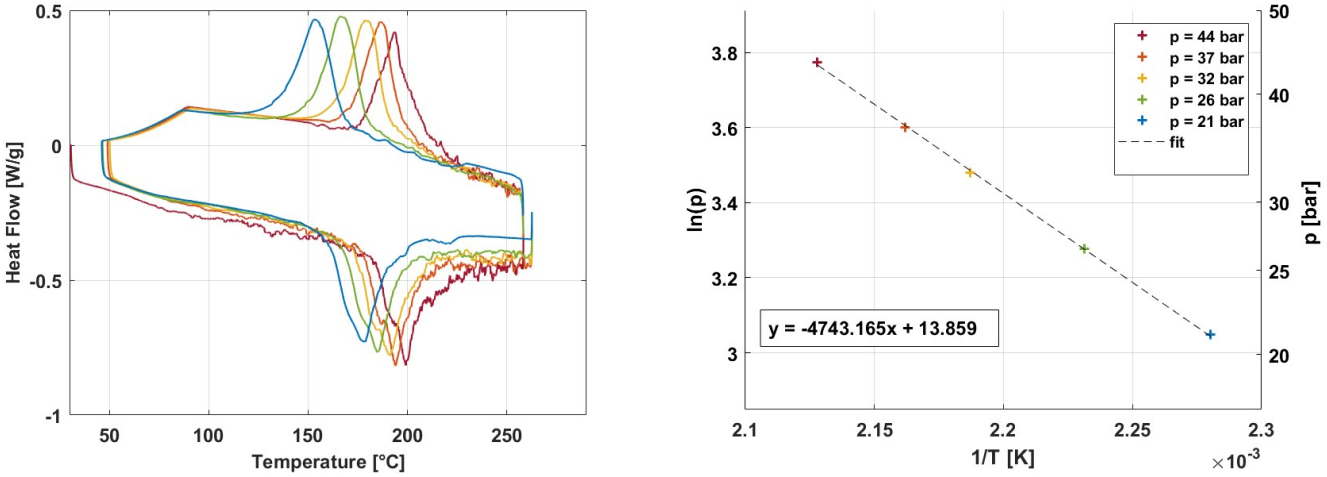

(g) **Ni20-b**

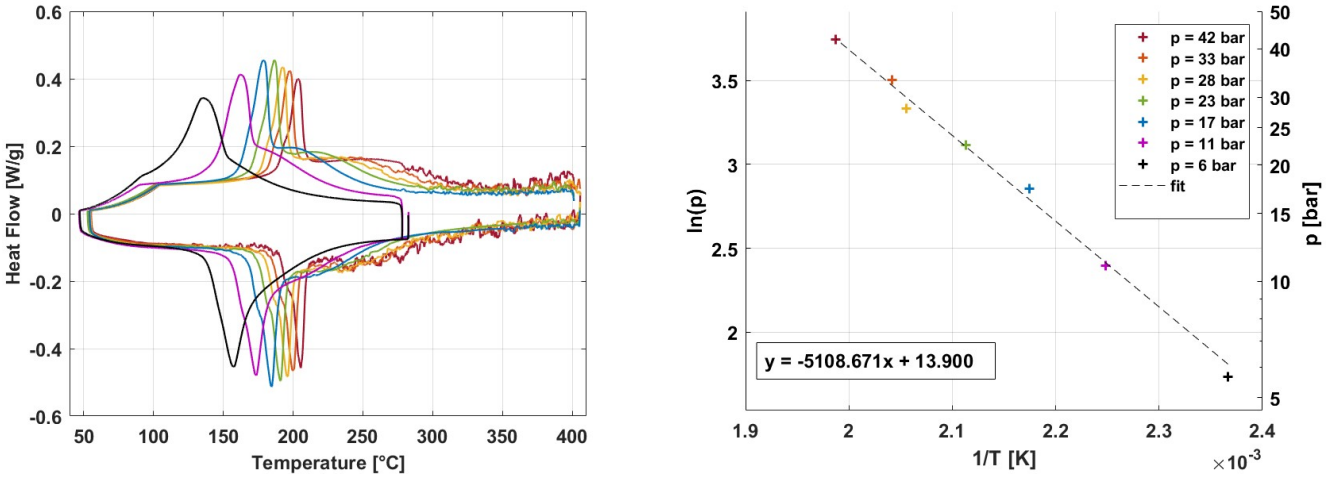

(i) **Ni30-b**

Figure 4.10: DSC raw data (on the left) and van't Hoff fits (on the right) of samples (a) Ni05-a, (b) Ni10-a, (c) Ni15-a, (d) Ni20-a, (e) Ni30-a. Colors from red to black correspond to decreasing pressure, starting from 40 bar (equilibrium p values of each measurement are written on the right-side plots).

Enthalpy of reaction from heat flow integration does not lead to meaningful results, as the extracted values are always lower than the expected ones and not constant throughout the set of measurements at different pressure for the same sample. This can be due to:

- **mass losses**
  In the case of Ni20-b a mass loss is detected (see Tab.4.5). Such event can occur during the purging process, where the DSC cell is repeatedly filled with Ar and emptied with the rotary pump, or when H_2 pressure is lowered between a measurement and the next, if the procedures are done too quickly causing powder suction. This makes data non-reliable.

- **temperature range limit**
  Heat flow signals of samples Ni05-b and Ni10-b at low pressure reach the limit of the temperature range where the DSC can work. In this region, the cooling rate is not maintained constant, since it is more difficult for the DSC to cool down the cell. This may affect data.

- **pressure leaks**
  Small pressure leaks are noticed during measurements, which may alter the result.

- **partial activation**
  A lower enthalpy than expected may indicate only part of the sample has been activated, due to the presence of regions whose interaction with hydrogen remains hindered. This can be verified with post-absorption XRD, provided that the sample does not release H upon exposure to air.

4.3.3 Van't Hoff analysis

In order to apply van't Hoff analysis, at least 4 measurements are needed. For samples with higher hydride formation/decomposition temperature, like Ni15-b, Ni20-b, and Ni30-b, it is possible to extend the range of pressure towards lower pressures, providing a richer dataset as a reference for the fit. Rongeat et al.[39] determined T_{eq} by taking the intersection between the background line and the slope of the peak. Anyway, this method is not trivial to apply in this case since the DSC ramps in Fig.4.10 do not show single and clear peaks, but rather multiple peaks with partial overlap, which are not easy to isolate and identify (see Appendix A1). Therefore, with the procedure explained in the Materials and Methods chapter, enthalpy and entropy of reaction are obtained by using van't Hoff equation to fit (p,T) values given by the average of absorption and desorption half-reaction parameters. The fit is weighted by the error on the pressure, given by its maximum semi-dispersion. Resulting van't Hoff plots are in Fig.4.10 and extracted values are listed in Tab.4.6. They show quite good agreement with values found in literature, which are determined for limited samples and only in few available studies. Differently from other samples, Ni30-b shows a broad peak at high temperatures and a sharper one at lower values. The latter has been studied separately from the rest and it leads to a very large enthalpy of reaction, equal to 60 kJ mol^{-1}. This behavior is unexpected for $TiFe_{1-x}Ni_x$ hydrides, and can be ascribed to the formation of TiNi secondary phases, which forms TiNi-H hydride with a heat of transition of about 60 kJ mol^{-1}.[50] We suppose it was not detected with XRD because TiNi has a Cs-Cl-like structure, like TiFe. Overall,

enthalpy of reaction increases for increasing Ni-concentration of the samples, as depicted in Fig.4.11, in agreement with previous studies[23].[51] DSC measurements for sample $TiFe_{0.90}$ are performed in a restricted temperature range at the limit of the available sampling interval and show very low signal. The van't Hoff analysis lead to $|\Delta H^{exp}| = (28.3 \pm 3.7)$ kJ mol^{-1}. Due to the experimental conditions, this value is not very reliable but shows that, in the absence of Ni, the hydride is less stable than Ni-rich ones. The $|\Delta H^{exp}|$ dependency on x determines the fact that, a fixed temperature, the equilibrium pressure for hydride formation/decomposition decreases for increasing Ni concentration, i.e. Ni stabilizes hydrides at lower pressures (Fig.4.12 (a)).

Table 4.6: *Results of van't Hoff analysis applied on* $TiFe_{1-x}Ni_x$ *data.*
$\Delta H(S)^{exp}$ are the experimental values from the fit, derived from the average of absorption and desorption parameters T, p. Errors are given by the standard deviation. $\Delta H(S)^{ref}$ are reference values from literature, for absorption ($\alpha \rightarrow \beta$) and desorption ($\beta \rightarrow \alpha$).[2352]

Sample	$\lvert\Delta H^{exp}\rvert$ $[kJ\ mol^{-1}]$	$\lvert\Delta H^{ref}\rvert$ $[kJ\ mol^{-1}]$	$\lvert\Delta S^{exp}\rvert$ $[J\ mol^{-1}\ K^{-1}]$	$\lvert\Delta S^{ref}\rvert$ $[J\ mol^{-1}\ K^{-1}]$
Ni05-b	25.2±0.8	-	94.3±2.1	-
Ni10-b	28.6±1.0	$_{\alpha \rightarrow \beta}$ 31.4±3.3 $_{\beta \rightarrow \alpha}$ 34.7±3.3	98.0±2.5	$_{\alpha \rightarrow \beta}$ 106.3±5.9 $_{\beta \rightarrow \alpha}$ 112.1±5.9
Ni15-b	34.7±0.4	$_{\alpha \rightarrow \beta}$ 32.2±5.8 $_{\beta \rightarrow \alpha}$ 37.7±5.8	107.8±0.9	$_{\alpha \rightarrow \beta}$ 102.9±15.1 $_{\beta \rightarrow \alpha}$ 117.6±15.1
Ni20-b	39.4±0.5	$_{\alpha \rightarrow \beta}$ 39.3±2.2 $_{\beta \rightarrow \alpha}$ 41.9±2.2	115.2±1.1	$_{\alpha \rightarrow \beta}$ 113.4±5.0 $_{\beta \rightarrow \alpha}$ 118.4±5.0
Ni30-b	42.5±1.8	-	115.6±3.7	-

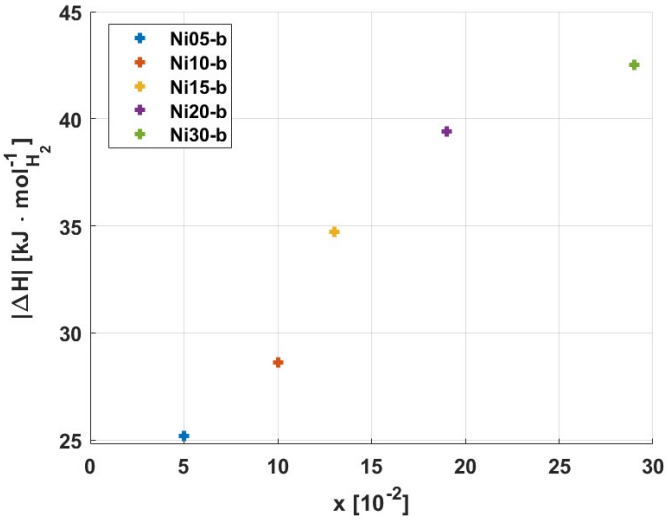

Figure 4.11: Enthalpy of reaction as a function of Ni atomic fraction.

4.3.4 Enthalpy-Entropy Compensation

Van't Hoff analysis of DSC data clearly shows a linear increase of $|\Delta H^{exp}|$ as a function of $|\Delta S^{exp}|$ (Tab.4.6), depicted in Fig.4.12, following the equation:

$$\Delta H \;=\; a\Delta S + bR \tag{4.1}$$

This effect is known as Enthalpy-Entropy Compensation (EEC) and is observed in many

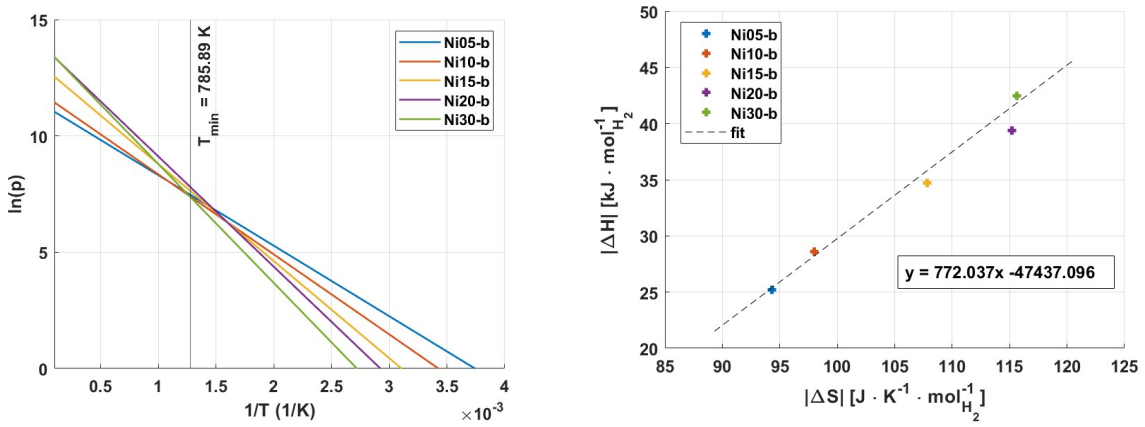

(a) (b)

Figure 4.12: (a) van't Hoff fits of the $TiFe_{1-x}Ni{-}x$ samples with coalescence point T_{min} and (b) extracted enthalpy of reaction values as a function of entropies of reaction showing EEC.

chemical and biological reactions. However, it can be a statistical artifact when measurements are performed in a small region of the p-T plane, forcing van't Hoff plots to encounter in an intersection point and resulting in a linear correlation between $|\Delta H^{exp}|$ and $|\Delta S^{exp}|$. The main parameter describing this effect is the compensation temperature, where all the samples have the same equilibrium pressure. It is given by the slope of $|\Delta H^{exp}|$ - $|\Delta S^{exp}|$ linear fit (eq.4.1):

$$a \;=\; T_{comp} \;=\; \frac{d(\Delta H)}{d(\Delta S)} \tag{4.2}$$

In the ideal case, where van't Hoff plots meet at a single point, this point is T_{comp} and it corresponds to the isoequilibrium condition. In general, measurements are affected by experimental errors, thus one can only consider T_{comp} as a trustworthy compensation temperature indicating the coalescence region of van't Hoff plots. Griessen et al.[5354] investigated this phenomenon and defined a method to understand if EEC is genuine or the result of artifacts. Following their work, a second parameter is defined as the temperature at which the variance σ^2 of $ln(p)$ is minimum. We have that:

$$\sigma^2\left(ln\left(p(T)\right)\right) \;=\; \frac{1}{N-1}\sum_{i=1}^{N}\left[ln\left(p_i(T)\right) - \langle ln\left(p(T)\right)\rangle\right]^2 \tag{4.3}$$

where samples are labeled by $i = 0, 1, ...N$ and average values are given by $\langle x \rangle = \frac{1}{N}\sum_i^N x_i$. Using van't Hoff equation, this formula can be rewritten as a function of thermodynamic variables as follows:

$$\sigma^2\left(ln\left(p(T)\right)\right) = \frac{1}{N-1}\sum_{i=1}^{N}\left[\left(H_i - \langle H\rangle\right)\frac{1}{RT} - \left(S_i - \langle S\rangle\right)\frac{1}{R}\right]^2 \tag{4.4}$$

To find the minimum of this function, we impose:

$$\frac{d}{d(1/T)}\sigma^2\left(ln\left(p(T)\right)\right) = 0 \tag{4.5}$$

The correspondent temperature T_{min} can now be expressed in terms of the variance $\sigma^2(h)$ and the covariance $\sigma^2_{h,s}(h,s)$, with $h = \Delta H/R$ and $s = \Delta S/R$:

$$T_{min} = \frac{(N-1)\,\sigma^2(h)}{N\sigma^2_{h,s}(h,s)} \tag{4.6}$$

Since from the linear fit with eq.4.1, by applying the least square method, one gets:

$$\begin{cases} T_{comp} = \frac{N\sigma^2_{h,s}(h,s)}{(N-1)\sigma^2(s)} \\ R^2 = \frac{N^2\left[\sigma^2_{h,s}(h,s)\right]^2}{(N-1)^2\sigma^2(h)\sigma^2(s)} \end{cases} \tag{4.7}$$

one can finally write:

$$T_{min} = \frac{T_{comp}}{R^2} \tag{4.8}$$

where R^2 is obtained by the linear fit in Fig.4.12 (b). If $R^2 = 1$, then we are in the ideal condition of $T_{min} = T_{comp}$. In the case of DSC data in Fig.4.10 (a), one finds $T_{min} \sim 786$ K. The variance of $ln(P)$ at $T = T_{min}$, defined as σ^2_{min}, is a direct measure of the degree of coalescence of the van't Hoff plots, together with its maximum value σ^2_{max}, through the Compensation Quality Factor:

$$CQF = 1 - \sqrt{\frac{\sigma^2_{min}}{\sigma^2_{max}}} = 1 - \sqrt{\frac{1-R^2}{\left(\frac{1}{R^2}\right)\left(\frac{T_{comp}}{T^*}\right)^2 - 2\left(\frac{T_{comp}}{T^*}\right) + 1}} \tag{4.9}$$

T^* is the temperature at which $\sigma^2 = \sigma^2_{max}$. If the experiments have been realized in the temperature range $[T_1;T_2]$, we intuitively have that $T^* = T_1$ if T_{min} is closer to T_2, and vice versa.
Since the first H-sorption process is observed at ∼100°C (for Ni05-b), this can be considered as a reference for T_1, and because data in Fig.4.12 (a) follow the first behavior, CQF can eventually be computed considering that: $T_{comp} \sim 772$ K and $R^2 = 0.984$ (from the linear fit of values in Fig.4.12 (b)), and $T^* = 323$ K. In the end: CQF = 0.89.
Boundary conditions to understand if the EEC is genuine are represented by the $\gamma[N,\text{CL}\%]$, defined for N samples and the confidence level CL%: if CQF>γ, EEC is a real effect. This reference function has been found by Griessen et al.[53] by considering statistically independent randomly generated van't Hoff lines for a set of N samples and for a chosen

CL%. For example, for a CL%=99% and a set of N=10 samples, they found that 99% of all CQF values from the random simulations are below 0.67 or, equivalently, that there is only a 1% probability that the EEC of an experimental data set for N=10 samples with CQF>0.67 is of a statistical nature. Thus the threshold is set to γ=0.67. Repeating this procedure for different set [N,CL%] parameters, they identified the following functions (plotted in Fig.4.13):

$$\begin{cases} \gamma[N; 95\%] &= 0.29 + 1.43/N^{0.67} \\ \gamma[N; 99\%] &= 0.29 + 1.41/N^{0.57} \\ \gamma[N; 99.5\%] &= 0.29 + 1.39/N^{0.53} \end{cases} \tag{4.10}$$

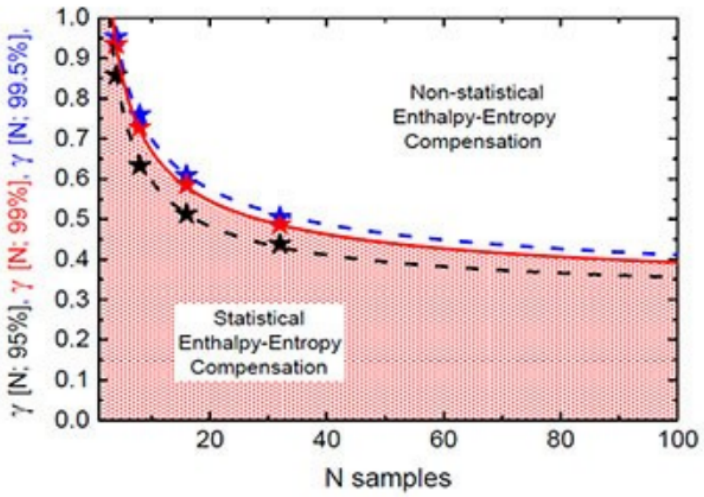

Figure 4.13: γ parameter indicating the boundary condition for different confidence levels depending on the number of samples studied.[53]

For N≥5, the boundary condition $\gamma[N = 5; 99\%]$ is strict enough to determine EEC source. Thus, choosing CL% = 99%,

$$\gamma[N = 5; 99\%] = 0.85 < CQF = 0.89 \tag{4.11}$$

This result indicates that there is 99% probability that EEC is of non-statistical, thus physical, reason, and we can conclude that our data show a genuine EEC effect.
The trade-off between enthalpic and entropic terms can be briefly explained by looking at the free energy expression: $\Delta G = \Delta H - T\Delta S$. Indeed, because of the opposite sign, the two contributions will tend to compensate each other: as H becomes more negative forming a more stable system, S tends to decrease, while as H becomes less negative, S tends to increase as the system becomes increasingly disordered.[55] From a physical point of view, understanding the profound causes to this effect in the case of hydrides is not trivial. Since in this work correlations between composition, unit cell volume, enthalpy and entropy were found, these are the starting points. The correlation between structure and stability demonstrated here, has also been found in previous studies. For example, Cuevas et al.[57] determined a linear relation between the intermetallic cell volume

v_{cell} and the logarithm of the plateau pressure in $LaNi_5$ alloys, proving that an increase in v_{cell} stabilizes the hydride at lower plateau pressures. Lundin et al.[58] determined a similar correlation taking as a reference the interstitial volume for AB_5 and AB compounds. We thus highlight the importance of structural features in the determination of thermodynamic properties. The enthalpy variation determines the stability of the final state: the large $|\Delta H|$ variation found in this study (Tab.4.6) tells that, upon absorption, the hydride state is more stable than the initial metal state. The fact that increasing (negative) enthalpy of formation is accompanied by increased (negative) entropy can be explained considering structural factors as follows. The entropy of formation is given by $\Delta S^{abs} = S_{M-H} - (S_M + S_{H_2}) < 0$, where the terms indicate the entropy of the hydride, metal and gaseous state, respectively. Entropy accounts for different contributions: vibrational and configurational. Since the entropy of H_2 has the typical value of 130 J mol^{-1} K^{-1}, we need to focus on the hydride and on the metal states. A first explanation for absorption entropy decrease upon Ni-content increase is that the entropy in the hydride state is lower. When the hydride is formed, the contribution of H atoms must be taken into account. Consider hydrogen atoms in interstitial sites between metal atoms. On one side, owing to its low mass, a hydrogen atom vibrates as if in a cage. Although the neighboring metal atoms must move a bit in response to the moving hydrogen atom, these metal atom displacements are small. If the interatomic forces between the metal and hydrogen atoms are moderate, the system will show a "local mode" at a high frequency, typically above the modes of the metal crystal.[56] Since the unit cell volume increases with Ni-substitution, and so do interstitial sites, we can suppose that H can move in a larger space, thus increasing the vibrational entropy with increasing Ni content. On the other side, configurational entropy must be taken into account. The decrease of ΔS with Ni concentration shows a loss in the configurational term. This has proven to happen if the H concentration in the hydride increases[18] (eq.2.11), and since $TiFe_{1-x}Ni_x$ hydrides capacity seems to have higher capacity with increasing Ni content,[59] this might a primary source of lower configurational entropy. Moreover, effects of lattice distortion could cause an additional decrease in the entropy of the hydride state.[60] This could be important in this case since TiFe changes crystal structure from cubic to orthorombic upon hydrogenation[23] and a similar behavior is expected from Ni-substituted alloys. Post-absorption XRD would be useful to asses the occurrence of a structural transformation also in these compounds.

A second motivation for the decreasing absorption entropy of transformation is linked to the characteristics of the metal. Considering the metal in state M, the interaction between the A and B components in the A-B complex can be approximately described by a potential energy function of the usual Lennard-Jones kind (Fig.4.14). For a deep well, corresponding to a strong bond, the vibrational energy levels of the system are widely spaced and the vibrational entropy is small; on the other hand, a shallow well corresponds to many closely-spaced vibrational levels and hence to a larger vibrational entropy.[55]

Because Ti-Ni bond is weaker than the TiFe one, we can conclude that with increasing Ni concentration, the vibrational entropy of the intermetallic alloy can increase, since there are more available states to explore for the atoms. Another way of seeing this is by attributing springs to the bonds in the lattice: stronger bonds correspond to stiffer springs, and an increased order in the crystal.[56]

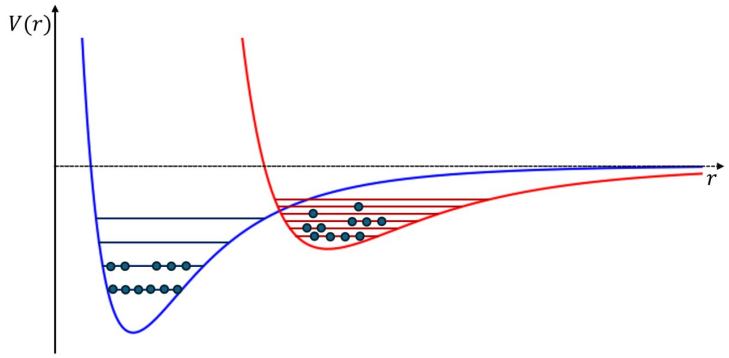

Figure 4.14: Interatomic potential and available energy levels.

In the end, the cumulative effect of these entropic contributions in the hydride and in the metal states can lead to the observed correlation among composition, structure and thermodynamics. This shows how structural features can be determinant for thermodynamic properties of hydride systems. In particular, in our study they allow to give an explanation of how stoichiometric tailoring leads to minimal structural modification in the intermetallic alloy, which can in turn change its hydride-forming thermodynamics.

4.3.5 Hysteresis

Additional information from the DSC ramps concerns hysteresis. This effect is always observed between hydride formation and decomposition and, in the case of isobaric measurements, it is represented by the difference between the equilibrium temperature for absorption and that for desorption. From Fig.4.15 (a), it is evident that such hysteresis increases with decreasing set pressure, as also demonstrated by the ramps in Fig.4.10. This suggests that absorption and desorption occur in slightly different conditions, supposedly because of coherent energy strains due to the hydride formation,[24] as explained in Section 2.2.1. Also Ni seems to influence this effect, decreasing it from Ni05-b to Ni30-b. Nonetheless, Fig.4.15 (b) proves that this effect strictly depends on the temperature, since hysteresis linearly decreases with increasing average temperature. Clear attribution of the source of hysteresis is not possible based on DSC measurements, but can be understood via equilibrium measurements, like PCIs. As to pressure changes (4.15 (c)), hysteresis is a mere consequence of the ideal gas law (eq.3.6) and pressure leaks, which are intuitively more important at higher set pressures.

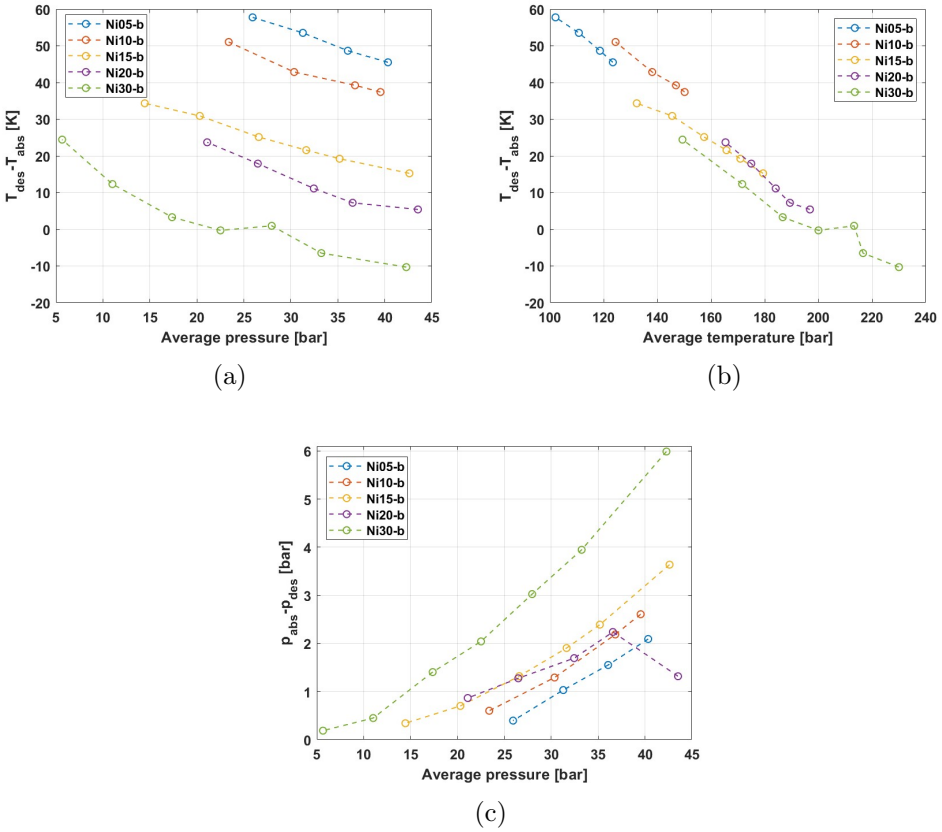

(a) (b)

(c)

Figure 4.15: Absorption-desorption hysteresis in DSC measurements: temperature hysteresis Vs average pressure (a) and average temperature (b), and pressure hysteresis Vs average pressure (c).

4.4 Sievert's Measurements

4.4.1 Instrument calibration

Volumes resulting from the measurement procedure exposed in section 3.3.2 can be found in Tab. 4.7. Due to some modifications done to the apparatus before the start of measurements, V_c has been measured again by filling $V_{cx} - V_c$ with H_2 gas and later opening MV1. Final values are the average of repeated measurements and the uncertainty is given by the standard deviation, which depends on the pressure error and temperature fluctuations.

Table 4.7: *Internal volumes of the Sievert's apparatus.*

Portion	Volume [cm^3]
V_c	51.92 ± 0.98
V_{cx}	64.81 ± 0.26
V_{cxt}	70.74 ± 0.37
V_{TOT}	76.64 ± 0.49
V_{sh}	5.89 ± 0.05

The main source of error on the measurements is the pressure gauge accuracy. Since it can be at most equal to 1% on the reading, it is possible to estimate the minimum detectable absorbed/desorbed hydrogen mass. Setting a pressure of 0.1 bar in the system, a 1% change in the pressure corresponds to a minimum detected mass change of 80 μg for a 1 g sample, and grows up to 6 mg for a set pressure of 50 bar. Accuracy of the measurement is determined by applying eq.3.16 to eq.3.13, with errors on p and T, reported in section 3.3.2, on V, from the previous table, and on m_s ($\delta m = 0.1$ mg). Considering experimental conditions, in a pressure range from 0.1 to 50 bar, with system and sample holder temperatures equal to 30°C and 100°C, respectively, and with a sample of 1 g, the hydrogen capacity uncertainty is of 0.08 wt%. Knowing this allows to verify than a correction with van der Waals equation (eq.3.15) would not be appreciable, since it is on the order of 10^{-3} wt%.

4.4.2 $TiFe_{1-x}Ni_x$ characterization

$TiFe_{0.90}Ni_{0.10}$

A 0.501 g sample of non-BM Ni10-b was characterized with the Sievert's apparatus in a previous research work by E. Pericoli.[45] To reach activation, similarly to the procedure applied for DSC, the sample is treated at high temperatures and high pressures, which are additionally alternated to vacuum cycles. Applying high pressures p' at a fixed temperature T' such that $p' > p_{eq}^{abs}(@T')$, has the aim of inducing H_2 absorption by the sample. After these treatments, kinetic measurements are performed: pressure is reduced at $p' < p_{eq}^{des}(@T')$ to allow desorption, and increased again for absorption, in subsequent cycles, to ensure complete activation. Then, PCI measurements are performed at 100 80, 60 and 40°C. Following the method described in Section 3.3.2, and applying eq. 3.13,

the pressure dependence on the hydrogen capacity is obtained. The van't Hoff analysis is performed by considering the average plateau pressure as the equilibrium pressure for the process at a fixed temperature. Data and van't Hoff analysis are in Fig.4.16, and results of the latter are in Tab.4.8.

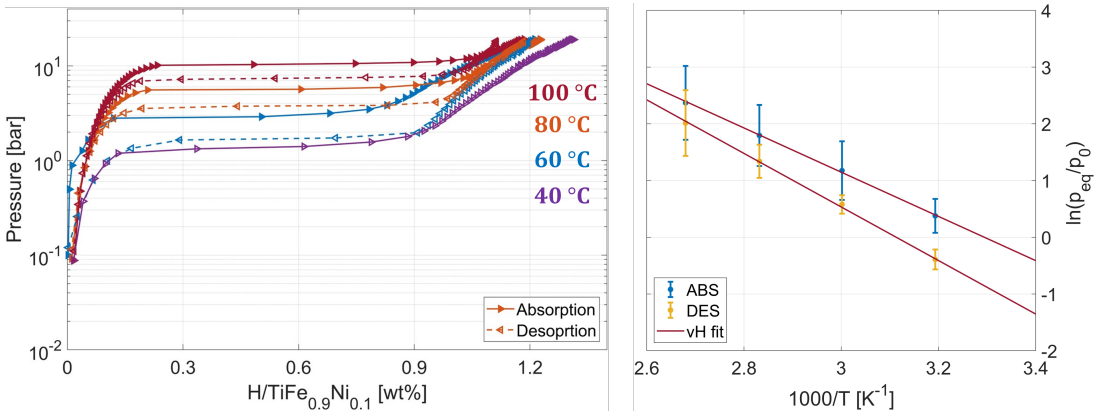

Figure 4.16: PCI measurements and van't Hoff analysis performed on sample non-BM Ni10-a. Absorption and desorption pressures are estimated as the mean value on the relative plateau region, and uncertainties are the maximum error of the chosen range.

$TiFe_{0.80}Ni_{0.20}$

A 1.064 g sample of non-ball milled $TiFe_{0.80}Ni_{0.20}$, namely Ni20-d, is characterized with Sievert's apparatus. After complete activation is achieved, a PCI absorption measurement is performed at T = 100°C, in the pressure range from 0.1 to 10 bar. Following the aforementioned procedure, the final relation between the sample pressure and the hydrogen capacity is plotted in Fig.4.17. The total achieved wt% is of 1.15±0.02 and the equilibrium pressure is 2 bar, which is in agreement the value available in literature, of about 2.4 bar.[23] Moreover, this pressure is lower than the absorption plateau pressure of Ni10-a at 100°C, at 10 bar, proving again hydride stabilization with increasing Ni content.

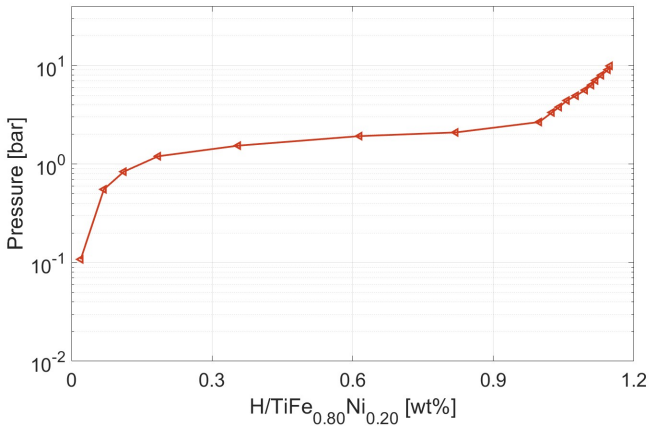

Figure 4.17: Absorption PCI of sample Ni20-d at 100°C.

Comparison with calorimetric analysis

Results from DSC are confirmed by the van't Hoff analysis of non-BM Ni10-b PCI measurements. They are summarized in Tab.4.8, and compared with reference values. Considering compound $TiFe_{0.80}Ni_{0.20}$, the expected equilibrium pressure for H-sorption for Ni20-b was 3 bar, which is only slightly higher than the value extracted from the absorption PCI of Ni20-d. This is a supplementary indication that the DSC allows to evaluate thermodynamic properties of hydrides with about 10% precision, while requiring much shorter measurement time. This is useful to efficiently study the behavior of a set of numerous samples in a range of compositions and to determine eventual tendencies among them, which is not possible with the longer procedure of PCI measurements.

Table 4.8: *Results of van't Hoff analysis applied on $TiFe_{0.90}Ni_{0.10}$ data.*
$\Delta H(S)^{exp}$ are the experimental values from the fit applied to DSC and PCI data. Errors are given by the standard deviation. $\Delta H(S)^{ref}$ are reference values from literature, for absorption ($\alpha \rightarrow \beta$) and desorption ($\beta \rightarrow \alpha$).[23]

$\lvert\Delta H^{exp}_{DSC}\rvert$ $[kJ\ mol^{-1}]$	$\lvert\Delta H^{exp}_{PCI}\rvert$ $[kJ\ mol^{-1}]$	$\lvert\Delta H^{ref}\rvert$ $[kJ\ mol^{-1}]$	$\lvert\Delta S^{exp}_{DSC}\rvert$ $[J\ mol^{-1}\ K^{-1}]$	$\lvert\Delta S^{exp}_{PCI}\rvert$ $[J\ mol^{-1}\ K^{-1}]$	$\lvert\Delta S^{ref}\rvert$ $[J\ mol^{-1}\ K^{-1}]$
28.6±1.0	$_{\alpha\rightarrow\beta}$ 32.4±0.7 $_{\beta\rightarrow\alpha}$ 39.2±0.8	$_{\alpha\rightarrow\beta}$ 31.4±3.3 $_{\beta\rightarrow\alpha}$ 34.7±3.3	98.0±2.5	$_{\alpha\rightarrow\beta}$ 107±2 $_{\beta\rightarrow\alpha}$ 122±3	$_{\alpha\rightarrow\beta}$ 106.3±5.9 $_{\beta\rightarrow\alpha}$ 112.1±5.9

Chapter 5

Conclusions and Outlook

The present research aims to analyze the properties and to delve into the physics of $TiFe_{1-x}Ni_x$ intermetallic hydrides. Samples were synthesized in a wide range of compositions, going from $x = 0.05$ to 0.30, by arc melting. In the first part of the study, SEM was used to examine composition and morphology, with EDX and SE, respectively, after lapping and polishing of the samples. All samples show compositional and morphological homogeneity overall; in the case of visible surface defects, no correlation with composition alteration is verified, thus such features only depend on the metallurgical treatment. Ball-milled samples crystalline structure is analyzed with XRD. This experiment shows that the crystalline structure of TiFe is not modified due to partial Ni-substitution, but only the unit cell volume is slightly increased. Indeed the lattice parameter grows with increasing Ni concentration, following Vegard's law. In the final part, H-sorption analysis is performed first by using the DSC. Before introducing $TiFe_{1-x}Ni_x$ samples in the DSC cell, the instrument was first tested analyzing Pd and $LaNi_5$, since their hydrides have been extensively studied. Next, after the extraction of equilibrium pressures and temperatures by considering the half-reaction point of $TiFe_{1-x}Ni_x$ hydrides formation/decomposition, van't Hoff analysis is done to get the enthalpy and entropy of reaction. The values are in agreement with those available in literature. Since experimental ΔH and ΔS are linearly correlated, Enthalpy-Entropy Compensation is analyzed, confirming its genuine nature. Moreover, the absolute value of the enthalpy of reaction increases with increasing Ni concentration, demonstrating that Ni stabilizes the hydrides at lower equilibrium pressures. The correlation between increasing lattice parameter and enthalpy of the process with increasing Ni content, shows that the increased unit cell volume facilitates the hydrogen inlet and diffusion in the host crystal at lower pressures. This is important in the view of practical realization of the green hydrogen cycle. Higher hydride stability thanks to Ni-substitution is also confirmed by Sievert's measurements on $TiFe_{0.90}Ni_{0.10}$ and $TiFe_{0.80}Ni_{0.20}$. Completing these studies and evaluating the hydrogen capacity of all samples will help integrate the conclusions reached up to now.

The results of this research highlight the influence that microscopic modification, realized through stoichiometric tailoring, have on the structure, and in turn on the macroscopic features of the material, represented by the thermodynamics of hydride formation/decomposition. The characterization done for $TiFe_{1-x}Ni_x$ samples could be realized for new ones: compositional tailoring may be also exploited with different substitutional elements or bi- and multi-substituted alloys can be studied. Results of these analyses can be used

as a reference for the computational modeling of hydride systems.
In addition, because the final scope is to realize hydrides that can be produced and employed on a vast scale, it is important to assess the importance and influence of ball milling on the powder hydrogen-sorption properties, since it is not an available technique on industrial scale. Hydride activation is a process of crucial importance, and it would be useful to determine the physical processes driving it, together with the thermal or mechanical treatments that facilitate it to find the most efficient and fast way to have active materials. This is not only interesting for fundamental science, but also in the view of an industrial scale production. To this aim, compositional and mechanical surface studies should be performed on the samples. The structural analysis performed with XRD could be coupled to neutron scattering measurements, which represent a complementary method that would enrich the information available on the crystal. Additionally, the Sievert apparatus could be employed to do kinetic measurements and get more insight about kinetic aspects of hydrogen-sorption processes. Experimental analyses can also be coupled to computational studies: for example, results can be used as a reference for the modeling of hydride systems, allowing to extend the knowledge about their properties. In conclusion, both the variety of experimental techniques and the compositional tailoring will help disclose the physics characterizing hydrides, leading to a complete picture of new possible solutions for hydrogen storage.

Appendix A

DSC data analysis

A.1 Baseline removal

Removing the baseline in DSC measurements is fundamental to isolate the heat flow signal due to the transition occurring in the sample. Nonetheless, the procedure must not cause loss of interesting data. This problem is encountered if a simple linear baseline is used, for instance. A. Cisse et a.[39] developed a method to calculate an accurate baseline. First, a pre-peak baseline $f_{bl}^{pre}(T)$ and a post-peak baseline $f_{bl}^{post}(T)$ are determined, assuming a linear dependence of the heat flow on the temperature. Then a cubic spline fit is applied to find a unique baseline with initial and final slope equal to that found from the pre- and post- peak baselines. The resulting baseline has the following form:

$$f_{bl}(T) \;=\; (1-\alpha(T))\, f_{bl}^{pre}(T) + \alpha(T) f_{bl}^{post}(T) \tag{A.1}$$

where $\alpha(T)$ is a temperature-dependent function depending on the difference between apparent and real baseline, found with the cubic spline fit. In the present work, a similar technique has been applied, based on the following MatLab code:

```
function [Heat_Flow_corrected] = baseline_removal(T, H, T_lim_1, T_lim_2)

% T = temperature data
% H = heat flow data
% T_lim_1 = higher T bound limit for pre-peak baseline
% T_lim_1 = lower T bound limit for post-peak baseline

% define useful variables
T_baseline_pre = []; H_baseline_pre = [];
T_baseline_post = []; H_baseline_post = [];
bl_pre = []; bl_post = [];
T_q_pre = []; T_q_post = [];
P_pre = []; P_post = [];

% find pre-peak baseline slope
for i = 1:length(T)
if T(i)<T_lim_1
T_baseline_pre(end+1)=T(i);
H_baseline_pre(end+1)=H(i);
end
end
T_q_pre = linspace(T_baseline_pre(1), T_baseline_pre(end), 500);
P_pre = polyfit(T_baseline_pre', H_baseline_pre',1);
bl_pre = P_pre(1)*T_q_pre+P_pre(2);

% find pre-peak baseline slope
for i = 1:length(T)
if T(i)>T_lim_2
T_baseline_post(end+1)=T(i);
H_baseline_post(end+1)=H(i);
end
end
T_q_post = linspace(T_baseline_post(1), T_baseline_post(end), 500);
P_post = polyfit(T_baseline_post', H_baseline_post',1);
bl_post = P_post(1)*T_q_post+P_post(2);
```

```
% cubic spline baseline fit with initial and final slopes
% based on pre- and post- peak linear baselines previously found
bl = spline(cat(2,T_q_pre,T_q_post), [P_pre(1) cat(2, bl_pre, bl_post) P_post
    (1)],T);
plot(T,bl)

% baseline subtraction
Heat_Flow_corrected=H-bl;
end
```

The code analyzes absorption and desorption ramps separately, to find a correct baseline for each of them. The procedure applied to sample Ni20-b data at 35 bar is illustrated in Fig.A.1

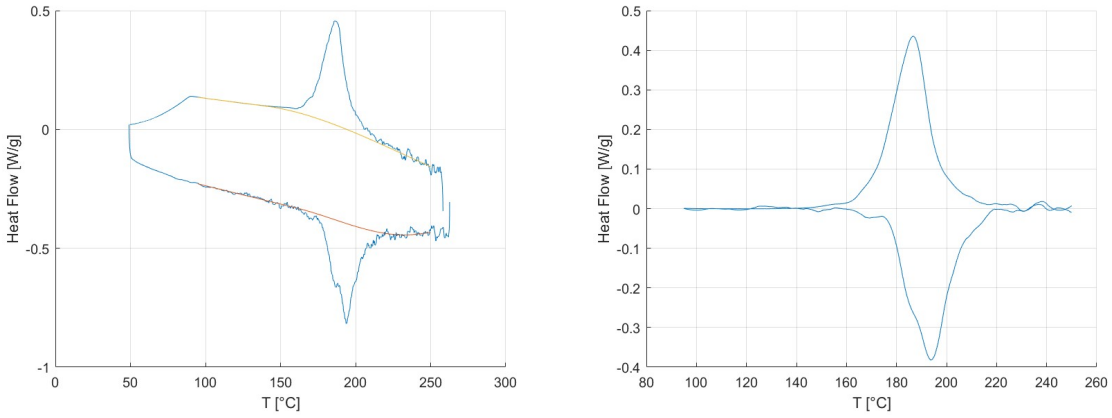

(a) (b)

Figure A.1: Starting from raw data, (a) absorption and desorption baselines are identified, and (b) removed.

A.2 DSC: van't Hoff analysis

After baseline removal, a first analysis of DSC data is done by following the method explained by Rongeat et al.[39] In their research, they determined T_{eq} by taking the intersection between the background line and the slope of the peak. This is done in the present work by taking the inflection point as the reference for calculating the slope. The procedure is in Fig.A.2 (a). The red curve is the peak fit, which is useful to define the function from which the derivative is computed. The fitting procedure is based on the *fit* function of MatLab:

```
y_fit = fit(x, y, fit_method, 'Startpoint', guesses);
```

fit depends on the x and y data (represented by temperature and heat flow), the fitting method and the starting guesses, which are the amplitude, the x position of maximum, and the width. The shape of the peaks, which defines the fitting method, is not straightforward to determine and is often given by the sum of multiple gaussian functions with different parameters, which gives additional sources of uncertainty on the fit. Peak deconvolution is also attempted in the case of multiple peaks present, but this is difficult since, due to their overlap, only the maximum and a reduced number of x (T) and y (heat flow) data can be used as a reference for the fit. Moreover, identifying the process corresponding to a certain peak is not easy, since multiple peaks can be due to the formation of different phases,

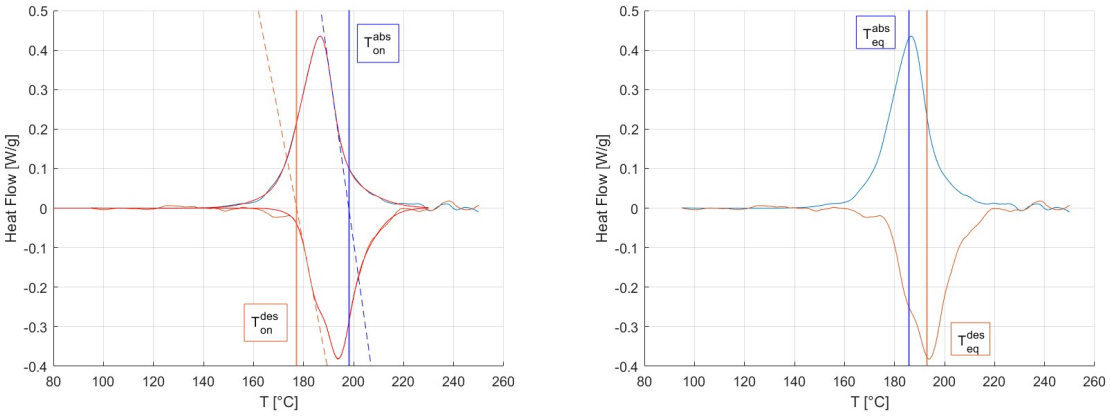

(a) (b)

Figure A.2: Equilibrium pressure and temperature determination by (a) inflection point method and (b) half-reaction method.

or the fact that different parts of the sample react at different pressure and temperature conditions (maybe because of inhomogeneities present). Thus assigning the extracted enthalpy and entropy of reaction to a specific transition is difficult. To work around this problem, the fit can be done by considering the first detectable signals for the cooling ramp and and on the heating one, and applying the method to this signal rise. Then:

$$T_{on} = \frac{T_{on}^{abs} + T_{on}^{des}}{2} \tag{A.2}$$

Values resulting from this are summed up in Tab.A.1.

Table A.1: *Results of van't Hoff analysis applied on* $TiFe_{1-x}Ni_x$ *data based on inflection point method.*
$\Delta H(S)^{exp}$ are the experimental values from the fit, derived from the average of absorption and desorption parameters T, p. Errors are given by the standard deviation.

Sample	$\lvert\Delta H^{exp}\rvert$ $[kJ\ mol^{-1}]$	$\lvert\Delta S^{exp}\rvert$ $[J\ mol^{-1}\ K^{-1}]$
Ni05-b	27.4±0.6	98.6±1.4
Ni10-b	30.5±0.1	102.9±0.3
Ni15-b	33.9±0.2	105.9±0.4
Ni20-b	35.1±1.5	105.8±3.2
Ni30-b	38.0±1.7	102.2±3.4

They show increasing enthalpy with increasing Ni concentration, with a slightly weaker dependence than those in Tab.4.6. Also entropy is expected to grow with Ni concentration, but this is not observed for x >0.15. A limit of this analysis procedure is that a reaction that can take place in large temperature range (spanning over 200°C for Ni30-b, Fig.4.10)

is represented by the pressure and temperature of the starting point of the process. This may not be an appropriate conclusion to draw, also recalling that the peak onset can often depend on the kinetics of the process, and not on the thermodynamics described by van't Hoff equation. A method depending on less starting guesses and constraints, while being able to extract meaningful results, is required. The half-reaction method described in section 3.3.1 has been applied with the following MatLab code and seems to do the work (Fig.A.2 (b)):

```
% full peak area
signal_area = abs(trapz(t*60, H/mass, 2));

% iteratively calculate the area
for i=1:length(T)
area(end+1) = abs(trapz(t(1:i)*60, H(1:i)/mass, 2));
delta_area(end+1) = abs(area(i)-signal_area/2);
end

%fing T at which the integral is the half of the total area
[minval, index] = min(delta_area);

t_ref=t(index); T_ref = T(index); p_ref = p(index)/100+1;
xline(T_ref, 'r');
```

Also in this case, some carefulness must be applied. Indeed, one should avoid to perform the integral calculation with respect to the temperature, converting the heat flow [W] to energy [J] by recalling that $\Delta t = \Delta T r^{-1}$, where $r = \left(\frac{dT}{dt}\right)$ is the temperature rate. Even if such method would seem to be intuitive, it might cause mistakes due to the non-constant r at low temperatures. In particular, if peaks are near the low temperature range limit, as in Ni05-b and Ni10-b, this leads to higher equilibrium temperatures than the correct ones, since the rate decreases due to the difficulty to cool the DSC cell down. Thus, the calculation must be done directly referring to the measured experimental time as x-data.

Bibliography

[1] A. Zuttel et al., *Hydrogen: the future energy carrier*, Phil. Trans. R. Soc. A 2010 368, doi: 10.1098/rsta.2010.0113

[2] NOAA - Climate Change: Atmospheric Carbon Dioxide https://www.climate.gov/news-features/understanding-climate/climate-change-atmospheric-carbon-dioxide

[3] Met Office Hadley Centre for Climate Science and Services (2023) – processed by Our World in Data, https://ourworldindata.org/co2-and-greenhouse-gas-emissions

[4] United Nations, Climate action, *Causes and Effects of Climate change*, https://www.un.org/en/climatechange/science/causes-effects-climate-change

[5] NASA, Vital Signs of the Planet, *How do we know climate change is real?*, https://climate.nasa.gov/evidence/

[6] IEA, Global Energy Crisis, *How the energy crisis started, how global energy markets are impacting our daily life, and what governments are doing about it*, https://www.iea.org/topics/global-energy-crisis

[7] Energy Institute - Statistical Review of World Energy (2023); Smil (2017) – with major processing by Our World in Data, https://ourworldindata.org/energy-production-consumption

[8] R. Griessen and A. Zuttel, *Science and Technology of Hydrogen in Metals* (2003)

[9] A. Züttel, *Materials for hydrogen storage*, Materials today, 2003, 6.9: 24-33, https://doi.org/10.1016/S1369-7021(03)00922-2

[10] N. Patelli, A. Migliori, V. Morandi, and L. Pasquini, *Interfaces within biphasic nanoparticles give a boost to magnesium-based hydrogen storage*, Nano Energy, 2020, 72, 104654, https://doi.org/10.1016/j.nanoen.2020.104654

[11] L. Pasquini, *Design of Nanomaterials for Hydrogen Storage*, Energies 2020, 13, 3503, https://doi.org/10.3390/en13133503

[12] A. Züttel, FUELS - HYDROGEN STORAGE - Hydrides, Encyclopedia of Electrochemical Power Sources, Elsevier, edited by J. Garche, 2009, 440-458, ISBN 9780444527455, https://doi.org/10.1016/B978-044452745-5.00325-7

[13] U.S. Department of Energy, Office of energy efficiency and renewable energy, https://www.energy.gov/eere/fuelcells/safe-use-hydrogen

[14] Clean Hydrogen Joint Undertaking, Programme review report 2023, Publications Office of the European Union, 2023, https://data.europa.eu/doi/10.2843/260486

[15] M. Chatenet et al., *Water electrolysis: from textbook knowledge to the latest scientific strategies and industrial developments*, Chem. Soc. Rev., 2022, 51, 4583, https://doi.org/10.1039/D0CS01079K

[16] M. E. M. Buan, *Photoelectrochemical Hydrogen Production*, 2012, Master's Thesis, Institutt for materialteknologi

[17] M. Winter and R. J. Brodd, *What are Batteries, Fuel Cells, and Supercapacitors?*, Chem. Rev., 2004, 104, 10, 4245–4270, https://doi.org/10.1021/cr020730k

[18] Y. Fukai, *The metal-hydrogen system*, 2nd ed. (Springer Berlin, Heidelberg)

[19] J. D. Fast, *Interaction of metals and gases*, Vol. 2 Kinetics and Mechanisms (Macmillan Press LDT)

[20] Neil W. Ashcroft, N. David Mermin, *Solid State Physics* (Harcourt College Publishers, 1976)

[21] K. H. J. Buschow, P. C. P. Bouten and A. R. Miedema, *Hydrides Formed from Intermetallic Compounds of Two Transition Metals: A Special Class of Ternary Alloys*, Reports on Progress in Physics, November 2000, 45(9):937, http://dx.doi.org/10.1088/0034-4885/45/9/001

[22] G. E. R. Schulze: Metallphysik, Akademie-Verlag, Berlin 1967

[23] E. M. Dematteis, N. Berti, F. Cuevas, M. Latroche and M. Baricco, *Substitutional effects in TiFe for hydrogen storage: a comprehensive review*, Mater. Adv., 2021, 2, 2524–2560, https://doi.org/10.1039/d1ma00101a

[24] R.B. Schwarz, A.G. Khachaturyan, *Thermodynamics of open two-phase systems with coherent interfaces: Application to metal–hydrogen systems*, Acta Materialia 54 (2006) 313–323, https://doi.org/10.1016/j.actamat.2005.08.044

[25] Hayoung Kim, ShinYoung Kang, Ji Yeong Lee, Tae Wook Heo, Brandon C. Wood, Jae-Hyeok Shim, Young Whan Cho, Do Hyang Kim, Jin-Yoo Suh, Young-Su Lee, *A new perspective on the initial hydrogenation of $TiFe_{0.9}M_{0.1}$ (M = V, Cr, Fe, Co, Ni) alloys gained from surface oxide analyses and nucleation energetics,*, Applied Surface Science, Volume 610, 2023, 155443, https://doi.org/10.1016/j.apsusc.2022.155443.

[26] A. Santhosh, S. Kang, N. Keilbart, B. C. Wood, T. Klassen, P. Jerabek and M. Dornheim, *Influence of near-surface oxide layers on TiFe hydrogenation: mechanistic insights and implications for hydrogen storage applications*, J. Mater. Chem. A, 2023, 11, 18776, 10.1039/d3ta02205f

[27] J. W. Christian, *The Theory of Transformations in Metals and Alloys*, 2nd edition, Pergamon Press (2002), https://doi.org/10.1016/B978-0-08-044019-4.X5000-4

[28] Wicke, E., Brodowsky, H., Züchner, H. (1978). *Hydrogen in palladium and palladium alloys*, in: Alefeld, G., Völkl, J. (eds) *Hydrogen in Metals II*, Topics in Applied Physics, vol 29. Springer, Berlin, Heidelberg (1978) https://doi.org/10.1007/3-540-08883-0_19

[29] R. Lässer and K. H. Klatt, *Solubility of hydrogen isotopes in palladium*, Phys. Rev. B 28, 748–758 (1983), https://doi.org/10.1103/PhysRevB.28.748

[30] E. H. Kisi, C. E. Buckley, E. M. Gray, *The hydrogen activation of $LaNi_5$*, Journal of Alloys and Compounds, 1992, 185, 369-384, from https://www.crystallography.net/cod/search.html

[31] J.-M. Joubert, V. Paul-Boncour, F. Cuevas, J. Zhang, M. Latroche, *$LaNi_5$ related AB_5 compounds: Structure, properties and applications*, Journal of Alloys and Compounds 862 (2021) 158163, https://doi.org/10.1016/j.jallcom.2020.158163

[32] S. Luo , J.D. Clewley , Ted B. Flanagan , R.C. Bowman Jr. , L.A. Wade, *Further studies of the isotherms of $LaNi_{5-x}Sn_x$–H for x=50–0.5*, Journal of Alloys and Compounds 267 (1998) 171–181, https://doi.org/10.1016/S0925-8388(97)00536-7

[33] E. M. Dematteis, D. M. Dreistadt, G. Capurso, J. Jepsen, F. Cuevas, M. Latroche, *Fundamental hydrogen storage properties of TiFe-alloy with partial substitution of Fe by Ti and Mn*, Journal of Alloys and Compounds 874 (2021) 159925, https://doi.org/10.1016/j.jallcom.2021.159925

[34] https://www.crystallography.net/cod/search.html

[35] https://www.malvernpanalytical.com/en/products/category/software/x-ray-diffraction-software/highscore-with-plus-option

[36] https://luttero.github.io/maud/

[37] A. Hewat, William I. F. David and L. van Eijckc, *Hugo Rietveld*, J. Appl. Cryst. (2016). 49, 1394–1395, http://dx.doi.org/10.1107/S1600576716012061

[38] https://jp-minerals.org/vesta/en/

[39] C. Rongeat, I. Llamas-Jansa, S. Doppiu, S. Deledda, A. Borgschulte, L. Schultz, and O. Gutfleisch, *Determination of the Heat of Hydride Formation/Decomposition by High-Pressure Differential Scanning Calorimetry (HP-DSC)*, J. Phys. Chem. B 2007, 111, 13301-13306, https://doi.org/10.1021/jp075954r

[40] D. B. Robinson, W. Luo, T. Y. Cai, and K. D. Stewart, *Metal Hydride Differential Scanning Calorimetry as an Approach to Compositional Determination of Mixtures of Hydrogen Isotopologues and Helium*, International Journal of Hydrogen Energy, 40(41), 2015, 14257-14270 http://dx.doi.org/10.1016/j.ijhydene.2015.08.033

[41] *DSC Differential Scanning Calorimeter, Q Series^{TM} - Getting Started Guide* by by TA Instruments—Waters LLC (2007)

[42] A. Cisse, J. Peters, G. Lazzara, Leonardo Chiappisi, *PyDSC: a simple tool to treat diferential scanning calorimetry data*,Journal of Thermal Analysis and Calorimetry (2021) 145:403–409, https://doi.org/10.1007/s10973-020-09775-9

[43] Y.-W. Lee, B. M. Clemens, K. J. Gross, *Novel Sieverts' type volumetric measurements of hydrogen storage properties for very small sample quantities*, Journal of Alloys and Compounds 452 (2008) 410–413, https://doi.org/10.1016/j.jallcom.2006.11.014

[44] R. Bitter, T. Mohiuddin, and M. Nawrocki (2006) *LabVIEW: Advanced programming techniques*, Crc Press (2006)

[45] E. Pericoli, *Synthesis and characterisation of metal hydrides for hydrogen storage applications*, http://amslaurea.unibo.it/29476/

[46] T. V. Philip, P. A. Beck, Trans. Am. Inst. Min. Metall. Pet. Eng. 209, 1269 (1957)

[47] Rostoker, Armour Research Foundation, Chicago, Illinois, USA, Private Communication

[48] H. C. Siegmann, L. Schlapbach, and C. R. Brundle, *Self-Restoring of the Active Surface in the Hydrogen Sponge $LaNi_5$*. Physical Review Letters, 40(14), 972–975 (1978) doi:https://doi.org/10.1103/physrevlett.40.972

[49] M.T. Hagström, P.D. Lund, *Pressure DSC studies on the formation and reproducibility of double peaks in the sorption of $LaNi_5$-H_2 during thermal cycling*, Thermochimica Acta 298 (1997) 141-147, https://doi.org/10.1016/S0040-6031(97)00088-9

[50] A. Andreasen, Predicting formation enthalpies of metal hydrides, Risø National Laboratory (2004)

[51] Y. Li, H. Shang, Y. Zhang, P. Li, Y. Qi, D. Zhao, *Investigations on gaseous hydrogen storage performances and reactivation ability of as-cast $TiFe_{1-x}Ni_x$ (x=0, 0.1, 0.2 and 0.4) alloys*, International Journal of Hydrogen Energy, 44, 8, 2019, 4240-4252, https://doi.org/10.1016/j.ijhydene.2018.12.144

[52] M.H. Mintz, S. Vaknin, S. Biderman, and Z. Hadari, *Hydrides of ternary $TiFe_xM_{1-x}$ (M=Cr, Mn, Co, Ni) intermetallics*, Journal of Applied Physics 52, 463 (1981), https://doi.org/10.1063/1.329808

[53] R. Griessen, C. Boelsma, H. Schreuders, C. P. Broedersz, R. Gremaud, and B. Dam, *Single Quality Factor for Enthalpy-Entropy Compensation, Isoequilibrium and Isokinetic Relationships*, ChemPhysChem 2020, 21, 1632– 1643, https://doi.org/doi.org/10.1002/cphc.202000390

[54] R. Griessen, and B. Dam, *Simple Accurate Verification of Enthalpy-Entropy Compensation and Isoequilibrium Relationship*, ChemPhysChem 2021, 22, 1774– 1784, https://doi.org/doi.org/10.1002/cphc.202100431

[55] J. D. Dunitz, *Win some, lose some: enthalpy-entropy compensation in weak intermolecular interactions*, Chemistry & Biology, 2 (11), 1995, 709-712, https://doi.org/10.1016/1074-5521(95)90097-7

[56] B. Fultz, *Vibrational thermodynamics of materials*, Progress in Materials Science, 55 (4), 2010, 247-352, https://doi.org/10.1016/j.pmatsci.2009.05.002

[57] F. Cuevas, JM. Joubert, M. Latroche, et al. *Intermetallic compounds as negative electrodes of Ni/MH batteries*, Appl Phys A 72, 225–238 (2001), https://doi.org/10.1007/s003390100775

[58] C.E. Lundin, F.E. Lynch and C.B.Magee, *A correlation between the interstitial hole sizes in intermetallic compounds and the thermodynamic properties of the hydrides formed from those compounds*, Journal of the Less Common Metals 56, 19–37 (1977)

[59] H. Miyamura , M. Takada, K. Hirose, S. Kikuchi, *Metal hydride electrodes using titanium–iron-based alloys*, Journal of Alloys and Compounds 356–357 (2003) 755–758, https://doi.org/10.1016/S0925-8388(03)00084-7

[60] H.K. Smith, W.E. Wallace and R.S. Craig, *An investigation of $R_6Fe_{23}H_x$ thermodynamics*, Journal of the Less-Common Metals, 94 (1983) 89-93